Thesis for the degree of Doctor of Engineering

Investigation of Sigma-Delta-over-Fiber for High-Capacity Wireless Communication Systems

Husileng Bao

Department of Microtechnology and Nanoscience - MC2
CHALMERS UNIVERSITY OF TECHNOLOGY
Göteborg, Sweden 2024

Investigation of Sigma-Delta-over-Fiber for High-Capacity Wireless Communication Systems
Husileng Bao
978-91-7905-976-7

Doktorsavhandlingar vid Chalmers tekniska högskola
Ny serie nr 5442
ISSN 0346-718X

Department of Microtechnology and Nanoscience - MC2
Chalmers University of Technology
SE–412 96 Göteborg, Sweden
Telephone + 46 (0) 31 – 772 1000

Typeset by the author using LaTeX.

Printed by Chalmers Digitaltryck
Göteborg, Sweden 2024

Abstract

The advent of beyond-5G (B5G) and 6G technologies brings increases in wireless devices and their applications. Although massive multiple-input-multiple-output (MIMO) delivers high-capacity services using co-located MIMO (C-MIMO) technology, distributed MIMO (D-MIMO) technology offers a more uniform user service.

This thesis introduces an automatic D-MIMO testbed featuring a statistical MIMO capacity analysis for an indoor use case. Additionally, raytracing-based simulations are employed for predictions and comparisons in an indoor scenario. The statistical MIMO capacity analysis demonstrates that D-MIMO outperforms C-MIMO in terms of both higher and more uniform capacity, as observed in measurements and simulations.

A promising solution for such future communication systems is radio-over-fiber (RoF). Achieving data rates in the range of several tens of Gbit/s necessitates the utilization of the millimeter-wave (mm-wave) frequency band in RoF. However, mm-wave signals exhibit high propagation loss. Overcoming these challenges requires the incorporation of beamforming and/or MIMO technology in mm-wave RoF systems.

Subsequently, a mm-wave sigma-delta-over-fiber (SDoF) link architecture is proposed for MIMO applications. The first implementation utilizes bandpass sigma-delta modulation (SDM) between a central unit (CU) and a remote radio unit (RRU) through a commercially available QSFP28-based optical interconnect. The implementation achieves symbol rates of 700/500 Msym/s for single-input-single-output (SISO)/multi-user MIMO (MU-MIMO) cases at a 1 m over-the-air (OTA) distance. The second implementation employs lowpass SDM between a CU and a RRH, and reaches 1 Gsym/s with 1024-quadrature amplitude modulation (1024-QAM) signal across a 5 m OTA distance.

Furthermore, the proposed mm-wave link is extended to two SDoF D-MIMO architectures, both incorporating a CU-inherited local oscillator for phase coherence verification. The bandpass SDoF-based D-MIMO system supports a 748 MHz bandwidth with orthogonal frequency-division multiplexing (OFDM) signals for multiple-input-single-output (MISO)/MU-MIMO cases, while the lowpass SDoF-based D-MIMO system operates in the W-band for MISO measurement cases.

In conclusion, this thesis has shown that D-MIMO surpasses C-MIMO in both capacity and uniformity, as validated through statistical analyses from measurements and simulations. The proposed innovative mm-wave SDoF D-MIMO architectures lay the foundation for future high-capacity wireless communication networks.

Keywords: Radio-over-fiber, central unit, remote radio head, multiple-input-multiple-output, millimeter-wave.

Acknowledgments

I received countless help during my journey to this licentiate thesis. As doctoral research is pushing the human knowledge boundary, I could not imagine how I could survive without following people:

My first and most gratitude is to my main supervisor, Professor Christian Fager, for giving guidance, valuable feedback, and resources. Without your state-of-the-art support, we can not have those state-of-the-art publications and I can not reach this thesis. "Thanks! Christian."

Another important person for me is my examiner, Professor Magnus Karlsson, who shapes me as a qualified researcher. Even if we do not often have personal interactions due to where we are located, I know you are always there when I need to talk with someone.

I can not forget you, my industry supervisor, Dr. Filippo Ponzini. Thanks for your creative feedback and supervision. It is always a pleasure to have a pleasant and innovative discussion with you!

I finished most of my courses and research work in the microwave electronic laboratory (MEL) with the help of my colleagues. When I am stuck with my homework, I know there is always someone who can help. When I panic about my measurement, I still can find the necessary support. Please accept my huge thanks, MEL friends!

I had an unforgettable period in Ericsson Research (Pisa, Italy) with my lovely colleagues. You are always giving me top priority for my laboratory activity. I have felt the warmest time from your host. You spoiled me with Italian lunch and coffee, which I can not find anywhere else!

It is my privilege to have the opportunity to join the MyWave project, which has received funding from the European Union's Horizon 2020 research and innovation programme under the Marie Skłodowska-Curie grant agreement No 860023. In this project, I have met excellent senior researchers who have been role models for my whole life and kind colleagues who always support me no matter how I misbehave.

My work was also in part funded by the Swedish Research Council (grant VR-2019-05174).

I want to thank Xilinx and Analog Devices for the donations of hardware. I also thank Keysight for the loan of equipment during measurements.

I only feel this section is too short of expressing my gratitude to all of you one by one. "Thank you!"

Husileng Bao
Göteborg, December 2023

List of Publications

This thesis is based on the following papers:

[A] **H. Bao**, I. C. Sezgin, Z. S. He, T. Eriksson and C. Fager, "Automatic Distributed MIMO Testbed for Beyond 5G Communication Experiments," *2021 IEEE MTT-S International Microwave Symposium (IMS)*, Atlanta, GA, USA, 2021.

[B] C. Fager, S. Rimborg, E. Rådahl, **H.Bao** and T. Eriksson, "Comparison of Co-located and Distributed MIMO for Indoor Wireless Communication," *2022 IEEE Radio and Wireless Symposium (RWS)*, Las Vegas, NV, USA, 2022.

[C] **H. Bao**, Z. S. He, F. Ponzini and C. Fager, "Demonstration of Flexible mmWave Digital Beamforming Transmitter using Sigma-Delta Radio-Over-Fiber Link," *2022 52nd European Microwave Conference (EuMC)*, Milan, Italy, 2022.

[D] **H. Bao**, F. Ponzini and C. Fager, "Flexible mm-Wave Sigma-Delta-Over-Fiber MIMO Link," in *Journal of Lightwave Technology*, vol. 41, no. 14, pp. 4734-4742, July 2023.

[E] **H. Bao**, F. Ponzini and C. Fager, "Wideband mm-wave Spectrum-Efficient Transmitter Using Low-Pass Sigma–Delta-Over-Fiber Architecture," in *IEEE Microwave and Wireless Technology Letters*, vol. 33, no. 10, pp. 1505-1508, October 2023.

[F] **H. Bao**, F. Ponzini and C. Fager, "Wideband mm-wave 6 × 2 Distributed MIMO Transmitter using Sigma-Delta-over-Fiber," accepted for publication in *Journal of Lightwave Technology*, January 2024.

[G] **H. Bao**, G. Gavell, and C. Fager, "W-Band Distributed MIMO Demonstration using low-Pass Sigma-Delta-over-Fiber," *manuscript*.

The content of the following publications partially overlaps with the appended papers or is out of the scope of this thesis.

[H] **H. Bao**, A. Ziemann and Z. S. He, "Design and Measurements of MSK-LFM RadCom System," *2020 17th European Radar Conference (EuRAD)*, Utrecht, Netherlands, 2021.

[I] M. F. Keskin, I. C. Sezgin, **H. Bao**, H. Wymeersch and C. Fager, "Localization With Distributed MIMO Using a High-Speed Sigma-Delta-Over-Fiber Testbed," in *IEEE Microwave and Wireless Components Letters*, vol. 32, no. 7, pp. 923-926, July 2022.

[J] Meyer E, Kruglov D, Krivic M et al, "The state of the art in beyond 5G distributed massive multiple-input multiple-output communication system solutions," *Open Res Europe 2022*.

As part of the author's doctoral studies, some of the work presented in this thesis has previously been published in [K]. Therefore, figures, tables, and text from [K] may be fully or partly reproduced in this thesis.

[K] **H. Bao**, "High Capacity Fiber-Connected Wireless MIMO Communication," *Chalmers University of Technology*, Gothenburg, 2023, ISSN 1652-0769.

Acronyms

3D	Three-Dimensional
3GPP	The 3rd Generation Partnership
4-ASK	Quaternary-Amplitude-Shift-keying
4G	Fourth Generation
5G	Fifth Generation
6G	Sixth Generation
ACPR	Adjacent Channel Power Ratio
ARoF	Analog Radio-over-Fiber
BER	Bit-Error Rate
BPF	Bandpass Filter
BPSDM	Bandpass Sigma-Delta Modulation
C-MIMO	Co-located Multiple-Input-Multiple-Output
C-RAN	Centralized Radio Access Network
CDR	Clock Data Recovery
CPRI	Common Public Radio Interface
CU	Central Unit
D-MIMO	Distributed Multiple-Input-Multiple-Output
DAC	Digital-to-Analog Converter
DEMUX	Demultiplexer
DL	Downlink
DRoF	Digital Radio-over-Fiber
DSP	Digital Signal Processing
E/O	Electrical/Optical
eCPRI	Enhanced Common Public Radio Interface
EVM	Error Vector Magnitude
FDD	Frequency Division Duplex
FEC	Forward Error Correction
FPGA	Field Programmable Gate Array
GPS	Global Positioning System
I/Q	In-phase/Quadrature
IF	Intermediate Frequency
IID	Independent Identically Distribution
IoT	Internet of Things
LNA	Low Noise Amplifier
LO	Local Oscillator

LPSDM	lowpass sigma-delta modulator
LS	Least-Squares
LTE	Long-Term Evolution
LuMaMi	Lund University massive MIMO
MCF	Multi-Core Fiber
MIMO	Multiple-Input-Multiple-Output
MISO	Multiple-Input-Single-Output
mm-wave	Millimeter Wave
MMSE	Minimum-Mean Squared Error
MRT	Maximum Ratio Transmission
MU-MIMO	Multi-User Multiple-Input-Multiple-Output
MZM	Mach-Zehnder Modulator
NMSE	Normalized Mean Square Error
O/E	Optical/Electrical
OFDM	Orthogonal Frequency-Division Multiplexing
OTA	Over-The-Air
PA	Power Amplifier
PC	Personal Computer
PLL	Phase-Locked Loop
QAM	Quadrature Amplitude Modulation
QPSK	Quadrature Phase Shift Keying
QSFP28	Quad Small Form-Factor Pluggable 28
RAN	Radio Access Network
RF	Radio Frequency
RoF	Radio-over-Fiber
RRH	Remote Radio Head
RX	Receiver
SDM	Sigma-Delta Modulation
SDoF	Sigma-Delta-over-Fiber
SISO	Single-Input-Single-Output
SMF	Single-Mode Fiber
SNR	Signal-to-Noise Ratio
TDD	Time Division Duplex
TX	Transmitter
UL	Uplink
ZF	Zero-Forcing

Contents

Chapter 1

Introduction

1.1 Motivation

The fifth generation (5G) communication networks bring several advancements such as Enhanced Mobile Broadband, Ultra-Reliable and Low Latency Communications, massive Machine-Type Communications [2][3]. Concurrently, the Internet of Things (IoT) will connect millions of devices per square kilometer, demanding high data rates [4]. As user densities surge in the realms of 5G and IoT [5][6], wireless communication systems must offer higher capacity solutions and also better and more uniform quality of service.

A recent report from Ericsson summarizes mobile user subscriptions, 5G subscriptions, and monthly data traffic per user [1], depicted in Figure 1.1. Projections for 2021 - 2023 suggest that subscriptions will surpass 9000 million by the end of 2029, with 5G subscriptions reaching approximately 5300 million by that time. This growth positions 5G as the dominant communication network, constituting more than half of all subscriptions. The monthly mobile data traffic per device, which was 11.9 GB/month in 2021, is expected to grow to 55 GB/month. This dramatic increase in data traffic, coupled with the expected 5G devices, underscores the urgent need for high-capacity wireless communication systems.

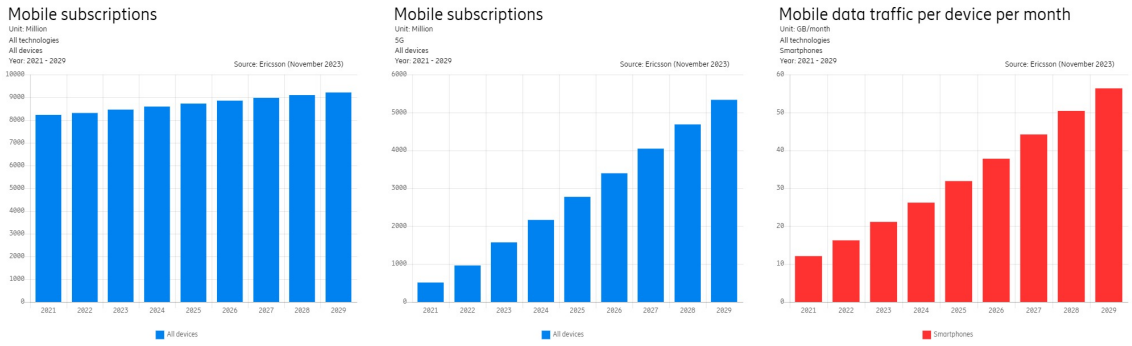

(a) (b) (c)

Figure 1.1: Ericsson worldwide study results [1]. (a) User subscriptions; (b) 5G subscriptions; (c) Monthly data traffic per user.

Currently available in over 1300 cities across 61 countries [7], commercial 5G is expanding rapidly. In contrast, the sixth generation (6G) communication network is in its early research phase, aiming for higher capacity, lower latency, increased reliability, and a high-density communication strategy by 2030 [8]. A key focus of 6G is achieving low power consumption while enabling ubiquitous communication [9]. For the 6G ambitions, some research institutions and universities have taken action, as follows: Ericsson Research expanded the 6G research unit worldwide and predicts new ways of seamless communications [10]. Nokia Bell Labs has 5G and 6G research being developed in parallel, while 6G technology research is in the exploratory start-up phase [11]. The European Union funding for the 6G research under the Horizon Europe programme aims to contribute to the sustainable development goals of the United Nations towards sustainable, resilient, and climate-neutral network infrastructures and services [12]. One of the earliest European initiative 6G research programs was the 6G Flagship Center in Finland, investigating sustainable solutions for society needs [13]. In short, 6G is coming as a sustainable ultra-high data rate wireless communication infrastructure.

The substantial surge in 5G subscriptions and commercial network deployments underscores the imperative for a high-capacity communication network in society. As 6G research advances in leading wireless communication research groups worldwide, the ultra-high data rate communication system remains a vibrant research area.

Massive multiple-input-multiple-output (MIMO) is an important technology, using co-located MIMO (C-MIMO), enhancing communication capacity in 5G applications [14]. Additionally, distributed MIMO (D-MIMO) and cell-free MIMO have recently been proposed to further enhance communication capacity and ensure uniform user service in the context of 6G [15].

1.2 Contributions

Radio-over-fiber (RoF) is is already playing an important role in the implementation of 5G MIMO communication networks and will play a critical role in future research activities. It establishes a connection between a remote radio head (RRH) and a central unit (CU) through fiber optics, facilitating the deployment of C-MIMO systems via an antenna array in the RRH. However, RoF requires enhancements to accommodate the advancements in D-MIMO concerning complexity, capacity, and synchronization. Additionally, the introduction of high-frequency bands for various applications introduces yet another layer of complexity to the existing technological solutions.

This thesis contributes to the exploration of millimeter wave (mm-wave) RoF for high-capacity wireless communication systems through a variety of innovative solutions. Specifically, a mm-wave D-MIMO RoF communication system using sigma-delta modulation (SDM) is proposed. For RoF technology, applying SDM in a CU simplifies the RRH architecture at transmission direction. Hence, this thesis concentrates on the downlink (DL) direction, from the RRH to the users. The investigation introduces a low-complexity, generalized mm-wave D-MIMO communication

transmitter architecture in Paper [C]. The proposed architecture offers two viable implementations as in Paper [D] and Paper [E]. These implementations present flexible, digitally controlled D-MIMO demonstrations in Paper [F] and Paper [G], delivering exceptional data throughput. The demonstration in Paper [G] is operating even up to the 100 GHz frequency band. The proposed architecture with the demonstrations, supported by experimental results, constitutes a direct and impactful contribution to the evolving requirements of future communication networks.

1.3 Thesis Scope and Outline

The thesis is organized as follows. In Chapter 2, the evolution of MIMO technology is detailed. Additionally, an examination of various RoF wireless system architectures is provided, specifically focusing on implementations of D-MIMO, along with an exploration of the underlying theories.

Chapter 3 provides an in-depth exploration of the capacity of the proposed fiber-connected D-MIMO systems conducted through extensive measurements and simulations. The chapter starts with a summary of the existing low-frequency C-MIMO/D-MIMO testbed. A significant contribution is made through a statistical study of C-MIMO and D-MIMO in an indoor environment, utilizing an automated testbed (referenced as Paper [A]). The study concludes that D-MIMO exhibits a more uniform and higher communication capacity than C-MIMO. This contribution is reinforced in Paper [B] through a comparison between simulation and measurement results.

Chapter 4 focuses on mm-wave sigma-delta-over-fiber (SDoF) systems, including a review of available solutions. Paper [C] introduces a wideband, flexible, and straightforward all-digital mm-wave architecture, implementing it with commercially available hardware. Furthermore, the chapter includes an over-the-air (OTA) demonstration of the proposed link, comparing the results with state-of-the-art findings (as outlined in Paper [D]). This demonstration documents the highest reported data rate in any mm-wave SDoF MIMO system.

In Chapter 5, a study on mm-wave SDoF D-MIMO systems is presented. The chapter begins by examining published state-of-the-art studies on high-frequency D-MIMO. Subsequently, the mm-wave link introduced in Chapter 4 is expanded to encompass two SDoF D-MIMO architectures: a bandpass SDoF-based D-MIMO system and a lowpass SDoF-based D-MIMO system. Both architectures are verified through detailed investigations, demonstrating coherent phase communication performance.

Chapter 6 provides a comprehensive summary of this thesis and suggests relevant future research. Finally, Chapter 7 contains a summary of appended papers.

Chapter 2

Wireless MIMO Technology Evolution

The low-frequency band, extending up to 6 GHz, is densely populated within the electromagnetic spectrum, hosting numerous applications such as business services, consumer terminals, military applications, navigation systems, astronomy, television broadcasts, etc. The crowded spectrum underscores the critical importance of spectral efficiency. Spatial multiplexing, facilitated by multi-antenna MIMO techniques initially proposed in [16] and subsequently refined, stands out as an approach to enhance spectral efficiency. MIMO has evolved into a fundamental technology embedded in all modern wireless systems, starting from the fourth generation (4G) mobile system and gaining further prominence in 5G, with expectations of increased relevance in future advancements. The subsequent subsections discuss the fundamentals of single-input-single-output (SISO)/multiple-input-single-output (MISO)/MIMO for DL connection of wireless communication.

Wireless MIMO systems fall into two primary categories: $co-located$ and *distributed* variants. The practical implementation of these systems heavily involves RoF technology and communication fundamentals.

2.1 SISO Communication Fundamentals

This section provides an overview of the SISO model and its capacity.

2.1.1 SISO Model

A wireless communication system comprises at least one transmitter (TX) and one receiver (RX). On the TX side, the signal is emitted into the channel through an antenna, while the RX side receives the transmitted signal via an antenna. The TX antenna serves as the input port for the wireless channel, and the RX antenna serves as the output port. When a wireless communication system features one TX antenna and one RX antenna, it is referred to as a SISO system.

In Figure 2.1, an idealized SISO communication system is depicted, characterized by a single coefficient, h, representing the channel between the TX and RX. This

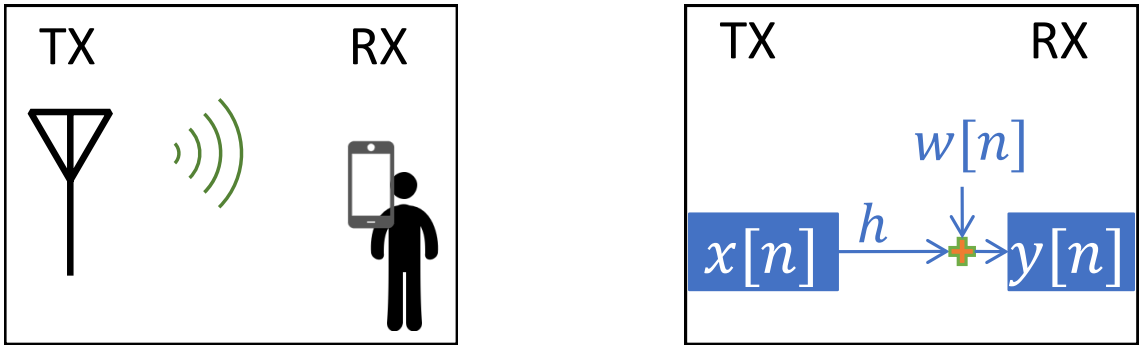

(a) (b)

Figure 2.1: Principal illustration of (a) SISO case; (b) SISO model.

channel element, a complex value, defines the radio frequency (RF) signal amplitude and phase of the channel, as

$$y[n] = hx[n] + w[n], \tag{2.1}$$

where $x[n]$ denotes the discrete signal at time index n from the TX, and $y[n]$ represents the corresponding received signal at the RX, as illustrated in Figure 2.1b. In real-world scenarios, the received signal incorporates additive noise $w[n]$ originating from system components and the wireless channel.

2.1.2 SISO Capacity

Assuming a Gaussian channel, the ideal communication capacity of a SISO system is given as [17]

$$C = B \log_2 \left(1 + \frac{S}{N}\right) [\text{bit/s}], \tag{2.2}$$

where B denotes the communication bandwidth, and $\frac{S}{N}$ represents the signal-to-noise ratio (SNR). Increasing either bandwidth or SNR ideally results in higher capacity. However, practical limitations, especially in low-frequency bands with restricted bandwidth, make it challenging to achieve significant increases. Additionally, boosting SNR only yields a logarithmic capacity increase. Consequently, MIMO technology becomes imperative to enhance system capacity [18].

2.2 MISO Communication Fundamentals

In the section on MISO communication fundamentals, we explore the model and precoding.

2.2.1 MISO Model

A single TX antenna typically has a fixed radiation pattern with wide coverage and low gain, catering to mobile users. By replacing the single antenna with a phased

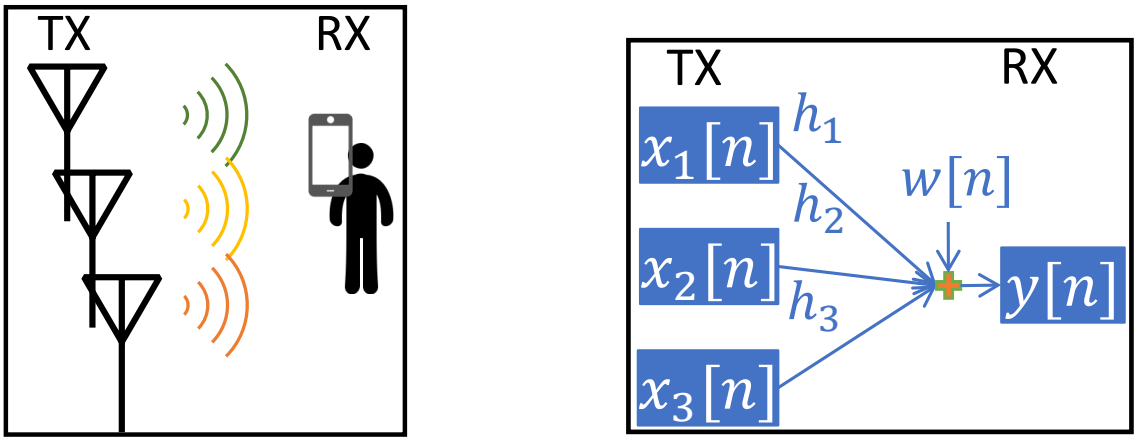

(a) (b)

Figure 2.2: Principal illustration of (a) MISO case; (b) MISO model.

array antenna, the radiated signal can be focused in the desired direction of the user. In essence, a MISO system incorporates an electrically steerable high-gain antenna on the TX side.

Figure 2.2 illustrates a specific 3×1 MISO configuration, where three TX antennas transmit signals $x_1[n]$, $x_2[n]$, and $x_3[n]$ into the communication channel. The channel coefficients h_1, h_2, and h_3 multiply with the TX signals, resulting in a superimposed received signal

$$\begin{aligned} y[n] &= h_1 x_1[n] + h_2 x_2[n] + h_3 x_3[n] + w[n] \\ &= \begin{bmatrix} h_1 & h_2 & h_3 \end{bmatrix} \begin{bmatrix} x_1[n] \\ x_2[n] \\ x_3[n] \end{bmatrix} + w[n]. \end{aligned} \tag{2.3}$$

Then, the general MISO expression with k TX antennas is

$$\begin{aligned} y[n] &= \begin{bmatrix} h_1 & h_2 & \dots & h_k \end{bmatrix} \begin{bmatrix} x_1[n] \\ x_2[n] \\ \dots \\ x_k[n] \end{bmatrix} + w[n] \\ &= \mathbf{h}^{\mathrm{T}} \mathbf{x}[n] + w[n]. \end{aligned} \tag{2.4}$$

2.2.2 Channel Estimation and Precoding

For channel coefficient estimation, the k TX antennas initially transmit an orthogonal pilot signal

$$\mathbf{X}_p = \begin{bmatrix} \mathbf{x}_p^1 & \mathbf{0} & \dots & \mathbf{0} \\ \mathbf{0} & \mathbf{x}_p^2 & \dots & \mathbf{0} \\ \dots & \dots & \dots & \dots \\ \mathbf{0} & \mathbf{0} & \dots & \mathbf{x}_p^k \end{bmatrix}_{N \times k}. \tag{2.5}$$

The received pilot signal $\mathbf{y}_p$ is known with N samples, meaning that a Least-Squares (LS) estimation of the channel information, $\widehat{\mathbf{h}}$, can be expressed as:

$$\widehat{\mathbf{h}} = \left(\mathbf{X}_p{}^{\mathrm{T}}\mathbf{X}_p\right)^{-1}\mathbf{X}_p{}^{\mathrm{T}}\mathbf{y}_p. \tag{2.6}$$

The estimated $\widehat{\mathbf{h}}$ is then utilized for precoding. Zero-forcing (ZF) precoding, beginning with the Moore–Penrose pseudoinverse, is one such method

$$\mathbf{p} = \left(\widehat{\mathbf{h}}\widehat{\mathbf{h}}^{*}\right)^{-1}\widehat{\mathbf{h}}. \tag{2.7}$$

For MISO beamforming, where there is no multi-user interference in the channels, the TX can radiate maximum power to maximize the RX SNR. A precoder where only the phase information is retained proves to be optimum

$$\mathbf{p}_{\mathrm{BF}} = \mathrm{e}^{\mathrm{j}\angle\mathbf{p}}. \tag{2.8}$$

The ZF MISO beamforming expression for user signal $\tilde{x}\,[n]$ is

$$\mathbf{x}\,[\mathrm{n}] = \mathbf{p}_{\mathrm{BF}}\tilde{x}\,[n]. \tag{2.9}$$

Maximum ratio transmission (MRT) precoding, also known as a matched filter or conjugate beamforming, maximizes signal power for RX users by conjugate matching with the channel matrix [18]. MRT precoding involves the multiplication of the uniform-amplitude conjugated estimated channel information and user data

$$\mathbf{x}\,[\mathrm{n}] = \mathrm{e}^{-\mathrm{j}\angle\widehat{\mathbf{h}}}\tilde{x}\,[n]. \tag{2.10}$$

2.3 MIMO Communication Fundamentals

The MIMO communication fundamentals explore the MIMO model, channel matrix decomposition, precoding, and capacity expressions.

2.3.1 MIMO Model

Expanding the number of TX and RX antennas increases the potential independent channels between RX users and TX. Figure 2.3 illustrates the principles of MIMO technology, showcasing both single-user (Figure 2.3a) and multi-user (Figure 2.3b) scenarios. Both cases are modeled in Figure 2.3c, where the received signals, y_1 and y_2, are linear combinations of channel elements, RX signals, and additive noises

$$\begin{aligned}\begin{bmatrix} y_1\,[n] \\ y_2\,[n] \end{bmatrix} &= \begin{bmatrix} h_{11}x_1\,[n] + h_{12}x_2\,[n] + h_{13}x_3\,[n] + w_1\,[n] \\ h_{21}x_1\,[n] + h_{22}x_2\,[n] + h_{23}x_3\,[n] + w_2\,[n] \end{bmatrix} \\ &= \begin{bmatrix} h_{11} & h_{12} & h_{13} \\ h_{21} & h_{22} & h_{23} \end{bmatrix}\begin{bmatrix} x_1\,[n] \\ x_2\,[n] \\ x_3\,[n] \end{bmatrix} + \begin{bmatrix} w_1\,[n] \\ w_2\,[n] \end{bmatrix}.\end{aligned} \tag{2.11}$$

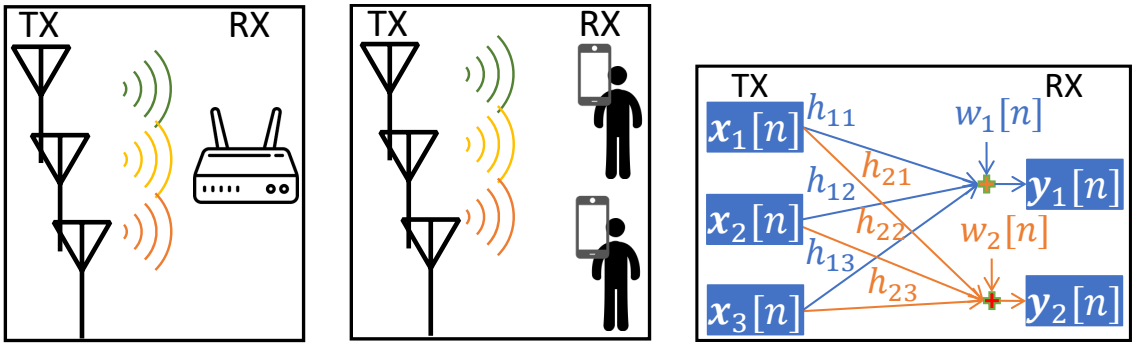

(a) (b) (c)

Figure 2.3: Principal illustration of (a) single-user MIMO case; (b) multi-user MIMO case; (c) general MIMO model.

Here, h_{11}, h_{12}, and h_{13} are channel elements from TX antennas to RX antenna one, while h_{21}, h_{22}, and h_{23} are channel elements from TX antennas to RX antenna two. Three TX signals of x_1, x_2, and x_3. The additive noise contributions are w_1 and w_2 for two RX signals.

In a general MIMO system with k TX and r RX antennas, the expression becomes

$$\begin{bmatrix} y_1[n] \\ \dots \\ y_r[n] \end{bmatrix} = \begin{bmatrix} h_{11} & h_{12} & \dots & h_{1k} \\ \dots & \dots & \dots & \dots \\ h_{r1} & h_{r2} & \dots & h_{rk} \end{bmatrix} \begin{bmatrix} x_1[n] \\ x_2[n] \\ \dots \\ x_k[n] \end{bmatrix} + \begin{bmatrix} w_1[n] \\ \dots \\ w_r[n] \end{bmatrix}, \tag{2.12}$$

or in a matrix form

$$\mathbf{y} = \mathbf{H}\mathbf{x} + \mathbf{w}. \tag{2.13}$$

where $\mathbf{x}$ is the transmitted signal with $k \times 1$ dimension, and k is the number of TX antennas. $\mathbf{y}$ is the received signal vector with $r \times 1$ dimension. $\mathbf{w}$ is an additive channel noise vector with $r \times 1$ dimension.

2.3.2 Channel Matrix Decomposition

The singular value decomposition of a $r \times k$ complex matrix $\mathbf{H}$ is given by

$$\begin{aligned} \mathbf{H} &= \mathbf{U}\mathbf{\Sigma}\mathbf{V}^* \\ &= \begin{bmatrix} u_{11} & u_{12} & \dots & u_{1r} \\ u_{21} & u_{22} & \dots & u_{2r} \\ \dots & \dots & \dots & \dots \\ u_{r1} & u_{r2} & \dots & u_{rr} \end{bmatrix} \begin{bmatrix} \sigma_{11} & 0 & \dots & 0 \\ 0 & \dots & \dots & 0 \\ \dots & \dots & \sigma_{ii} & \dots \\ 0 & 0 & \dots & \dots \end{bmatrix} \begin{bmatrix} v_{11} & v_{12} & \dots & v_{1k} \\ v_{21} & v_{22} & \dots & v_{2k} \\ \dots & \dots & \dots & \dots \\ v_{k1} & v_{k2} & \dots & v_{kk} \end{bmatrix}^*, \end{aligned} \tag{2.14}$$

where $\mathbf{U}$ is a $r \times r$ complex unitary matrix, $\mathbf{\Sigma}$ is a $r \times k$ rectangular diagonal matrix with non-negative real numbers on the diagonal, $\mathbf{V}$ is a $k \times k$ complex unitary matrix, and $\mathbf{V}^*$ is the conjugate transpose of $\mathbf{V}$. Such decomposition exists for any complex matrix. The matrices $\mathbf{U}$ and $\mathbf{V}$ have the property that $\mathbf{U}^* = \mathbf{U}^{-1}$ and $\mathbf{V}^* = \mathbf{V}^{-1}$,

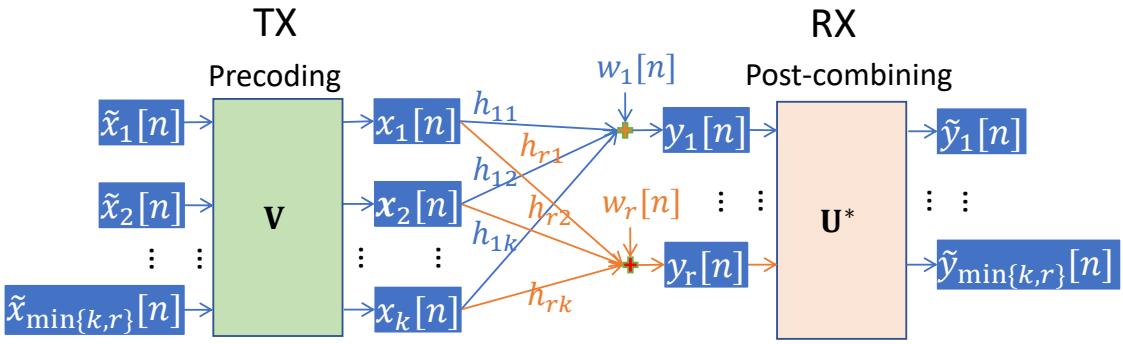

Figure 2.4: The MIMO model with precoding and post-combining.

which means the conjugate transpose is the same as the inverse. The diagonal entries $\sigma_{\mathbf{ii}}$ of $\mathbf{\Sigma}$ are uniquely determined by $\mathbf{H}$ and are known as the singular values of $\mathbf{H}$. The number of non-zero singular values is equal to the rank of $\mathbf{H}$, which is also the number of independent sub-channels that the MIMO system can ideally support [19].

Figure 2.4 explains precoding and post-combining based on the matrix $\mathbf{V}$ and $\mathbf{U}^*$, resulting in independent MIMO channels

$$\begin{cases} \tilde{\mathbf{y}} = \mathbf{U}^*\mathbf{y} \\ \tilde{\mathbf{x}} = \mathbf{V}^*\mathbf{x} \\ \tilde{\mathbf{w}} = \mathbf{U}^*\mathbf{w}. \end{cases} \tag{2.15}$$

The resulting channel model is

$$\tilde{\mathbf{y}} = \mathbf{\Sigma}\tilde{\mathbf{x}} + \tilde{\mathbf{w}}. \tag{2.16}$$

Here, the original transmitted signal $\tilde{\mathbf{x}}$ defines the final received signal $\tilde{\mathbf{y}}$ through the diagonal matrix $\mathbf{\Sigma}$.

2.3.3 Channel Estimation and Precoding

Channel estimation involves estimating the channel matrix $\mathbf{H}$, and the LS principle is applied to minimize channel estimation errors [20]. The LS algorithm calculates the channel information $\widehat{\mathbf{H}}$ using transmitted pilot signals $\mathbf{X}_\mathrm{p}$ and received pilot signals $\mathbf{Y}_\mathrm{p}$

$$\widehat{\mathbf{H}} = \left(\mathbf{X}_\mathrm{p}{}^\mathrm{T}\mathbf{X}_\mathrm{p}\right)^{-1}\mathbf{X}_\mathrm{p}{}^\mathrm{T}\mathbf{Y}_\mathrm{p}. \tag{2.17}$$

For MU-MIMO, where there is no post-combining at the RX due to the lack of collaboration, only precoding at the TX is explained. ZF precoding, a commonly used method, aims to minimize multi-user interference. The ZF MIMO precoder is derived from the Moore–Penrose pseudoinverse of the estimated channel matrix

$$\mathbf{P} = \left(\widehat{\mathbf{H}}\widehat{\mathbf{H}}^*\right)^{-1}\widehat{\mathbf{H}}. \tag{2.18}$$

The ZF precoding of user data $\tilde{\mathbf{x}}$ is done according to

$$\mathbf{x} = \mathbf{P}^{\mathrm{T}}\tilde{\mathbf{x}}. \tag{2.19}$$

MRT precoding operates by conjugate matching with the channel matrix. User data is multiplied by the conjugate transpose of the estimated channel information

$$\mathbf{x} = \widehat{\mathbf{H}}^{\mathrm{H}}\tilde{\mathbf{x}}. \tag{2.20}$$

Here comes the MRT preceded MIMO transmission signal.

2.3.4 Capacity Expressions

MIMO introduces spatial diversity to wireless systems, increasing channel capacity by utilizing channel information and exploiting parallel channels. The sum MIMO capacity [19] is expressed by

$$C_{\mathrm{MIMO}} = \sum_{m=1}^{M} B \log_2 \left(1 + \sigma_m^2 \frac{S}{N}\right) [\mathrm{bit/s}], \tag{2.21}$$

where C_{MIMO} is the sum MIMO capacity, σ_m^2 is the channel weight which is decided by the singular values of the channel matrix. This equation assumes an identical $\frac{S}{N}$ for all channels. The number of independent channels, M, is determined by the rank of $\mathbf{H}$. In theory, increasing the channel number can linearly increase MIMO capacity. However, actual MIMO capacity also depends on non-line-of-sight conditions and interference [21]. Simulations alone are insufficient to fully demonstrate the capability of the MIMO system. Hence, this thesis will discuss MIMO testbeds and study the capacity of MIMO cases through experiments and simulations.

2.4 Wireless MIMO Technology

MIMO technology is a crucial enhancement for wireless communication, significantly boosting capacity, as explained in the preceding section. A requirement for effective MIMO operation is the phase coherence among TXs. This section provides an overview of three MIMO architectures: C-MIMO, D-MIMO, and cell-free MIMO.

2.4.1 Co-located MIMO

The traditional and straightforward implementation of MIMO is C-MIMO, where multiple closely located antennas at the TX side transmit signals to multiple RXs. This method employs an array antenna, such as a linear, planar, or circular array, to enhance antenna gain and improve signal SNR. Users are served coherently by all antennas in the same time-frequency resources but separated spatially, receiving directive and distinct signals.

However, C-MIMO faces challenges in user interference, especially as user density increases. Figure 2.5a illustrates that signals from TX antennas are too close, leading to interference and reduced channel diversity, particularly in high-frequency bands. These limitations cannot be easily suppressed as long as we rely on co-located implementations [14].

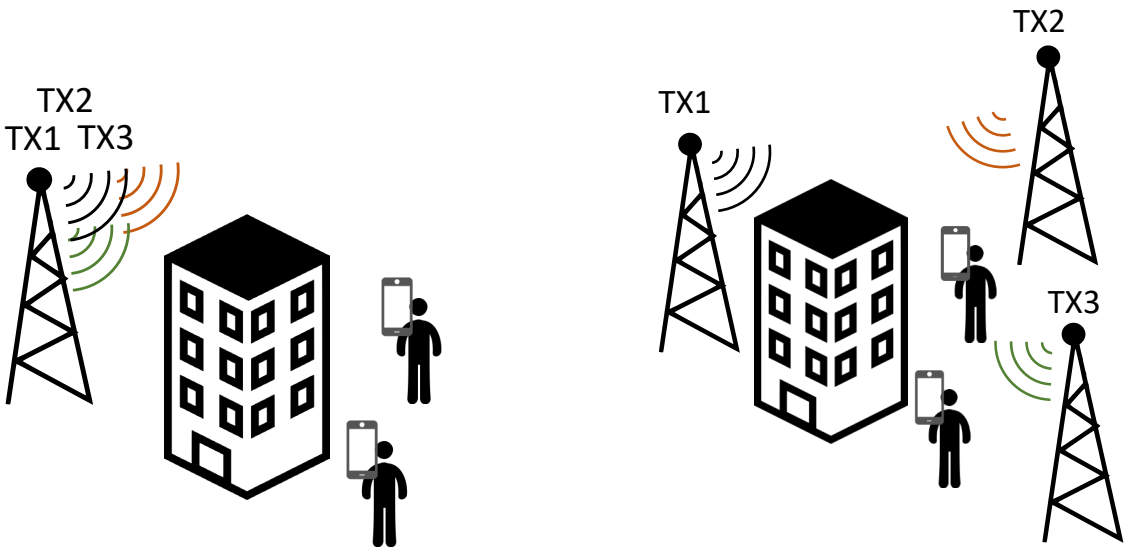

(a) (b)

Figure 2.5: A specific case of (a) C-MIMO introduces interference. (b) D-MIMO has a better possibility to cover users irrespective of their location .

2.4.2 Distributed MIMO

To address the limitations of C-MIMO, D-MIMO systems deploy multiple distributed TXs. Physically distributed antennas with different TXs mitigate signal coupling issues and are more likely to establish line-of-sight communication with RX. Figure 2.5b exemplifies D-MIMO technology with three distributed TXs serving users. D-MIMO is particularly beneficial in high-density urban areas, offering a more uniform service [22]. This approach aims to improve data service quality, especially in scenarios where wireless connectivity supports critical functions like payments, navigation, forums, and autonomous vehicle control.

2.4.3 Cell-free MIMO

The term "cell-free" implies the absence of cell boundaries during data transmission. In a cell-free MIMO system, RRHs in the network collaborate to jointly serve users without predefined cell areas. RRHs are connected via fronthaul connections to a CU responsible for coordination. Figure 2.6a illustrates the cell-free MIMO concept, where RRHs cooperate to dynamically serve users without specific area definitions. In contrast to cellular systems, where each RRH serves a designated area, cell-free MIMO provides a more user-centric and dynamic communication environment. Figure 2.6 compares cellular MIMO with cell-free MIMO network implementation, highlighting the dynamic and load-balanced nature of the latter. Cell-free MIMO offers a more user-centric communication system with load balancing among RRHs.

In contrast, a cellular communication system operates with each RRH having a designated serving area bounded by specific boundaries, connecting only with users within that area. Notably, the signal power experiences rapid decay with

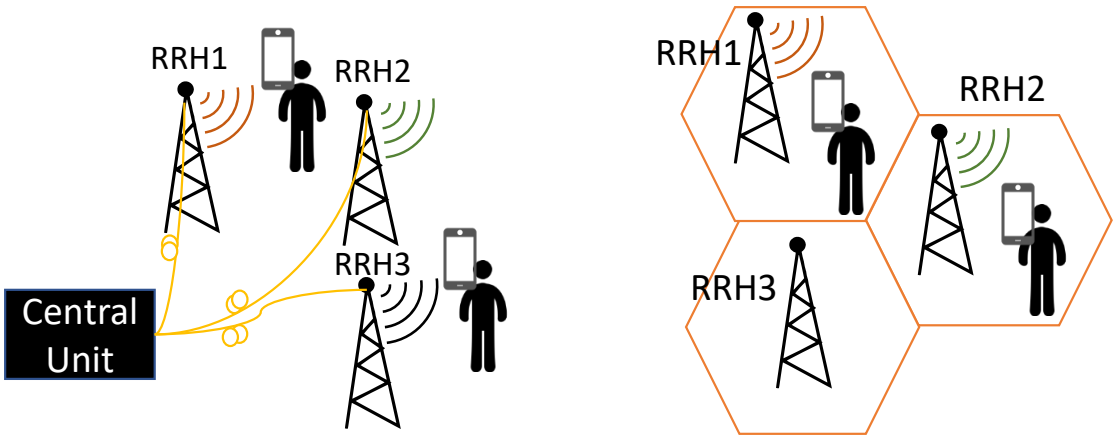

(a) (b)

Figure 2.6: (a) The cell-free system is user-centralized. (b) The cellular system has an unbalanced load.

increasing propagation distance. Users near the center of a cell, close to a RRH, will enjoy a higher SNR compared to those positioned at the cell edge between two cells. It is common for there to be a significant difference of up to 50 dB (or 100,000 times) in power level between the cell center and the cell edge [23]. Additionally, users at the cell edge may face interference from neighboring RRHs [22]. In mobile communication systems, users can move around the cell edge, traversing cell boundaries back and forth. Managing the resources for users at the cell edge becomes challenging for cellular systems, as cells must release and frequently schedule resources to accommodate these users. As a result, cellular communication systems often provide a nonuniform service. Figure 2.6b exemplifies a specific scenario where RRH1 and RRH2 are busy, while RRH3 remains free due to the predefined cellular system boundaries.

In summary, C-MIMO, D-MIMO, and cell-free MIMO architectures each address specific challenges and requirements in wireless communication, providing diverse solutions for different scenarios and user demands. The implementation and RoF architectures for these MIMO technologies are further explored in Sections 2.5 and 2.6.

2.5 Wireless MIMO Transmitter Implementations

This section covers the TX implementations for wireless C-MIMO/D-MIMO technologies.

2.5.1 Co-located MIMO Implementations

In C-MIMO implementations, all necessary components for MIMO communication, including antennas, electronics, and signal processing, are consolidated into a single

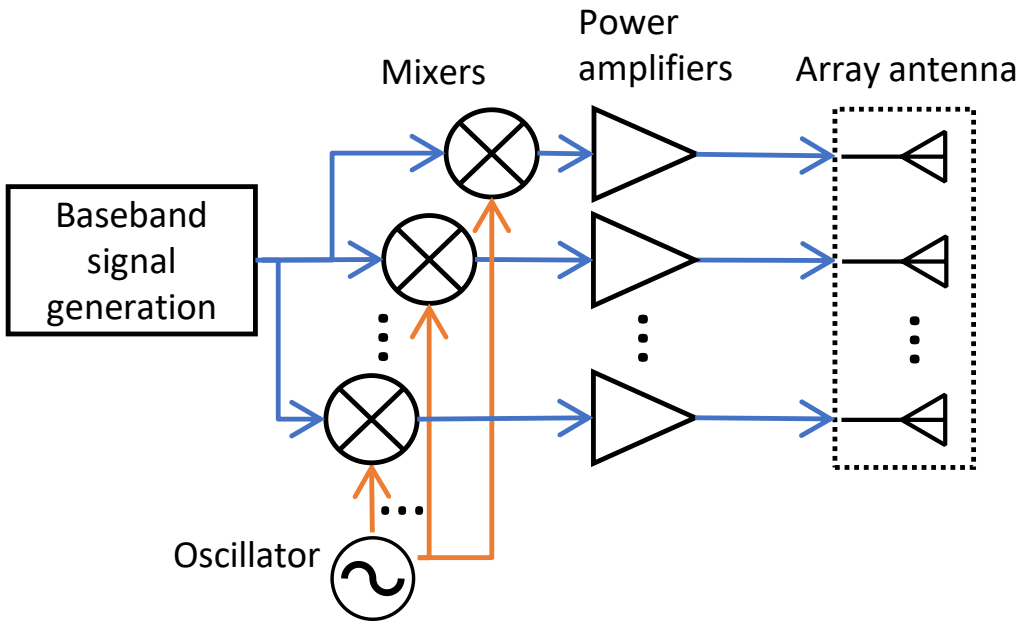

Figure 2.7: A simplified block diagram of a general transmitter structure for C-MIMO implementations.

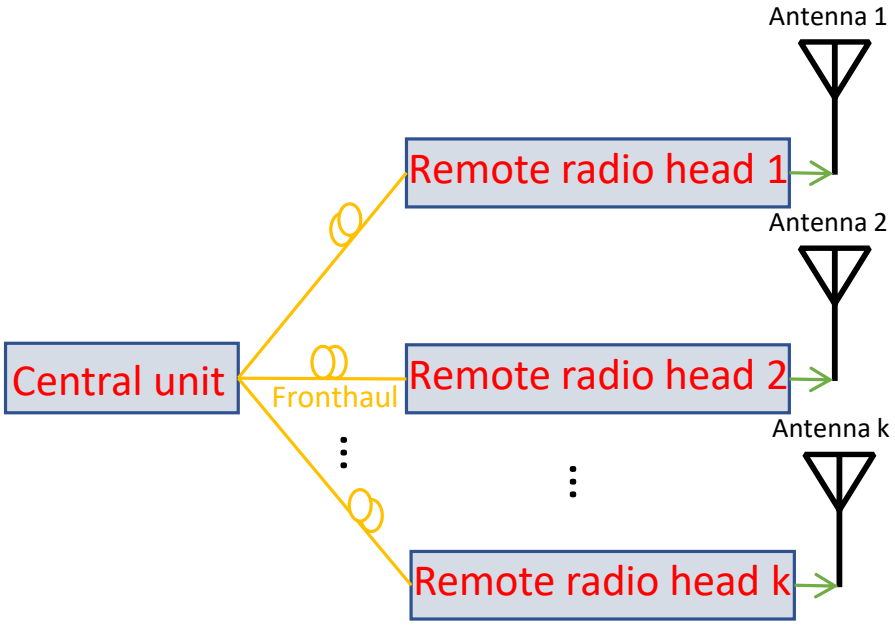

Figure 2.8: The D-MIMO transmitter implementation illustration.

unit. The key advantage is that all branches can share the same local oscillator (LO), facilitating the maintenance of phase coherence between channels—an essential requirement for MIMO.

In Figure 2.7, several branches, including a power amplifier (PA) and a mixer for an array antenna, are typical features of C-MIMO implementations. The input signal undergoes upconversion through the mixer and oscillator to generate a RF signal. Filters are employed to suppress unwanted spectrum components and maintain the

target frequency. Depending on specific applications, modifications to this structure are necessary. For instance, a high-frequency communication system might require multiple upconversion stages, and an amplifier stage could precede the mixer if the baseband signal is weak. In summary, C-MIMO TXs produce RF signals with sufficient power for transmission to the array antenna.

2.5.2 Distributed MIMO Implementations

D-MIMO, on the other hand, necessitates physically distributed RRHs to introduce channel diversity. The fronthaul connection, as depicted in Figure 2.8, separates the CU and the RRH. This architectural choice allows the CU to centrally process MIMO technology for distributed RRHs, which simplifies their implementation. The fronthaul connection is crucial for maintaining coherent signals for RRHs, as is required for MIMO technology to work.

2.6 Radio-over-Fiber Technology

For D-MIMO implementations, RoF technology is commonly employed. RoF technology supports various architectures, as described in this section.

2.6.1 Architecture

Optical fiber, known for its low cost and low attenuation (down to approximately 0.2 dB/km) of optical signals, enables the deployment of RRHs at remote locations, several kilometers apart. RoF architectures are already mature in 4G and 5G radio access network (RAN) deployments [24] [25].

As illustrated in Figure 2.9, there are generally three main types of RoF implementations for the low-frequency (sub-6 GHz) band: analog radio-over-fiber (ARoF), digital radio-over-fiber (DRoF) [26], [27], and SDoF [28]–[30]. The modern CU incorporates a digital signal processing (DSP) unit for baseband signal processing.

ARoF generates an analog RF signal at the CU using a digital-to-analog converter (DAC). An electrical/optical (E/O) converts the electric RF signal to an optical signal for a fiber transmission. In the RRH, an optical/electrical (O/E) recovers the electric RF signal before a PA stage. However, such an ARoF may face distortion issues due to impairments in the optical domain [31] [32].

In contrast, DRoF shifts the DAC to the RRH, transmitting digitized RF signals through the fiber connection, as in Figure 2.9b. The digital nature of the signal mitigates distortion problems. However, the need for a DSP unit in the RRH to manage signal protocols between the O/E converter and DAC introduces complexity [26] [27]. This DSP requirement makes the DRoF structure more complicated and not an optimum choice for massive MIMO deployment. A high-speed DAC is usually really expensive and has high energy consumption. Therefore, the DAC is another limitation in the ARoF and DRoF structure.

Some studies propose the SDoF architecture, which simplifies the RRH [28]–[30], overcoming some limitations of ARoF and DRoF. In this structure, the CU employs

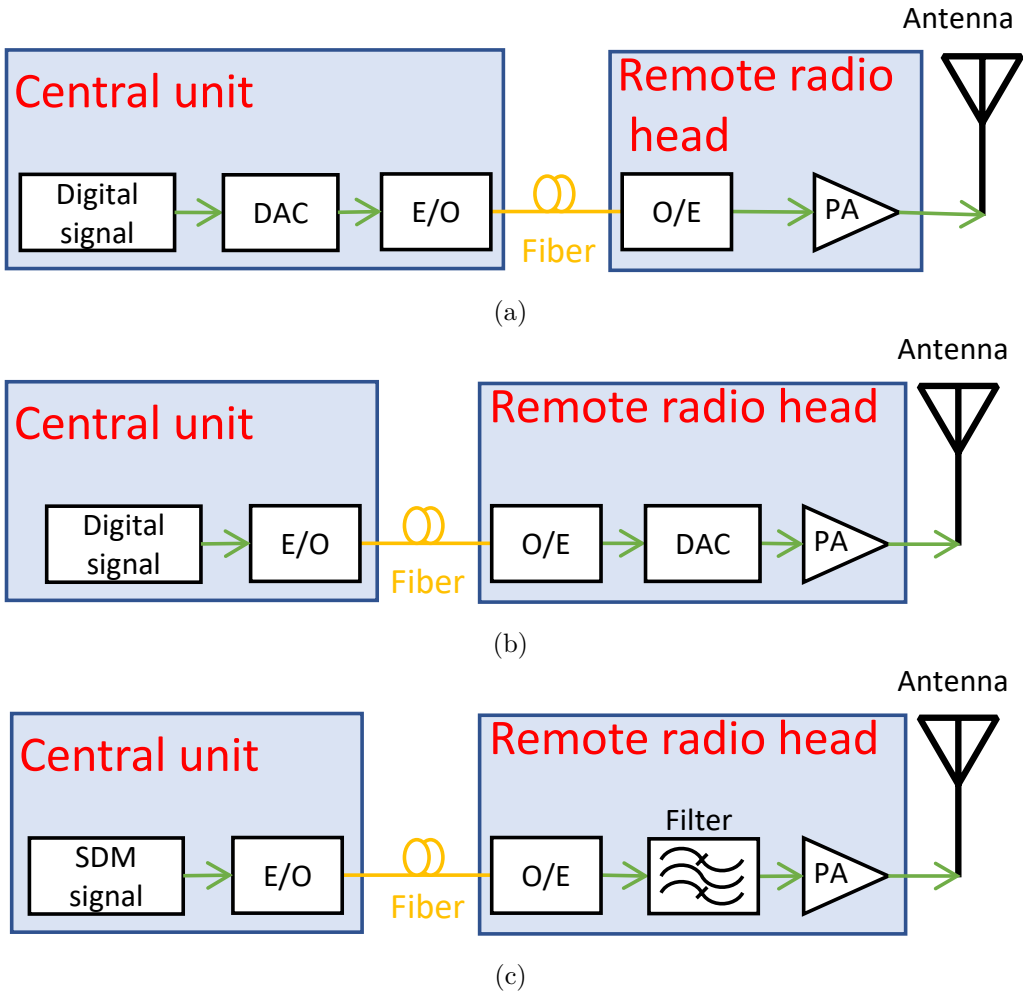

Figure 2.9: The principle illustration of (a) Analog Radio-over-Fiber. (b) Digital Radio-over-Fiber. (c) Sigma-Delta-over-Fiber .

bandpass sigma-delta modulation (BPSDM) with a digital RF signal to generate bit-streams for the fiber connection, as in Figure 2.9c. The RRH only requires a bandpass filter (BPF) to recover the analog RF signal, eliminating the need for a DAC.

While these RoF architectures are suitable for the low-frequency band, improvements are required for the mm-wave band (above 24 GHz). For example, RoF architectures need to generate mm-wave signals either at CU or RRH [33], and the fiber connection must support broad bandwidth signals.

2.6.2 MIMO Applications

RoF technology evolves the implementation of MIMO system applications by keeping centralized intensive computations in the CU. Furthermore, the fiber-supported high data throughput transmits over phase coherent RRHs [34]. Such a CU-scheduled implementation leads to the centralized radio access network (C-RAN) in current 4G and 5G communication networks [4] [35].

2.7 Chapter Conclusion

This chapter has provided an overview of the system model and capacity for SISO/MISO/MIMO technologies. In wireless MIMO communication, D-MIMO technology lays the foundation for the cell-free MIMO system concept. RoF can be an important technology for MIMO in general but D-MIMO in particular.

Chapter 3

Experimental Evaluation of Wireless MIMO Systems

MIMO technology enhances wireless communication system capacity to accommodate an increasing number of users, as theoretically elaborated in Chapter 2. This chapter examines available testbeds for statistically exploring MIMO capacity in realistic environments through experiments. Additionally, MIMO simulations are included as a crucial tool for comparing and validating the experimental results obtained.

3.1 Wireless Communication Testbeds

Theoretical concepts and mathematical simulations often oversimplify noise and propagation parameters in real-world, multipath-rich environments. Therefore, a proof-of-concept prototyping system is essential for validating actual MIMO communication performance. This section presents MIMO testbeds from academia and industry, categorizing them into C-MIMO and D-MIMO configurations.

3.1.1 C-MIMO Communication Testbeds

In 2014, the collaboration between the University of Bristol and Lund University resulted in the reporting of Lund University massive MIMO (LuMaMi) system, featuring a 'T' shaped array antenna with 160 dual-polarized elements [36]. LuMaMi supports configurations such as 4×25 and 10×10. The testbed platform connects the upper part of the 'T' shape, with 4×25 elements, to 50 software-defined radios (SDRs), each equipped with two independent RF transceivers. These SDRs operate with a 20 MHz bandwidth at a 3.7 GHz carrier frequency and are linked to a central processor through switch combiners. The central processor handles real-time uplink (UL)/DL data at an aggregated data throughput of 384 Gbps. LuMaMi, with its off-the-shelf hardware on a mobile trolley, has been used to conduct indoor and outdoor measurements, serving 12 simultaneously active users with ZF and MRT precoding in time division duplex (TDD) mode [37]. Results indicate the capability to separate up to 12 user devices on the same time/frequency resource when using massive MIMO. LuMaMi has also achieved communication with moving cars at

29 km/h velocity through channel state information and power control updates during measurements [38]. With moving car measurements, 100 RF signals are synchronized by a standard distributed reference clock and timing trigger at the base station. RXs are synchronized to the global positioning system (GPS) reference and primary synchronization signal of orthogonal frequency-division multiplexing (OFDM) symbols.

EURECOM, a French research center in Sophia Antipolis, operates the OpenAirInterface massive MIMO testbed, an open-source long-term evolution (LTE) compliant base station equipped with a 64-element array antenna at a 2.6 GHz carrier frequency and 5 MHz bandwidth. Four commercial user terminals simultaneously connect to the internet service through this massive MIMO testbed in TDD mode [39].

Apart from academic testbeds, there are also C-MIMO research results or products from industry. A full-dimension MIMO base-station prototype at Samsung Research, featuring an array antenna with 8×4 dual-polarized patch elements connecting 32 transceivers [40]. During the indoor/outdoor measurements, 12 user terminals get real-time LTE service at 3.5 GHz carrier frequency with 20 MHz bandwidth by sharing the same time/frequency resources [40]. Ericsson has AIR6428, with 64 transceivers for 192 antenna elements, supporting wideband MIMO with sub 6-GHz frequency band configurations for various urban scenarios [41]. Ericsson introduces 2×1, 4×1, and 8×1 sub-array MIMO configurations for dense urban high-rise, urban low-rise, and rural areas respectively [42]. At the same time, Nokia's AirScale massive MIMO Adaptive Antenna also has 64 transceivers and made a joint beamforming demonstration with a U.S. operator at Mobile World Congress in Barcelona, Spain [43].

3.1.2 D-MIMO Communication Testbeds

Katholieke Universiteit Leuven (Belgium) has developed a D-MIMO testbed [44] for outdoor environments, which has been used for analysis of infrastructure sharing spectrum efficiency. This KU Leuven D-MIMO testbed, each based on a previous MIMO testbed in [45], incorporates two base stations with a 32-patch element array antenna. All antenna elements have independent RF signals from SDRs and radiate 20 MHz LTE signal at 2.6 GHz carrier frequency in TDD mode. The outdoor measurement results conclude that the D-MIMO configuration significantly increases spectrum efficiency with minimum-mean squared error (MMSE) precoding. Furthermore, the testbed tackled the inter-user interference problem in an indoor experiment [46]. Some researchers proposed a new RAN concept of RadioWeaves [47] based on this testbed. The measurements in [48] validate the advantages of RadioWeaves (planar distributed) topology by comparing it with Ericsson's RadioStripes (linear distributed topology) [49].

Recently, Samsung Research upgraded the C-MIMO testbed [40] to a D-MIMO configuration, incorporating three RRHs connected to a CU through a common public radio interface (CPRI)-enabled fiber connection [26]. Each RRH features a single antenna panel with four dual-polarized antenna elements, a field programmable

gate array (FPGA) board equipped with eight high-speed data converters, and RF circuits. For D-MIMO measurement results, this testbed introduces a users-assisted OTA channel calibration method for seven user terminals operating at a 3.5 GHz carrier frequency with a 20 MHz LTE signal [26].

Another digital fronthaul D-MIMO testbed [27] is established on the open-source OpenAirInterface platform from EURECOM [39]. This D-MIMO testbed, built on DRoF technology, consists of two remote RRHs, each featuring two antennas. The CU is interconnected with the RRHs through Ethernet fronthaul links and facilitates commercial internet access. Operating in frequency division duplex (FDD) mode, the DL/UL frequencies are set at 2.66 GHz/2.54 GHz, respectively. In measurements, two commercial user terminals access internet services from the testbed, employing six combinations of 5/10/20 MHz bandwidth signals and two distinct fronthaul function splits. The systems evaluate the occupied resources for each combination [27].

University of Ghent (Belgium) has developed a real-time SDM-enabled 2×2 D-MIMO system operating at a 3.5 GHz carrier frequency with a 163.84 MHz bandwidth [29]. This system demonstrates indoor D-MIMO communication in seven scenarios for comparison with SISO cases. The scope of this work has been expanded to include UL direction with two RRHs, each equipped with four antenna elements [30]. The antennas operate in TDD mode, allowing UL and DL to share the same frequency by employing switching mechanisms [30]. Another SDoF-based massive D-MIMO testbed has been developed at Chalmers, featuring 12 distributed RRHs, and operates at a 2.365 GHz carrier frequency with a single-carrier 35 MHz 64-quadrature amplitude modulation (QAM) signal [28]. This massive D-MIMO testbed facilitates a simple C-RAN structure by incorporating offline signal processing and demonstrates superior communication signal quality compared to the C-MIMO case in indoor measurements.

In Paper [A], a user terminal integrated with a robot car is conceived, transforming the SDoF-based massive D-MIMO testbed [28] into an automated platform suitable for various MIMO measurements. The extensive measurement outcomes presented in Paper [A] provide experimental evidence demonstrating the statistical capacity advantage of the D-MIMO system over the C-MIMO system. Section 3.3 will discuss the specifics of the MIMO measurements and the results of their statistical analysis.

3.2 Communication Simulations

This section will study the simulations of MIMO capacity. A theoretical understanding of MIMO capacity is a valuable reference for reality measurements.

3.2.1 MIMO Simulation Example

The simulation results presented in [50] deploys 100 RRHs for 40 users, operating at a 1.9 GHz carrier frequency with a 20 MHz bandwidth. The model takes into account channel estimation and power control capabilities, creating a configuration close to real-world scenarios. In [50], the simulations are conducted for user capacity

in both cell-free Massive MIMO (D-MIMO) and small-cell Massive MIMO (C-MIMO) under conditions of uncorrelated and correlated fading. The findings indicate that D-MIMO enhances user capacity by fivefold in uncorrelated fading and tenfold in correlated fading compared to C-MIMO. The asymptotic analysis in [51] establishes that D-MIMO achieves more significant capacity gains than C-MIMO when the system incorporates a large number of antennas. Analytical and simulation results in [52] study a specific case involving a high-speed train with a MIMO system, concluding that D-MIMO provides more uniformly distributed user capacity than C-MIMO. It is important to note that these simulations lack an actual measurement reference for comparison.

3.2.2 Raytracing MIMO Simulation

The study described in [53] involves an indoor MIMO simulation utilizing a raytracing method based on geometrical optics. The simulated narrowband signal frequency is set at 2.45 GHz, involving four TXs and 2500 receiving positions. The simulation model focuses on line-of-sight propagation, allowing a maximum reflection number of three for six MIMO cases (three C-MIMO and three D-MIMO). The results generate a capacity map for all cases, highlighting that D-MIMO exhibits a more uniform capacity distribution for an independent identically distributed (IID) fading channel.

In a recent master thesis project, conducted at Chalmers, MIMO communication is studied using raytracing-based electromagnetic propagation [54]. This thesis work obtains the MIMO channel response as a complex value by comparing the phase/amplitude information between the original and propagated signals. Subsection 3.3.4 provides detailed MIMO simulation results, while subsection 3.3.5 offers a comparison between the simulation and measured results.

3.3 Comparison Between C-MIMO and D-MIMO in an Indoor Environment

The findings of [55] assert that D-MIMO has the capability to reduce the distance to users and provides a larger capacity gain compared to traditional MIMO when equal-power allocation is applied. The channel model outlined in [55] takes into account factors such as path-loss, log-normal fading, and Rayleigh fading, leading to the conclusion that the location of the RX has a significant impact on MIMO capacity. This section conducts a statistical comparison between C-MIMO and D-MIMO in an indoor environment.

3.3.1 Environment Description

The automated MIMO testbed described in paper [A] was utilized to conduct C-MIMO and D-MIMO measurements within an indoor office area measuring 8 m $\times$ 10 m. This area encompasses diverse multipath environments, including an open office space, individual offices, a kitchen, a meeting room, and laboratories. The

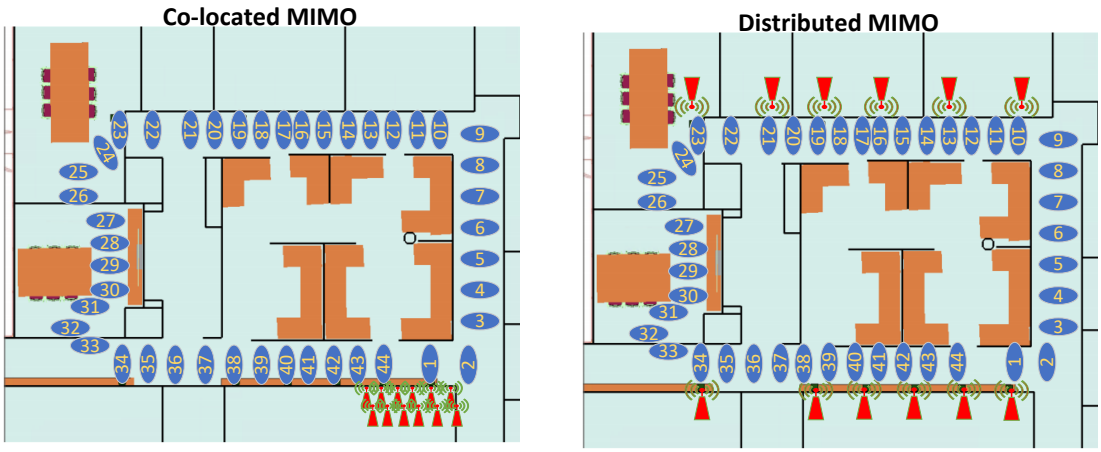

(a) (b)

Figure 3.1: The MIMO antenna configuration with measured positions in the indoor 8 m × 10 m area. (a) C-MIMO; (b) D-MIMO.

layouts for C-MIMO and D-MIMO measurements are depicted in Figure 3.1a and Figure 3.1b, respectively. The sole distinction between the two sets of measurements lies in the locations of RRHs. In the C-MIMO measurement, all RRHs are positioned at one corner of the layout, mimicking a conventional setup. In contrast, the D-MIMO measurement evenly distributes RRHs throughout the entire area. In both scenarios, the automated RX sequentially collects channel information and MIMO data at positions marked from 1 to 44.

3.3.2 Experimental Setup

The publication [28] details a SDoF DL testbed featuring 12 independent RRHs for MIMO measurements. Paper [A] extends this system by incorporating an automatic RX for comprehensive MIMO studies. In Figure 3.2a, an indoor area is depicted with distributed RRHs, and the automatic robot-based RX has the flexibility to move freely. Figure 3.2b illustrates the automatic RX as a robot car equipped with a software-controlled RF RX (USRP [56]) featuring an omnidirectional antenna. Additionally, the automatic RX is equipped with an ultrasonic sensor, infrared sensors, and a camera to navigate and follow labeled measurement positions on the ground.

The automatic RX undergoes several steps at each position, as depicted in Figure 3.3. In the channel estimation procedure, the RRHs transmit the pilot signal in the initial step, and the automatic RX downconverts the received signal to the baseband in the subsequent step. Steps 3 – 6 involve frequency offset adjustment, resampling with preamble detection, matched filtering, timing adjustment, and downsampling, leading to the 7_{th} step of LS channel estimation. For the MIMO communication procedure, steps 8 – 10 encompass the generation of user data with ZF precoding. The automatic RX captures data again in the 11_{th} step for RX baseband signal processing, covering steps 12 - 16. After completing these 16 steps,

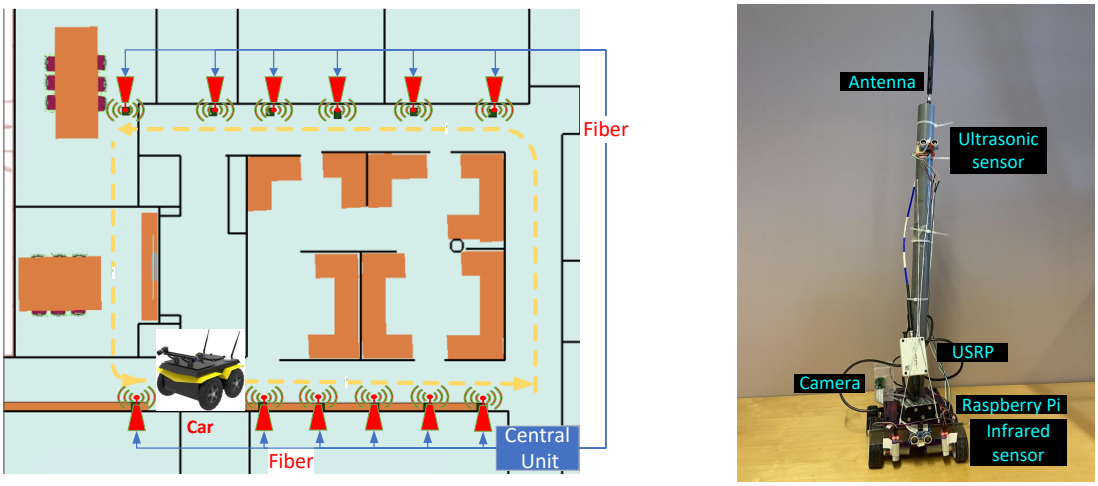

(a) (b)

Figure 3.2: The automatic MIMO measurement setup used for wireless communication experiments in the indoor 8 m × 10 m area. (a) Indoor measurement area; (b) The designed automatic receiver.

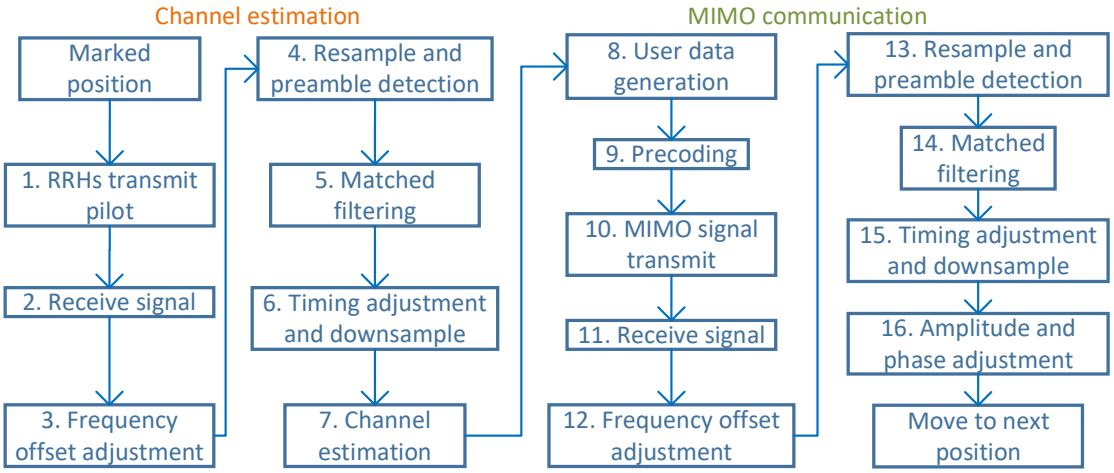

Figure 3.3: Operation procedure of the automatic MIMO measurement testbed [A].

the automatic RX concludes measurements at the current position and proceeds to the next one.

3.3.3 Experimental Results

Figure 3.4 presents a summary of the received power and normalized mean square error (NMSE) outcomes for C-MIMO and D-MIMO measurements at 44 positions with a 5 MHz bandwidth signal at a center frequency of 2.365 GHz. The NMSE curves exhibit fluctuations between -26 dB and -21 dB for both cases, indicating reasonable communication performance at all measurement positions. As shown in Figure 3.4, D-MIMO uniformly distributes power for users. In contrast, C-MIMO

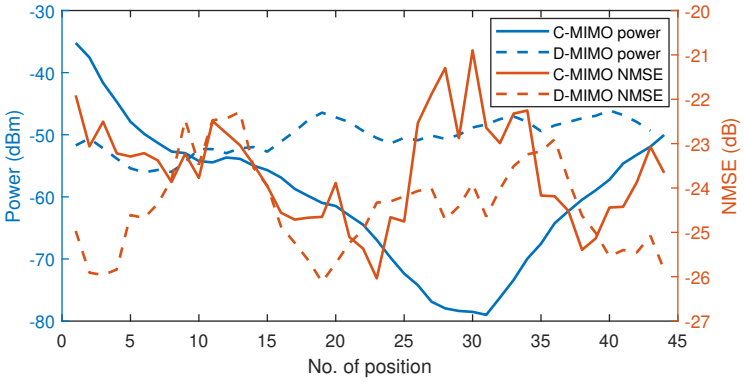

Figure 3.4: Power and NMSE results of the MIMO measurements from the indoor environment in Figure 3.1 [A].

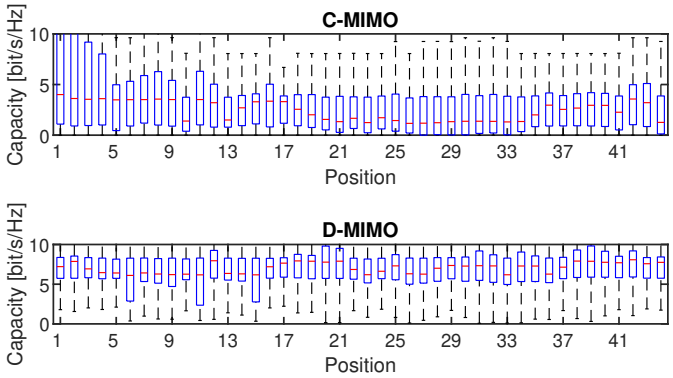

Figure 3.5: Boxplot of user capacity variation in MIMO measurements [A].

varies from -80 dBm to -35 dBm and experiences a significant drop for positions 23 – 35, which are not in the line-of-sight (refer to Figure 3.1).

From the collected channel matrix, the capacity expression of user m for MIMO cases is given by [57]

$$C_m = \log_2\left(1 + \sigma_m^2 \frac{S}{N}\right) [\text{bit/s/Hz}]\,, \tag{3.1}$$

where C_m is capacity for user m and $\frac{S}{N}$ is SNR. σ_m^2 is the channel weight and is the m^{th} eigenvalue obtained by singular value decomposition of the $12 \times M$ MIMO channel matrix with M users.

A hypothetical scenario involving 50,000 randomly generated sets of 4 user locations among the 44 positions has been analyzed for statistical purposes. Previously, Section 2.3.4 has discussed MIMO capacity with a constant SNR. Here, the corresponding user capacities have been computed using (3.1), leveraging eigenvalues obtained from the decomposition of the measured channel matrices, assuming a SNR of 30 dB. The user's capacity is influenced by combinations with the other three users. Figure 3.5 presents the distribution of user capacity in the form of a box

plot organized by location. In C-MIMO, the capacity exhibits significant variation depending on the positions of the other users, especially for positions 1-4, which are in proximity to the co-located RRHs. Positions situated farther away from C-MIMO antennas demonstrate lower capacity. In contrast, D-MIMO ensures a stable and higher median capacity for all positions.

3.3.4 Simulation Results

The automated testbed measurements documented in paper [A] summarize the results from in the master thesis report [54], which employs raytracing-based electromagnetic propagation within the simulation software [58]. The software necessitates a three-dimensional (3D) model of the measurement area, incorporating material parameters for walls, ceiling, floor, desks, and chairs. Figure 3.6 displays the 3D model with annotated positions, which also includes RRHs mirroring the real measurement setups. The simulation encompasses 831 user locations and generates 12×831 C-MIMO and D-MIMO channel responses, of which 12×44 channel responses are reserved for comparison with the actual measurements.

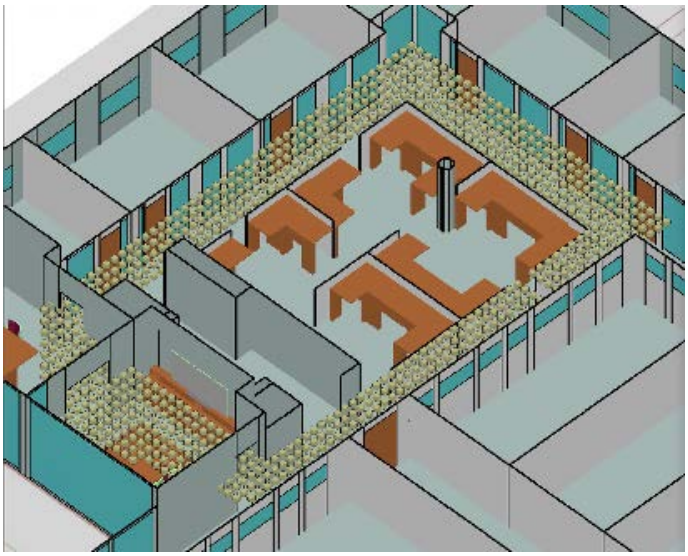

Figure 3.6: 3D simulation model with 831 user positions for the indoor 8 m $\times$ 10 m area [54].

The simulation software additionally provides a heatmap depicting power distribution, as illustrated in Figure 3.7. In the C-MIMO heatmap, an obvious low-power region is represented by green and blue colors, while the high-power area is concentrated around the co-located RRHs in one corner. In contrast, the D-MIMO heatmap exhibits a more uniform power distribution and lacks noticeable power variations.

The sum capacity is computed for a specific 12×4 scenario based on (3.1). Reducing the number of RRHs contributes to power savings but has an impact on channel capacity. As depicted in Figure 3.8, when eliminating one RRH, the C-MIMO user sum capacity drops to only 16 bit/s/Hz, while D-MIMO maintains a 20 bit/s/Hz user capacity. Even after removing 7 RRHs, D-MIMO still exhibits

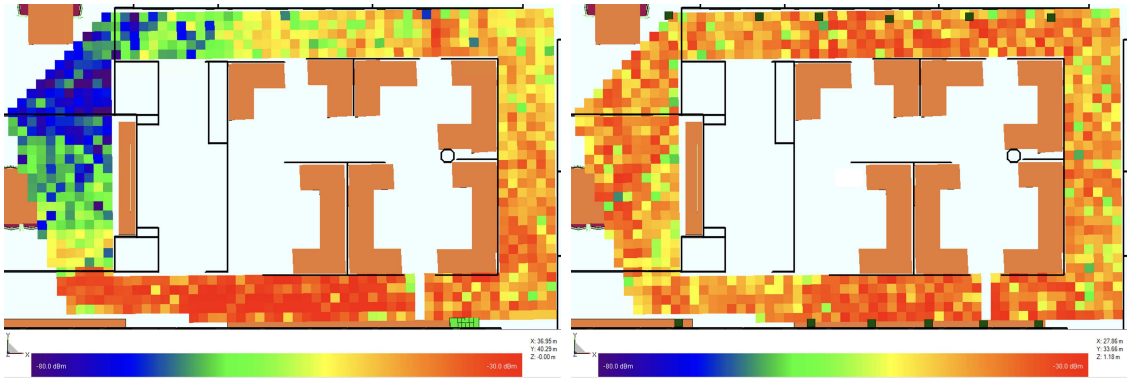

(a) C-MIMO (b) D-MIMO

Figure 3.7: Heatmap of MIMO received power [54].

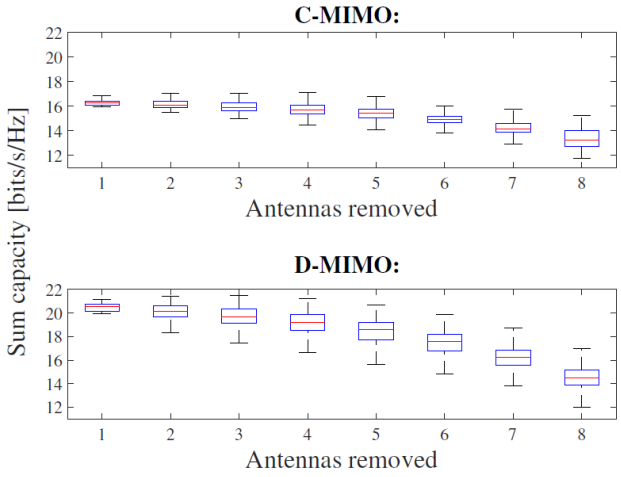

Figure 3.8: MIMO capacity variation when reducing the number of RRHs from 1 to 8 [B].

the same user capacity as C-MIMO with one RRH removed, demonstrating that D-MIMO can deliver equivalent service with fewer RRHs.

3.3.5 Measurement versus Simulation

As the measurements and simulations are conducted in the same indoor environment, a direct comparison of received power and user capacity probability can be carried out.

The MIMO received power in both measurements and simulations is depicted in Figure 3.9a and Figure 3.9b. D-MIMO received power displaying consistent fluctuations around -50 dBm. Meanwhile, C-MIMO exhibits relatively constrained received power at positions 23 - 35 in both measurements and simulation. Consequently, the MIMO received power demonstrates excellent alignment between measurements and simulation.

In a 12 $\times$ 44 MIMO scenario, randomly selecting 4 user positions from the 44

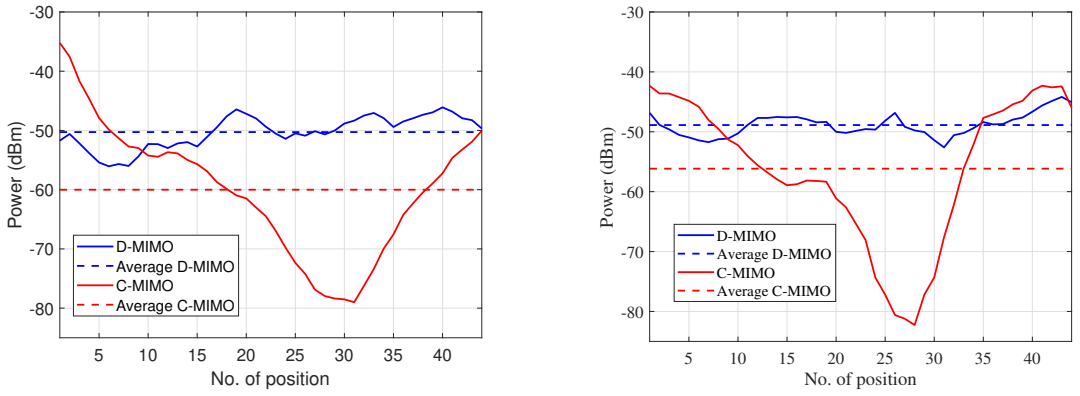

(a) (b)

Figure 3.9: Received power during MIMO transmission in (a) measurement (b) simulation [A].

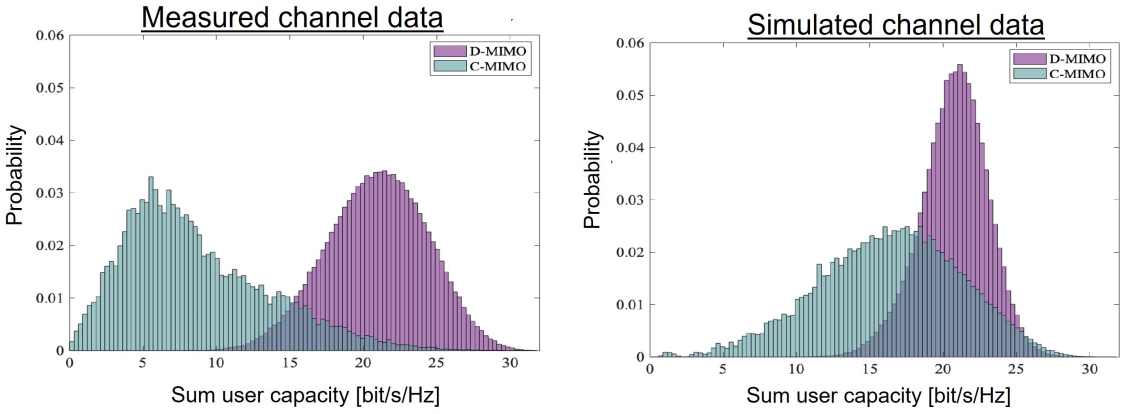

(a) (b)

Figure 3.10: The MIMO channel capacity histogram in [B]. (a) measurement; (b) simulation.

measured locations, there exist 135,751 unique 12×4 combinations. The user capacities for all possible combinations are computed using equation (3.1), and the resulting probabilities are illustrated in Figure 3.10a for measurements and Figure 3.10b for simulations. D-MIMO consistently exhibits a higher user capacity, averaging 22 bit/s/Hz, compared to C-MIMO, which has an average sum capacity of 7 bit/s/Hz (in measurements) and 16 bit/s/Hz (in simulations). Notably, the central user capacity for C-MIMO shows some variation between measurements and simulations, stemming from uncertainties in material parameters and geometric definitions. However, these disparities do not impact the overall findings and conclusions.

3.4 Chapter Conclusion

This chapter introduced an automated testbed designed for D-MIMO, C-MIMO, and various applications. Additionally, the chapter conducted a statistical analysis of

channel capacity based on measurements of D-MIMO and C-MIMO in an indoor environment. The capacity predictions, generated using raytracing-based electromagnetic propagation software, demonstrate reasonably consistent agreement with the measurement data.

Chapter 4

mm-wave RoF MIMO Link

To accommodate an increased number of user devices and data subscriptions, D-MIMO and corresponding RoF technology must operate on larger bandwidths, leading to higher data rates. The utilization of mm-wave signals can offer more bandwidth for RoF compared to lower-frequency bands. Additionally, MIMO technology plays a crucial role in mitigating the high path loss associated with mm-waves and enhancing capacity through spatial multiplexing. This chapter presents a comprehensive overview of existing mm-wave RoF architectures, supplemented with examples, and introduces an innovative mm-wave SDoF link architecture tailored for MIMO applications. The proposed architecture undergoes verification and demonstration, followed by conclusive findings.

4.1 mm-wave RoF Architectures

Section 2.5.2 outlines RoF architectures designed for low-frequency applications, which may not be well-suited for mm-wave frequencies. This section introduces various RoF architectures specifically tailored for mm-wave operations, beginning with those documented in existing literature.

4.1.1 Analog RoF

There are two mm-wave ARoF architectures depicted in Figure 4.1. Both architectures start with a digital intermediate frequency (IF) signal, as direct upconversion of a baseband signal to mm-wave frequency is impractical. Initiating with a digital IF signal not only simplifies the hardware connections of an in-phase/quadrature (I/Q) baseband signal but also mitigates potential I/Q imbalance issues. The first architecture illustrated in Figure 4.1a involves transmitting the analog IF signal from the CU to the RRH through a fiber connection. In the RRH, the IF signal is upconverted to mm-wave frequency through a mixer and an oscillator before being amplified by a PA and transmitted through the antenna. For analog beamforming RoF systems, the antenna would be a phased array antenna [59]. The second architecture shown in Figure 4.1b incorporates mm-wave conversion in the CU after the analog IF signal is generated by the DAC block. Consequently, the fiber transmits

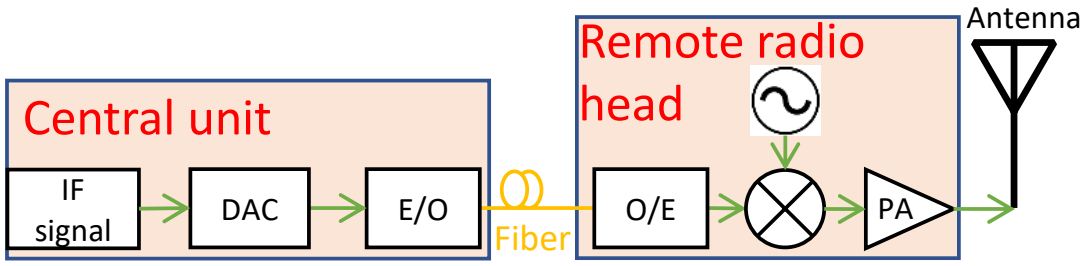

(a)

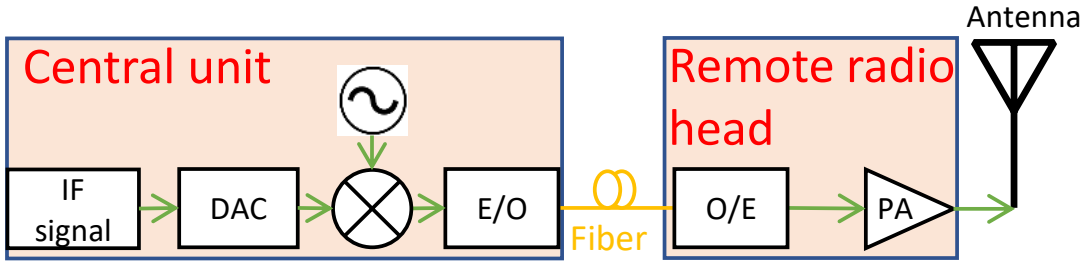

(b)

Figure 4.1: The mm-wave ARoF architecture illustrations. (a) The mm-wave signal generated in the remote radio unit; (b) The mm-wave signal generated in the central unit.

the mm-wave signal to a simplified RRH, which only encompasses O/E and PA functions. Since the RF signal is generated in the CU and the RRH does not convert frequencies, this architecture can allow phase-coherent RRHs to massive MIMO applications for high-capacity RAN infrastructure. However, it is important to note that the optical modulator/photodiode, in the E/O and O/E modules, has important limitations in terms of bandwidth, linearity, and noise for higher frequencies. In summary, Figure 4.1a features a simple fiber connection with a complex RRH, whereas the second architecture in Figure 4.1b has a complex fiber connection with a simple RRH.

Several mm-wave ARoF SISO experiments have been conducted [59]–[61]. The work presented in [60] aligns with the structure depicted in Figure 4.1b and involves the generation of quaternary-amplitude-shift-keying (4-ASK) modulated signals at 35.75 GHz at the CU. The study conducted in [59] shares the optical oscillation signal from the CU and produces an optical mm-wave signal at 28 GHz in the RRH. In the ARoF system described in [61], a mm-wave signal is transmitted from the CU, and a photodetector in the RRH is employed to recover the electrical mm-wave signal. A mm-wave ARoF demonstration in [62], with a cable-connected reference signal between RX and TX, operates at a 28.4 GHz carrier frequency using an outphasing principle. The results in [63] achieved the highest data rate of 328 Gbit/s with a single-user 2×2 C-MIMO antenna configuration. However, this system functions as two independent SISO systems based on narrow-beam horn antennas, but does not support MIMO precoding [63]. It is important to note that these experiments, while significant, are still in the early stages and face limitations in terms of using commercial components and coherent D-MIMO extension.

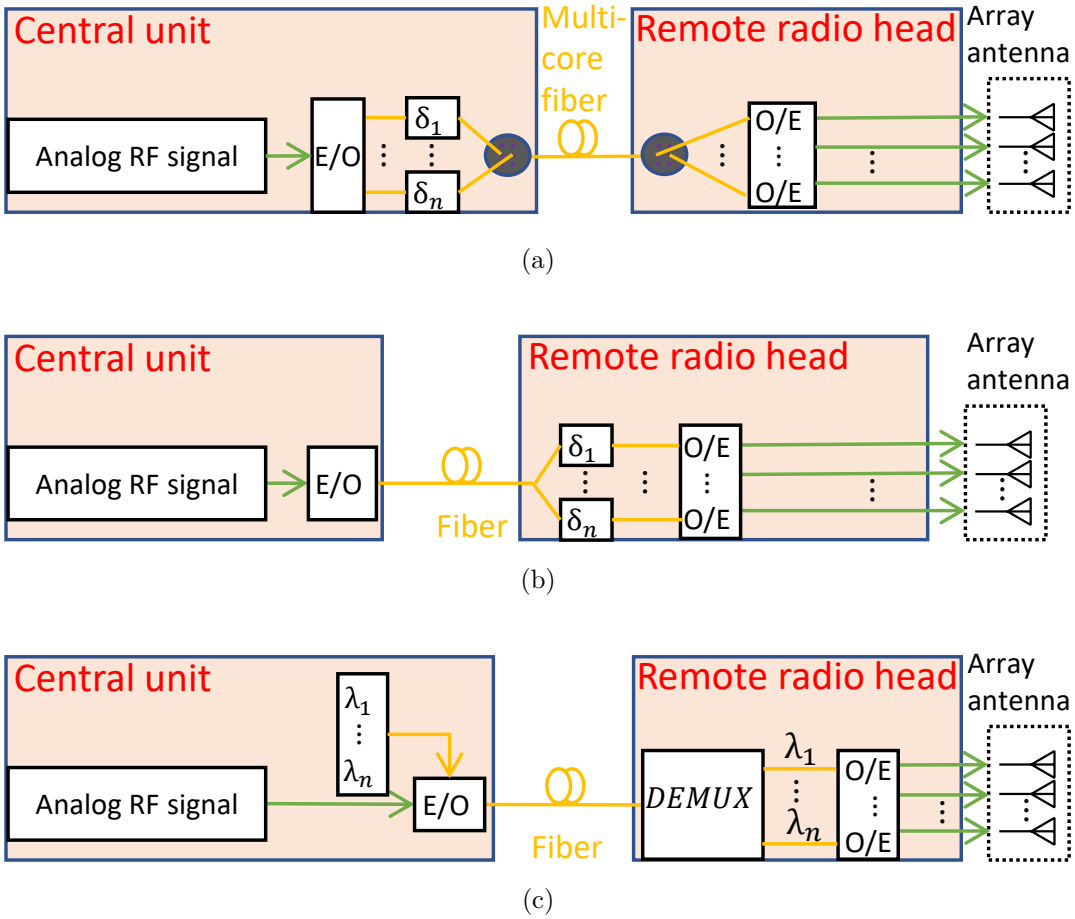

Figure 4.2: The mm-wave optical beamforming RoF architecture illustrations. (a) Hardware delay in the cental unit enabled optical beamforming architecture; (b) Hardware delay in the remote radio head enabled optical beamforming architecture; (c) Multiple wavelengths enabled Optical beamforming architecture; Demultiplexer (DEMUX).

4.1.2 Optical Beamforming

Another intriguing mm-wave RoF study focuses on the topic of optical beamforming based on the ARoF structure. Figure 4.2 provides an overview of the available mm-wave optical beamforming RoF structures, all of which generate mm-wave RF signals in the CU. The systems described in [64] and [65] follow the illustration in Figure 4.2a. In this setup, the CU delivers the optical modulated RF signal from E/O into several branches with different time delays δ_n. The fiber connection utilizes a multi-core fiber (MCF) to transmit optical signals, each with a distinct time delay δ_n. In the RRH, each branch of optical signals undergoes individual O/E conversion to recover RF signals with optical time delay δ_n for subsequent use in the phased array antenna. The time delay of the optical signal corresponds to the phase delay of electrical RF signals at the input of the phased array antenna. In the demonstration presented in [64], optical delay lines and attenuators are

employed to adjust the amplitude/phase of the seven optical signals, achieving optical beamforming functionality at 60 GHz with a 1.76 GHz bandwidth. The research conducted in [65] utilizes optical ring resonators for the optical signal time delay in the CU to achieve mm-wave beamforming functionality. The CU thermally adjusts the heaters to introduce different time delays for optical beamforming, successfully demonstrating a 3 GHz bandwidth for a 19 GHz RF signal.

In the second mm-wave optical beamforming RoF structure, a single-mode fiber (SMF) can serve as the connection between the CU and RRH, as depicted in Figure 4.2b. The CU transmits an optical RF signal to the SMF connection. The RRH receives the RF optical signal and repeats it for N branches with a time delay δ_n to each branch. Subsequently, O/E conversion and phased array antennas are employed. In the system outlined in [66], a switchable optical time delay circuit is implemented in the RRH, achieving mm-wave optical beamforming with a 2.2 GHz bandwidth (13.2 Gbit/s data rate) at a 28 GHz carrier frequency.

The final mm-wave optical beamforming RoF structure is introduced in the study [67], as illustrated in Figure 4.2c. The system in [67] allows the configuration of nine wavelengths for the optical modulator in the CU. In the RRH, each optical signal wavelength undergoes individual O/E conversion. The array antenna features nine distinct input ports, determining nine fixed beamforming directions. OTA measurements at 28.25 GHz carrier frequency are conducted using a 64-QAM OFDM signal with a 100 MHz bandwidth [67].

All three configurations depicted in Figure 4.2 require a Mach-Zehnder modulator (MZM) and an external laser to modulate RF signals into the optical domain, resulting in similar system complexities. However, the primary distinction arises from the fiber link. MCF is primarily suitable for short-distance connections due to modal dispersion. In contrast, a SMF solution necessitates a precise laser-fiber interface and can operate over several tens of kilometers.

4.1.3 Digital RoF

Figure 4.3 depicts digital RoF architectures designed for mm-wave systems. The initial architecture in Figure 4.3a is derived from the low-frequency structure and incorporates an upconversion function to produce an mm-wave signal in the RRH. The fiber link transmits CPRI or enhanced common public radio interface (eCPRI) data between the CU and the RRH. The DSP is compatible with fiber data protocols and supplies the high-speed DAC.

Subsequently, an SDoF solution employing real-time SDM is investigated, featuring a 100 Gbps bitrate for the demonstration of a carrier frequency range of 22.75 GHz to 27.5 GHz, achieving a symbol rate of 390 Msym/s performance [68]. As depicted in Figure 4.3b, the CU utilizes real-time four parallel SDM modules in FPGA at 25 Gbps, and the customized TX-circuit generates a single mm-wave RF SDM bit stream at 100 Gbps. However, the measurement results only showcase back-to-back fiber connection performance and do not include any OTA experiments. The SDM digital RoF architectures exhibit phase noise and a restricted symbol rate in the real implementations. Moreover, certain SDoF experimental works

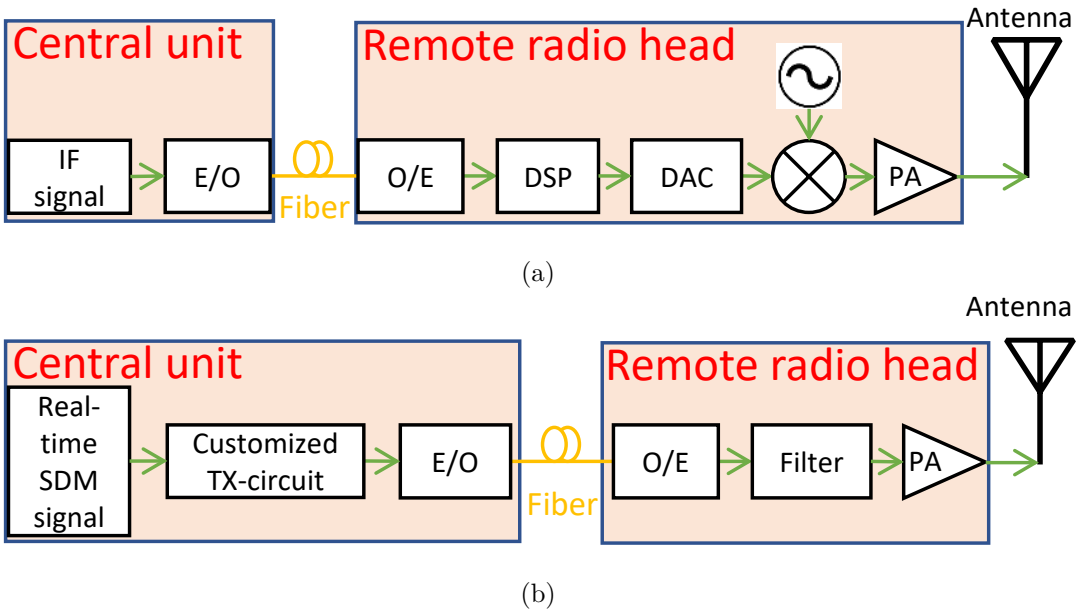

Figure 4.3: The mm-wave DRoF architecture illustrations. (a) CPRI or eCPRI based; (b) SDM based.

have demonstrated functionality at sub-terahertz frequencies of 370/320 GHz with bandwidths of 2/4.6 GHz [69] [70].

4.2 mm-wave SDoF MIMO Link Architecture

This section introduces novel low-complex mm-wave SDoF MIMO architectures with IF SDoF and baseband SDoF variations.

4.2.1 IF SDoF

In Paper [C], an innovative mm-wave IF SDoF MIMO link architecture was introduced, utilizing a quad small form-factor pluggable 28 (QSFP28) fiber connection, as depicted in Figure 4.4. The QSFP28, being a standardized and readily available module, offers four independent subchannels with a 25 Gbps data rate each. The architecture leverages SDM-coded IF with a remote LO for upconversion. The CU generates four coherent BPSDM bit streams offline from four IF digital signals. The FPGA board interfaces with the personal computer (PC) and transmits the four electrical bit streams to the QSFP28 fiber connection. The RRH comprises a QSFP28 transceiver, 90° hybrids, upconverters, and oscillation signals. The 90° hybrids connect with the QSFP28 outputs to obtain quadrature IF signals for the single sideband upconverters. While, in theory, SDM signals would require a BPF for analog IF signal recovery [71], in this implementation, the 90° hybrids and the input of the upconverter serve as effective BPFs. The RRH provides four independent inputs to an array antenna,

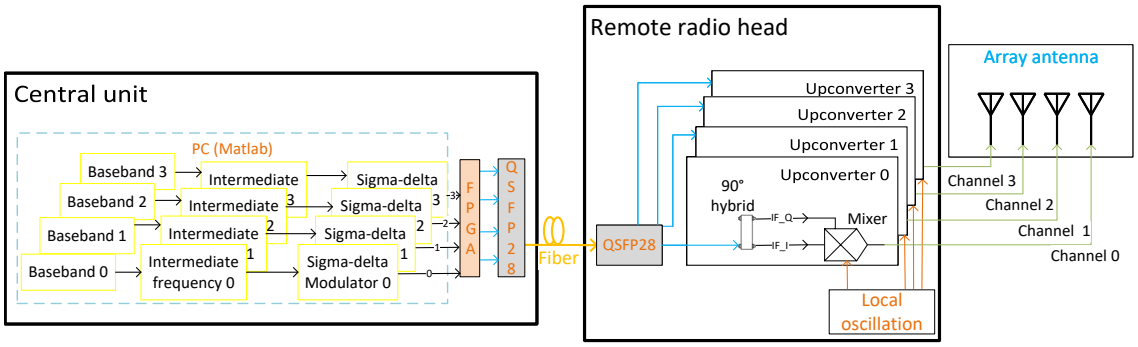

Figure 4.4: Proposed mm-wave IF SDoF architecture [C].

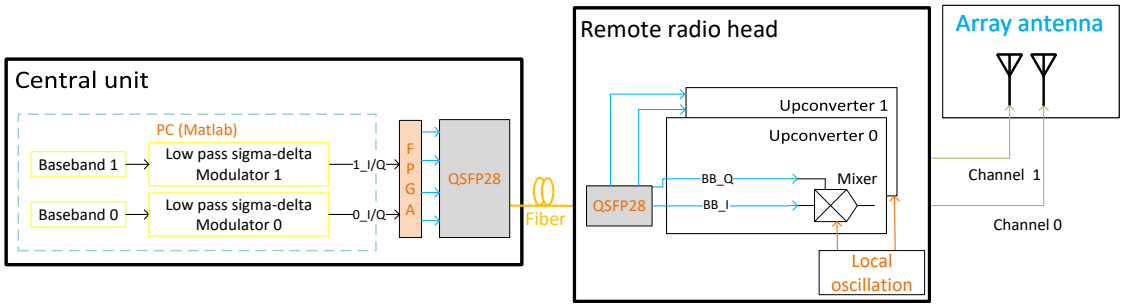

Figure 4.5: Proposed mm-wave baseband SDoF architecture [E].

enabling the CU to exercise remote and full digital control over the four-channel signals in this mm-wave MIMO link architecture.

4.2.2 Baseband SDoF

The architecture based on the QSFP28 fiber connection can also operate with a baseband SDM principle, as depicted in Figure 4.5. The parallel lowpass sigma-delta modulators (LPSDMs) modulates the I/Q branch of the baseband signal into a pair of bitstreams. The QSFP28 fiber connection then transmits four bitstreams (representing two baseband SDM signals) to the RRH. The remote LO and mixer facilitate the upconversion of the baseband SDM bitstreams into an mm-wave signal, which is subsequently connected to the inputs of an array antenna.

4.2.3 Comparison

Figure 4.6 illustrates the theoretically simulated NMSE results for the proposed mm-wave IF SDoF and baseband SDoF links, using a single carrier 64-QAM signal at 25 Gbps. The mm-wave IF SDoF link using BPSDM achieves -23.3 dB NMSE at 1200 Msym/s. In comparison, the baseband SDM for the baseband SDoF link achieves a higher NMSE of -38.9 dB at the same symbol rate. It is important to note that the baseband SDoF architecture supports only two baseband signals per QSFP28 fiber connection, while the IF SDoF architecture can transmit four IF

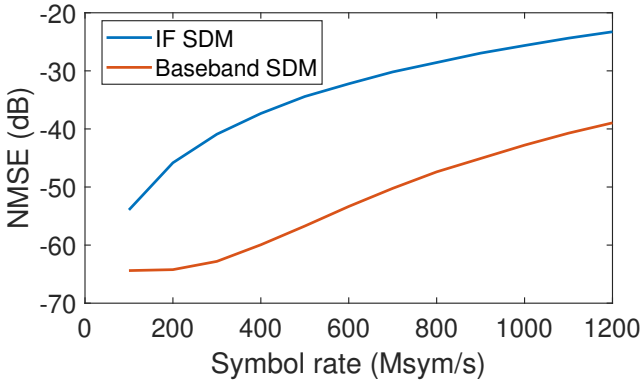

Figure 4.6: The IF SDM and baseband SDM simulation results for two corresponding proposed architectures in Figure 4.4 and Figure 4.5.

signals. The IF SDoF architecture employs hybrids for single-sideband upconversion, while the baseband SDoF architecture does not require this component. Additionally, the IF SDoF architecture offers more flexibility in choosing the carrier frequency by adjusting the IF or LO frequency, whereas the carrier frequency in the baseband SDoF architecture is solely determined by the LO frequency.

4.3 mm-wave IF SDoF MIMO Link Demonstrator

The previously introduced mm-wave IF SDoF structure is implemented using readily available components and validated in this section.

4.3.1 IF SDoF MIMO Link Implementation

The proposed architecture has been implemented and validated in Paper [D], as depicted in Figure 4.7. In the CU, the IF frequency is set at 2.2 GHz, corresponding to the center frequency of the chosen 90° hybrid. The oscillation frequency from the signal synthesizer is 6.45 GHz, with a built-in LO quadrupler in the mixer, allowing the RF frequency to be 28 GHz, calculated as $6.45\ \text{GHz} \times 4 + 2.2\ \text{GHz} = 28\ \text{GHz}$. This architecture can generate RF frequencies up to 44 GHz by adjusting either the oscillation frequency or the IF frequency. The mm-wave signals from the RRH are fed into a linear array antenna with four independent inputs. Further details on the principle can be found in Paper [D].

On the RX side, Vivaldi antennas are employed and linked to a low noise amplifier (LNA) along with a Keysight VSA (N9042B UXA X-Series Signal Analyzer [72]). The VSA is capable of inspecting the signal spectrum, measuring power levels, and facilitating downconversion for RX signal processing.

4.3.2 Hardware

All commercially available hardware utilized in the TX implementation is detailed in Table 4.1. The 90° hybrid (ZX10Q-2-27-S+) accommodates frequencies ranging

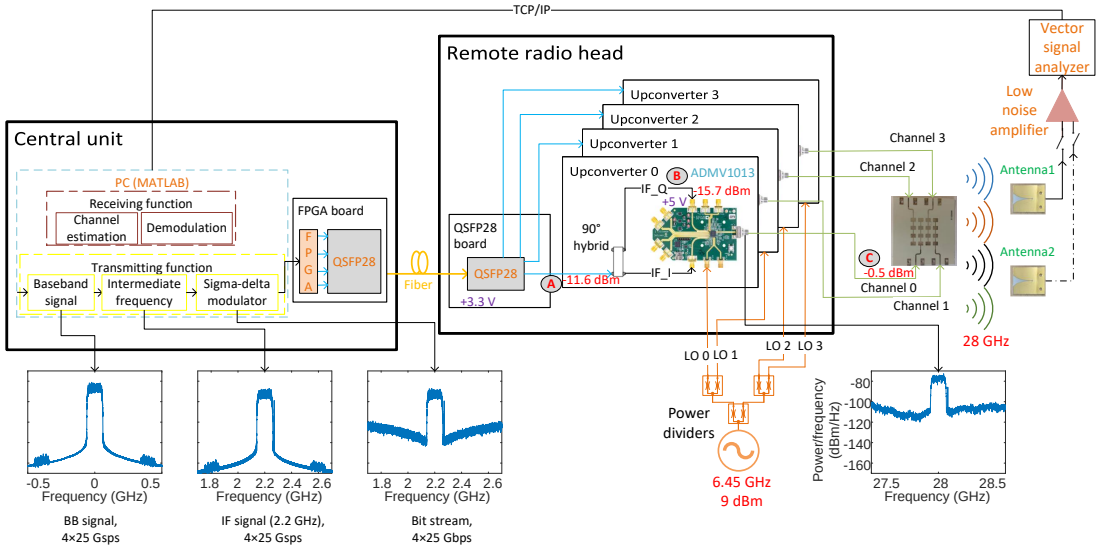

Figure 4.7: Proposed mm-wave IF SDoF link implementation with spectrum and power levels [D].

Table 4.1: Commercial hardware list of the IF SDoF transmitter [D].

Hardware	Manufacturer	Model	Quantity	Ref.
FPGA board	Xilinx	VCU128	1	[73]
QSFP28	FS	QSFP28-SR4-100G	2	[74]
90° Hybrid	Mini-Circuits	ZX10Q-2-27-S+	4	[75]
Power divider	Mini-Circuits	ZX10R-14-S+	3	[76]
Mixer	Analog Devices	EVAL-ADMV1013	4	[77]

Table 4.2: Technical specifications of the QSFP28 module used [D].

Specification	Description	Specification	Description
Wavelength	850 nm	Connector	MTO[a]-12
Media	Multi-mode fiber	Max fiber length	100 m
TX Type	VCSEL[b]	Receiver Type	PIN[c]diode
TX Power	-8.4 to 2.4 dBm	Max Data Rate	4x25.78 Gbps

[a] Multifiber Termination Push-on/Pull-off.
[b] Vertical Cavity Surface Emitting Laser.
[c] P-doped - Intrinsic - N-doped.

from 1.7 GHz to 2.7 GHz. The power dividers (ZX10R-14-S+) are operational up to 10 GHz and distribute the LO signal among four upconverters. The upconverting mixers (EVAL-ADMV1013) function as upconverters, generating frequencies up to 44 GHz in both IF and baseband input signal modes.

For the fiber connection, the technical specifications associated with the QSFP28 module are outlined in Table 4.2. A more in-depth description is provided in Paper [D].

The TX antenna array comprises a total of 16 patch elements. Each column is composed of four fixed patch elements, resulting in a narrow elevation beam width. The TX antenna allows for the steering of the transmitted beam in the azimuth direction through the control of phase inputs. Further details about the antenna can be found in Paper [D].

4.3.3 Signal Processing

During the following OTA measurements, we account for the total phase differences of the system by channel estimation and compensate for the phase differences by precoding. The MIMO link works in TDD mode in paper [C] and paper [D].

There are two steps for MISO or MIMO demonstration, and channel estimation is the first step. The orthogonal pilot signal $\mathbf{X}_\mathrm{p}$ is

$$\mathbf{X}_\mathrm{p} = \begin{bmatrix} \mathbf{x}_0 & \mathbf{0} & \mathbf{0} & \mathbf{0} \\ \mathbf{0} & \mathbf{x}_1 & \mathbf{0} & \mathbf{0} \\ \mathbf{0} & \mathbf{0} & \mathbf{x}_2 & \mathbf{0} \\ \mathbf{0} & \mathbf{0} & \mathbf{0} & \mathbf{x}_3 \end{bmatrix}_{N\times 4}, \tag{4.1}$$

where the $\mathbf{x}_0$, $\mathbf{x}_1$, $\mathbf{x}_2$, $\mathbf{x}_3$ and $\mathbf{0}$ have $N/4$ samples. Moreover, the LS algorithm calculates the channel information $\widehat{\mathbf{H}}$ according to equation (2.17). The second step is the ZF MIMO precoding of user data, as explained in subsection 2.3.3. The MISO digital beamforming follows the precoding of subsection 2.2.2.

4.4 mm-wave IF SDoF Wireless Communication Experiments

In this section, the previously implemented mm-wave IF SDoF MIMO link is utilized to demonstrate wireless communication through digital beamforming MISO and MIMO experiments.

4.4.1 Prerequisites

Paper [D] investigates the proposed IF SDoF architecture extensively for MIMO applications. The link characterization is conducted using the setup depicted in Figure 4.8, operating at a center frequency of 28 GHz. All link characterizations involve a single-carrier 64-QAM signal. The study in Paper [D] also examines the

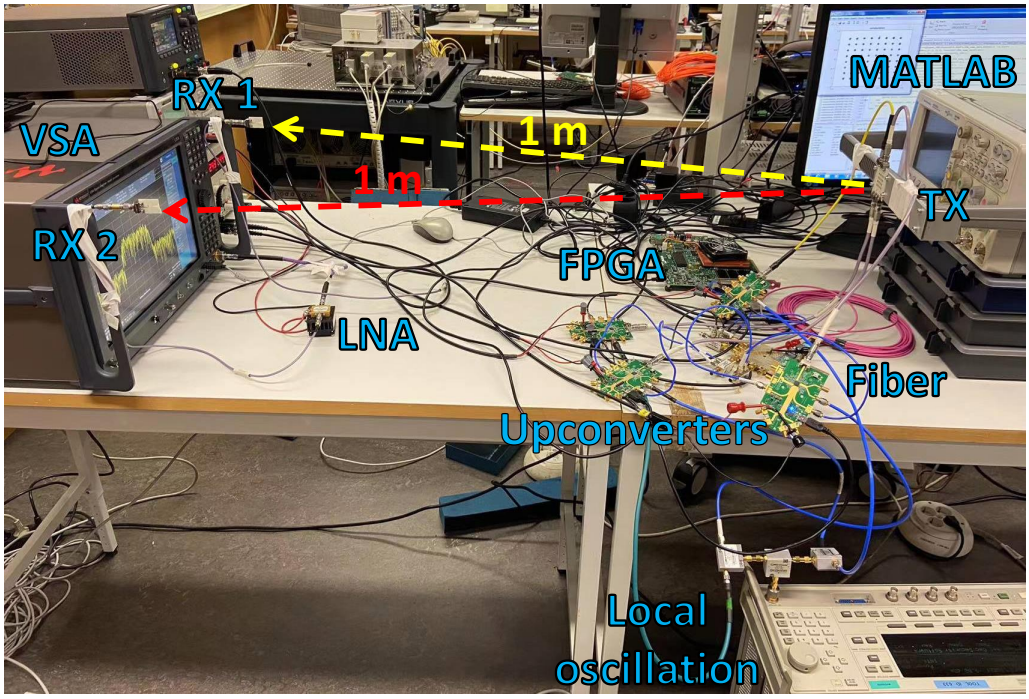

Figure 4.8: The experimental setup used to demonstrate the proposed IF SDoF link implementation. The transmitting linear array antenna is placed at a 1 m distance from the two receiving antennas. The two receiving antennas are separated by 0.5 m [D].

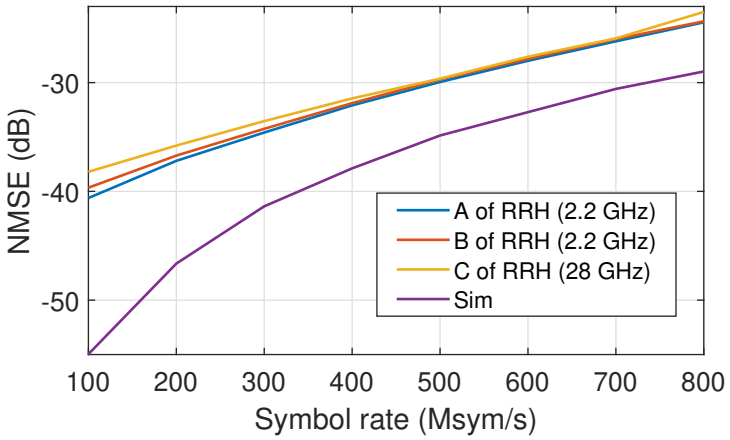

Figure 4.9: Bandwidth performance analysis of the IF SDoF implementation. The NMSE for an ideal SDM is included as a reference (Sim). The NMSE results are measured at the positions A, B, and C indicated in Figure 4.7 [D].

signal spectra at various stages, assessing parameters such as inband power and adjacent channel power ratio (ACPR).

The symbol rate verification is constrained to a maximum of 800 Msym/s due to the bandwidth of the hybrid, as shown in Figure 4.9. The simulated SDM signal performance, labeled as Sim in the bottom curve of Figure 4.9, serves as a reference for the measured results. The positions A, B, and C correspond to the labeled measurement test points inside the transmitter, as indicated in locations in Figure 4.7. Position B exhibits inferior performance compared to position A due to power differences. The limitation in performance at position C stems from the noise figure of the upconverter and the noise floor of the VSA. Despite the measured results being generally 5 dB lower than the simulated ones at 800 Msym/s, this discrepancy is deemed reasonable for hardware performance, consistent with the findings in [28]. Overall, the measured results align with the simulated trend.

4.4.2 Beamforming MISO

The OTA demonstration encompasses SISO, MISO, and MIMO scenarios, conducted over a distance of 1 meter between the RX and TX antennas. These demonstrations are presented in the subsequent subsections.

As outlined in Section 3.3, the digital beamforming demonstration involves two key steps: channel estimation and MISO beamforming. During the channel estimation step, the TX emits pilot signals, and the RX computes the channel information. The measured channel results, discussed intensively in Paper [D], confirm the anticipated stable amplitude and phase information, validating the stability and accuracy of the channel information in this MISO demonstration.

In Figure 4.10, the MISO OTA received bandpower is 3.2 dBm, while the SISO OTA case shows a received bandpower of -8.1 dBm. This indicates that digital beamforming results in an additional 11.3 dB of bandpower, aligning closely with the theoretical expectation of a 12 dB beamforming gain for a system with four antenna elements.

Figure 4.11 presents results for back-to-back, SISO OTA, MISO OTA, and simulated NMSE for symbol rates up to 700 Msym/s. The highest path loss in the SISO OTA scenario, shown at the top, is due to the 1 m distance at 28 GHz. With all TX sub-channels active, digital beamforming enhances the NMSE to -25.2 dB, a value closely resembling the NMSE at the upconverter output port (position C in Figure 4.7).

In conclusion, this proposed mm-wave IF SDoF architecture demonstrated a digital beamforming function that improves the received power and NMSE performance with precise channel information.

4.4.3 MU-MIMO

The following demonstration assesses the proposed architecture in a practical MU-MIMO scenario. This demonstration involves two steps: channel estimation and ZF MIMO communication. Due to the limitation of having only one LNA and one VSA,

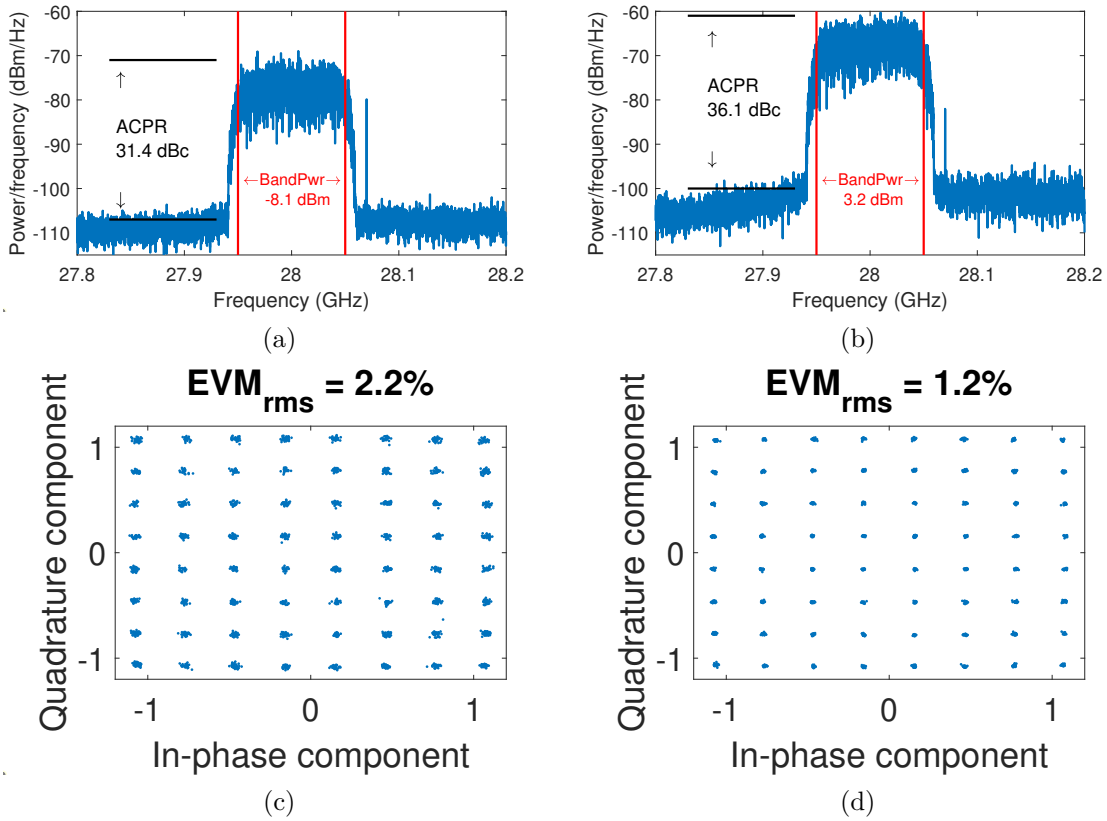

Figure 4.10: The received OTA signal performance in [D] of (a) SISO OTA; (b) MISO OTA; (c) SISO constellation with the error vector magnitude (EVM); (d) MISO constellation with the EVM.

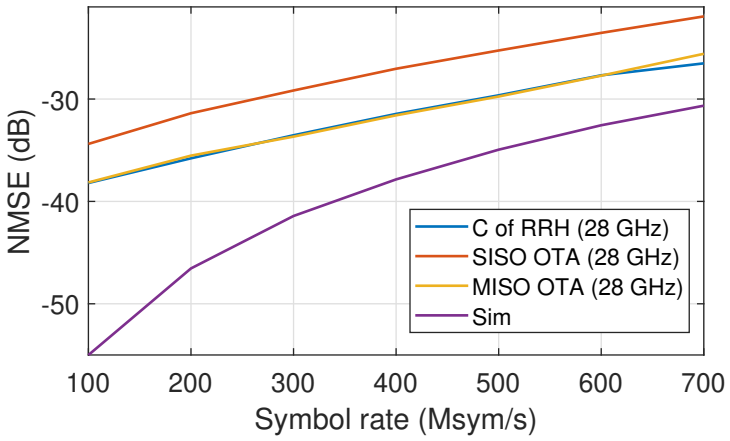

Figure 4.11: Symbol rate performance of digital beamforming demonstration of the IF SDoF link implementation. The NMSE results are measured at the position C indicated in Figure 4.7, SISO and MISO OTA transmissions [D].

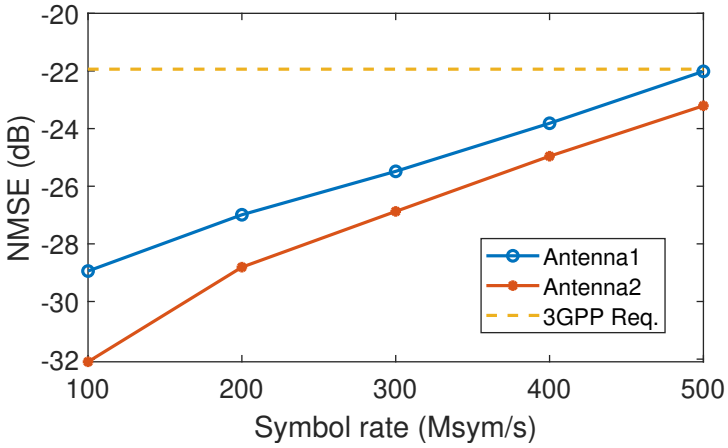

Figure 4.12: Symbol rate performance of MU-MIMO demonstration with the proposed IF SDoF link implementation [D].

channel information is gathered sequentially by switching cables between antennas 1 and 2. The measured channel stability aligns with the results obtained from the digital beamforming scenario, indicating the stability of the system.

Throughout the experiments, the symbol rate was systematically adjusted from 100 Msym/s to 500 Msym/s by iteratively executing the channel estimation and ZF MIMO communication steps. Figure 4.12 displays the NMSE outcomes for two users alongside the 3rd generation partnership (3GPP) requirements. At 500 Msym/s, both users exhibit NMSE values of -22.1 dB and -23.3 dB, respectively, meeting the 3GPP specifications for 64-QAM modulation [78]. Notably, Antenna 2 consistently outperforms Antenna 1 based on NMSE results. Importantly, even with changes in cable switching order, the outcomes remain consistent, affirming that cable switching does not impact MIMO demonstration. It is worth acknowledging that variations in the position and radiation patterns of RX/TX antennas may contribute to differences in the effective received signal power [79].

4.5 mm-wave Baseband SDoF Transmitter with Experiments

The previous section illustrates the proposed mm-wave IF SDoF architecture with implementation and measurement results. The proposed mm-wave baseband SDoF structure from section 4.2.2 is demonstrated with off-the-shelf components and measured in this section.

4.5.1 Baseband SDoF Link Implementation

Figure 4.13 shows the block diagram of the implementation of the proposed baseband SDoF TX has been documented in Paper [E]. In the CU, the baseband signal undergoes shaping, filtering, and upsampling to 25 Gsps before entering the second-order LPSDM. The FPGA within the CU then transmits the LPSDM signal to the

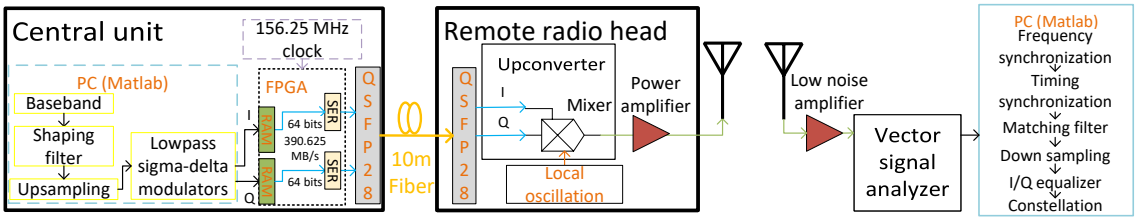

Figure 4.13: Proposed millimeter-wave baseband SDoF demonstrator [E].

Table 4.3: Hardware list of the mm-wave baseband SDoF demonstrator.

Hardware	Manufacturer	Model	Quantity	Ref.
FPGA board	Xilinx	VCU128	1	[73]
QSFP28	FS	QSFP28-SR4-100G	2	[74]
Mixer	Analog Devices	EVAL-ADMV1013	1	[77]
Power amplifier	Analog Devices	EVAL-HMC943APM5E	1	[80]

RRH. Within the RRH, a baseband mode upconversion mixer interfaces with the LPSDM signal and a 7 GHz signal synthesizer. The 7 GHz LO signal with a built-in quadrupler in the mixer achieves a RF frequency of 28 GHz. This configuration allows the architecture to emit RF frequencies up to 44 GHz by adjusting the oscillation frequency. The mm-wave signals from the RRH are conveyed to an antenna after a PA stage. The RRH features a Vivaldi antenna tailored for a center frequency of 28 GHz. In the demonstration, an identical antenna is employed at the RX. The RX incorporates a LNA preceding a 33 GHz oscilloscope (UXR0334A Infiniium UXR-Series, 128 GS/s) equipped with a VSA software. RX signal processing encompasses frequency and timing synchronization, matching filtering, down-sampling, and I/Q equalizer stages, to get a demodulated constellation.

All commercially available components employed for the baseband SDoF TX implementation are detailed in Table 4.3. Notably, the FPGA board, QSFP28 module, and mixer remain consistent with the earlier IF SDoF implementation. A PA of EVAL-HMC943APM5E has been added to facilitate higher output power, reaching an ideal 29 dBm at the 1 dB compression point. The technical specifications of the QSFP28 module align with those previously documented in Table 4.2. The cable utilized comprises twelve fibers, with two dedicated to transmitting I/Q bit streams in the presented demonstration.

4.5.2 Transmitter Verification

The implemented baseband SDoF TX is validated through measurements in a setup depicted in Figure 4.14. The verification results include power level assessment, ACPR, signal spectrum analysis, and bandwidth performance at various stages, as detailed in Paper [E].

In the evaluation of symbol rate performance at different stages of RRH, the results are compared with simulations, as depicted in Figure 4.15. In general, the quality of the output signal of the QSFP28 module, as measured by its error

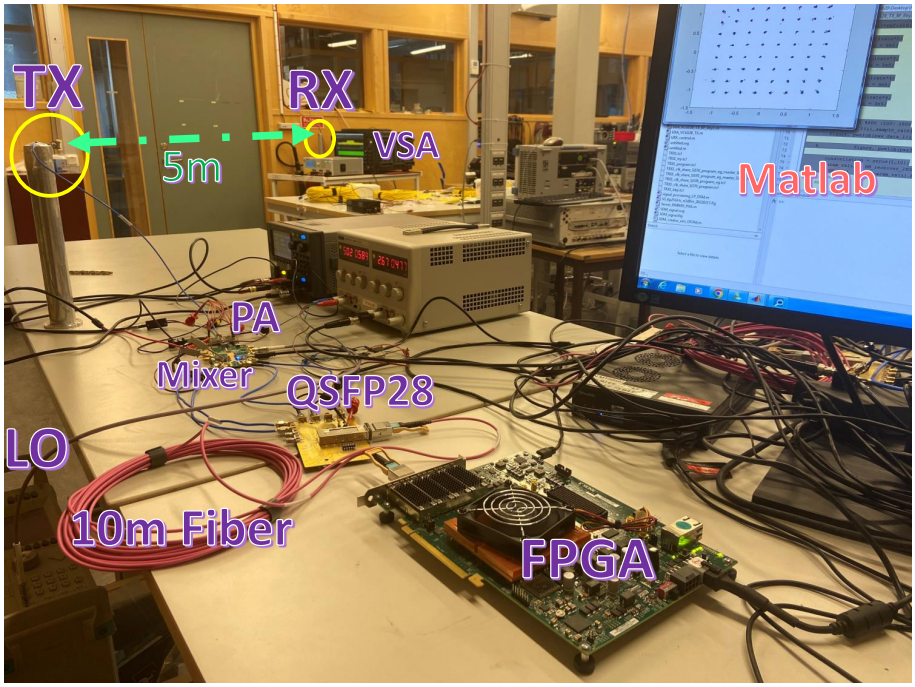

Figure 4.14: Measurement setup of mm-wave baseband SDoF demonstrator. The transmitting antenna has a 5 m OTA distance from the receiving antenna [E].

vector magnitude (EVM), closely mirrors its performance post-upconversion in the mixer, albeit with a slight degradation due to the tradeoff between output power and nonlinearity, as discussed in Paper [E]. At a symbol rate of 1.5 Gsym/s, all measured results closely align with the theoretical limits imposed by the quantization noise determined by the sample rate of LPSDM. This observation suggests that the dominant factor influencing TX performance is the quantization distortion intrinsic to the SDM signal, for large bandwidths.

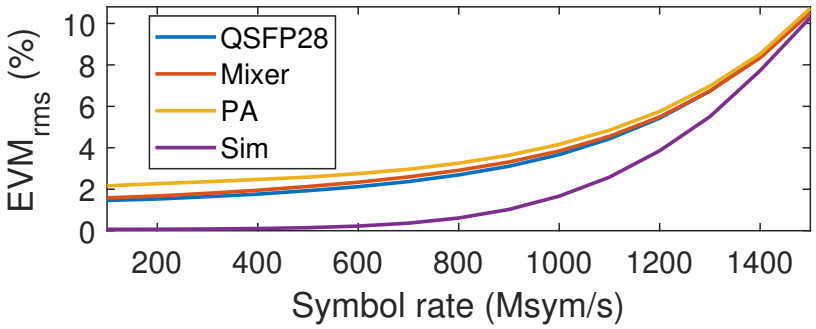

Figure 4.15: mm-wave baseband SDoF transmitter output signal performance quantified by EVM for 64-QAM up to 1.5 Gsym/s [E].

4.5.3 Over-The-Air Performance

Throughout the OTA experiments, a 5 m separation is maintained between the TX and RX antennas, as depicted in Figure 4.14. These OTA experiments encompass

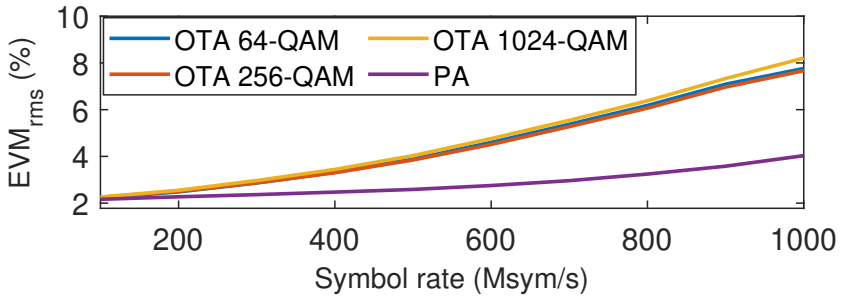

Figure 4.16: mm-wave baseband SDoF OTA demonstration and back-to-back (PA) measurements with the EVM results [E].

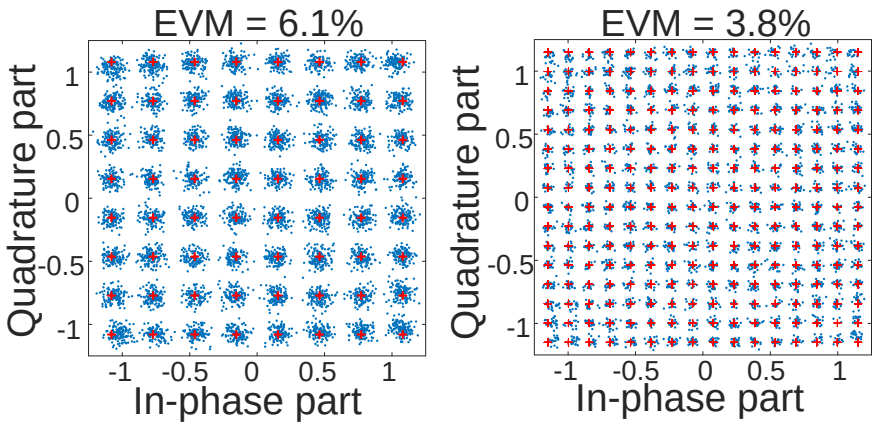

Figure 4.17: Zero-error constellations for 64/256-QAM from the mm-wave baseband SDoF OTA demonstration [E].

three distinct modulation scenarios, including 64-QAM, 256-QAM, and 1024-QAM. As revealed by the outcomes illustrated in Figure 4.16, the EVM remains consistent regardless of the chosen modulation scheme, resulting in an EVM of approximately 8% at a symbol rate of 1 Gsym/s. It is noteworthy that the differences observed between the OTA performance curves and the results obtained directly at the output of the PA are primarily attributed to the reduction in the received signal power spectral density in proportion to the increasing bandwidth. This phenomenon can potentially be mitigated by reducing the separation distance, enhancing the output power, or employing antennas with more directive characteristics.

Evaluating bit-error rates (BER) without the use of forward error correction is a stricter requirement than EVM. In this context, we determined the zero-error symbol rates for 64-QAM, 256-QAM, and 1024-QAM signals, which are 800 Msym/s, 500 Msym/s, and 200 Msym/s, respectively. These rates were obtained through ten transmission trials involving 46,080 bits, 38,400 bits, and 19,200 bits, corresponding to the three modulation schemes. Figure 4.17 displays the associated demodulated constellations for 64-QAM and 256-QAM signals at symbol rates of 800 Msym/s and 500 Msym/s, respectively, which exhibit EVM values of 6.1% and 3.8%. These rates translate to data rates of 4.8 Gbps and 4 Gbps, respectively. In general, it is observed that lower modulation formats result in higher data rates, whereas higher modulation formats offer the promise of greater spectrum efficiency.

4.6 Chapter Conclusion

This chapter introduces an innovative, flexible mm-wave SDoF architecture (Paper [C]) that supports IF (Paper [D]) and baseband (Paper [E]) demonstrations. For both implementations, a step-by-step power study and bandwidth verification validated the potential of the mm-wave TXs through measurements. Furthermore, OTA experiments confirmed that the proposed demonstrations have high capacity at SDoF wireless communication.

Table 4.4 compares this demonstration with state-of-the-art RoF publications, encompassing both ARoF and SDoF architectures for the mm-wave band. From the table, it is concluded that the IF SDoF demonstration serves two users with a symbol rate of 500 Msym/s, and the baseband SDoF demonstration reaches 1 Gsym/s. Both of these have the highest data rates in the SDoF category. This architecture can also serve as a foundational element for D-MIMO technology with IF and baseband versions.

Table 4.4: Comparison with state-of-the-art RoF publications.

Ref.	**RoF**	**MIMO**	**Symbol rate**	**OTA**	**Carrier**	**NMSE**
[59]	ARoF	1×1	1.96 Gsym/s	2.2 m	28 GHz	-14 dB[a]
[67]	ARoF	9×1	100 Msym/s	6.3 m	28 GHz	-31.3 dB
[63]	ARoF	2×2[b]	22 Gsym/s	0.2 m	140 GHz	-14 dB[a]
[64]	ARoF	8×1	3.5 Gsym/s	0.5 m	60 GHz	-19.6 dB
Paper [D]	IF SDoF	4×1	700 Msym/s	1.0 m	28 GHz	-25.2 dB
Paper [D]	IF SDoF	4×2	500 Msym/s	1.0 m	28 GHz	-22 dB
Paper [E]	Baseband SDoF	1×1	1 Gsym/s	5.0 m	28 GHz	-22 dB

[a] The paper reports the bit-error rate (BER) corresponding to forward error correction (FEC) with 25% overhead. The NMSE requirement for this BER is -14 dB [81].
[b] This is only antenna configuration and does not have MIMO precoding.

Chapter 5

mm-wave RoF D-MIMO Systems

The advancement of D-MIMO technology holds the potential to enhance capacity and coverage for mm-wave RoF wireless communication. Nonetheless, the implementation of mm-wave RoF D-MIMO systems encounters challenges related to coherence and complexity, particularly arising from the nature of distributed RRHs. As a result, only a subset of the mm-wave RoF architectures outlined in Chapter 4 have been extended for D-MIMO, and these developments will be presented in this chapter. Additionally, this chapter will feature the illustration of two competitive mm-wave SDoF D-MIMO solutions, complementing the aforementioned expanded architectures. The conclusion section will have a comparison of state-of-the-art mm-wave RoF D-MIMO demonstration results.

5.1 State-of-the-Art mm-wave RoF D-MIMO Publications

Several mm-wave state-of-the-art D-MIMO systems, either ARoF- or SDoF-based, are currently available and will be thoroughly discussed in this section.

5.1.1 Analog RoF

In the study [82], analog IF signals and synchronization clocks are transmitted from a central unit to RRHs, facilitating a coherent upconversion stage across eight distributed RRHs, as illustrated in Figure 5.1a. This proposed system operates with an 800 MHz bandwidth at a frequency of 28 GHz. Subsequently, the D-MIMO system is deployed to provide mm-wave 5G services both indoors and outdoors. For indoor demonstrations, four distributed RRHs with 2 km fiber connections achieve a total throughput of 4 Gb/s for a single terminal [83]. Outdoor demonstrations involve connecting the central unit to two distributed RRHs using two 1 km fibers in an urban setting, each RRH equipped with four mm-wave TXs [84]. The mm-wave UL/DL outdoor demonstration data rates are reported as 1 Gb/s and 9 Gb/s, respectively, operating in TDD mode. Furthermore, the system has been evolved

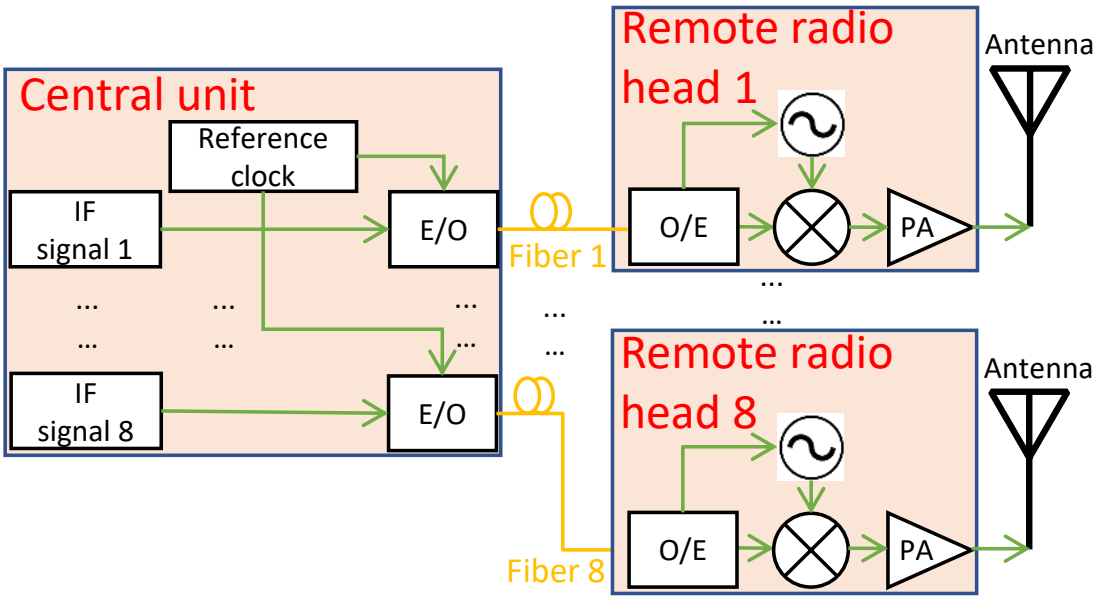

(a)

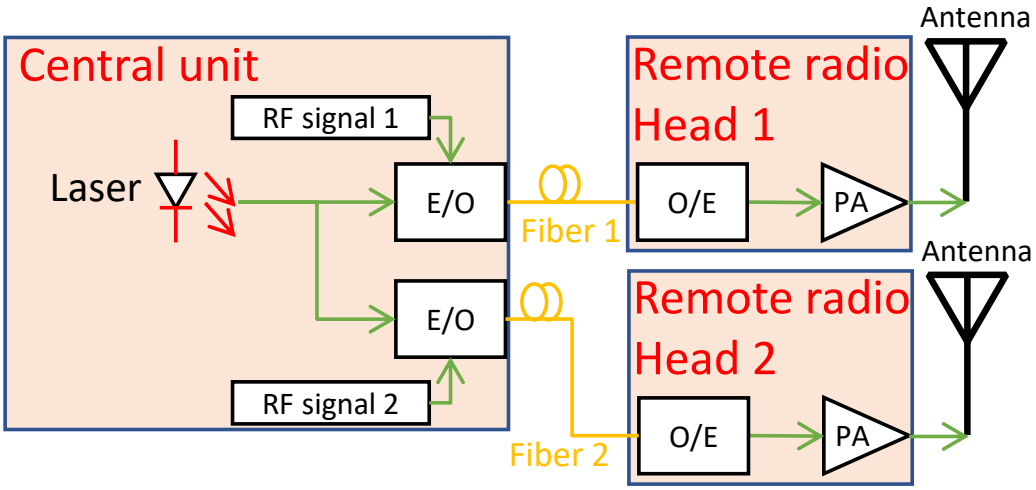

(b)

Figure 5.1: State-of-the-art mm-wave analog-radio-over-fiber based D-MIMO architectures. (a) The mm-wave signal is generated in the remote radio unit [82]; (b) The mm-wave signal is generated in the central unit [86].

into a cascaded RRHs version with a single fiber connection, further expanding communication coverage [85].

Conversely, another mm-wave ARoF D-MIMO system is introduced in [86], depicted in Figure 5.1b. In this architecture, mm-wave RF signals are generated in the central unit for optical transmission, with the RRH requiring only O/E conversion and PA stages. The mm-wave D-MIMO system relies on an innovative mm-wave RF O/E transceiver design [87] and an air-filled antenna array[88], operating in the mm-wave 5G bands (24.25 – 29.5 GHz). This system achieves a throughput of 48 Gb/s in harsh indoor conditions, demonstrating the capabilities of D-MIMO technology. Additionally, the study addresses self-blocking and other non-line-of-sight

challenges in the mm-wave band, with a focus on applications in the context of Industry 4.0 [89].

5.1.2 Sigma-Delta-over-Fiber

The mm-wave D-MIMO system reported in Figure 5.2 adopts a SDoF architecture, as proposed in [90]. This system transmits IF SDM signals to the RRHs and employs a BPF to suppress out-of-band SDM quantization noise. The RRH includes a mm-wave upconverter to generate a desired mm-wave RF signal. The architecture enables D-MIMO operation, incorporating coherent LO signals derived from clock data recovery (CDR) circuit and a phase-locked loop (PLL). A bandwidth of 160.32 MHz is demonstrated for a 2×1 MISO configuration. It is noteworthy that this bandwidth is constrained by the 10 Gbps data rate of the fiber connection and the phase noise inherent in the employed PLL, as discussed in [90].

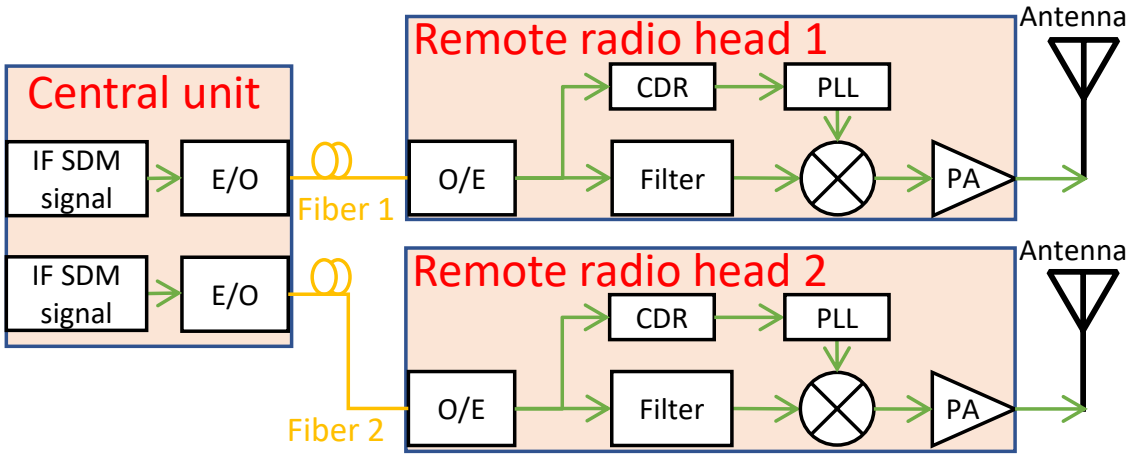

Figure 5.2: State-of-the-art mm-wave sigma-delta-over-fiber based architecture [90].

5.2 mm-wave IF SDoF D-MIMO OFDM Demonstrator

This section explains the proposed IF SDoF D-MIMO OFDM demonstrator with corresponding implementation and verification measurements.

5.2.1 Demonstrator Implementation

In this setup, a CU and two RRHs are employed, as depicted in Figure 5.3. The CU consists of a PC and an FPGA board. For this demonstration, the signal is modulated using OFDM 64-QAM and generated in MATLAB. The SDM is performed in MATLAB using the appropriate toolbox [91]. The specific offline signal processing details conducted on the PC are provided in Paper [F]. The FPGA board plays

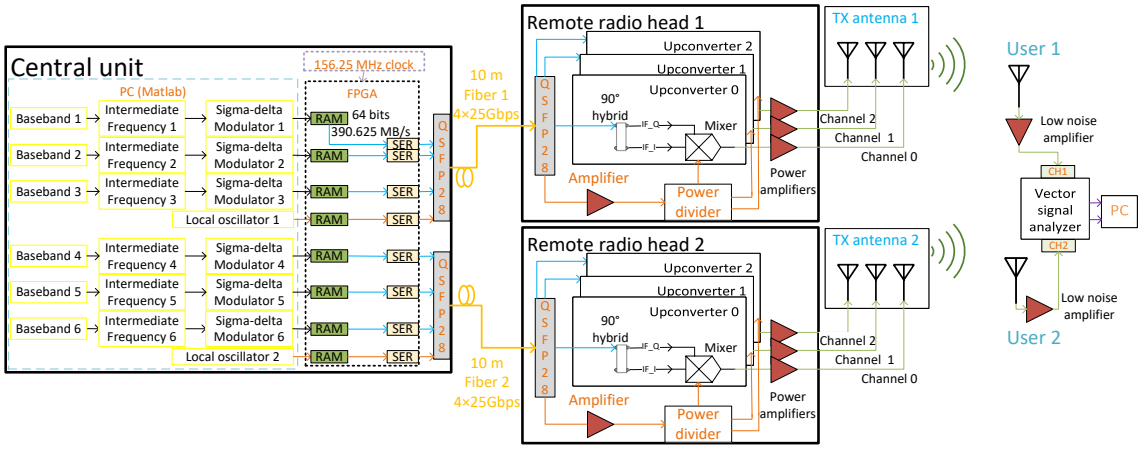

Figure 5.3: Proposed mm-wave IF SDoF D-MIMO architecture [F].

a crucial role in transmitting the IF SDM bitstreams to the RRHs via high-speed QSFP28-fiber optical fronthaul links.

The fiber connections utilized are given by the specifications outlined in Section 4.3, and the technical specifications of the QSFP28 modules are consistent with those presented in Table 4.2. Each QSFP28 link provides four parallel high-speed digital channels, each operating at a rate of 25 Gbps. Among these channels, three are dedicated to transmitting IF SDM bitstreams, while the remaining channel transmits periodic sequences of zeros and ones, serving as LO signals for the upconverters in the RRH. The FPGA board plays a crucial role in maintaining coherence among the distributed fiber links by synchronizing all signals to a shared onboard oscillator. As a result, the proposed D-MIMO TX architecture achieves synchronization among the RRHs under the control of the CU.

Detailed descriptions of the RRH and the TX antenna can be found in Paper [F]. In general, each RRH is equipped with LO amplifiers and power dividers, ensuring coherence within the system and providing sufficient power to drive the upconversion mixers. The generated LO frequency is 6.25 GHz. Each RRH unit is composed of three parallel upconversion mixers, three 90° hybrids, and three mm-wave PAs. In this particular application, the 90° hybrid, along with the mixer's IF input impedance, functions as a BPF, effectively suppressing the majority of out-of-band quantization noise. Additionally, the 90° hybrids play a crucial role in facilitating single sideband upconversion by providing a quadrature IF signal to the mixers.

In this implemented setup, the combination of a 1.5 GHz IF signal with the 6.25 GHz LO frequency results in an upper sideband output frequency of 26.5 GHz, as expressed by the formula $6.25\ \text{GHz} \times 4 + 1.5\ \text{GHz} = 26.5\ \text{GHz}$. It enables a flexible output frequency by altering the IF frequency or fiber link data rate. The linear patch antenna array used in the TX operates at 26.5 GHz. Each TX antenna features four independent feeding ports, with three of them being supplied with the three parallel coherent signals from the RRH. This configuration enables the antenna to perform a CU-controlled digital beam steering function in the azimuth direction.

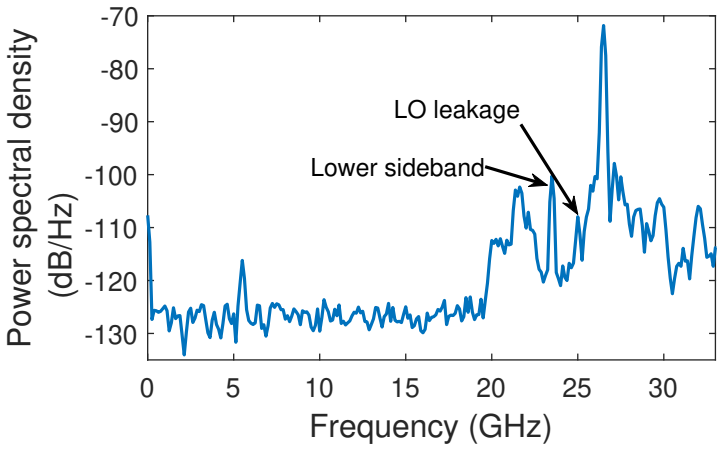

Figure 5.4: Wideband spectrum at the output for one channel of the RRH [F].

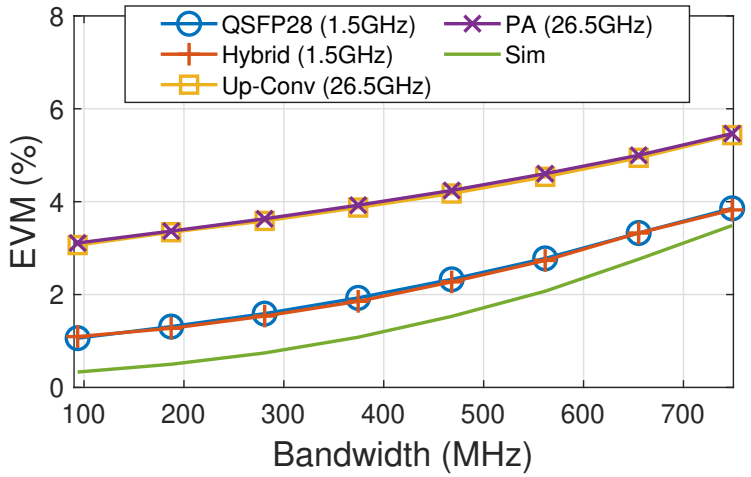

Figure 5.5: Bandwidth performance in each stage of one channel of the RRH. The EVM for an ideal sigma-delta modulated simulation is included as a reference (Sim) [F].

5.2.2 Transmitter Verification

In Paper [F], the comprehensive verification results encompass power levels, oscillation signal phase noise, system coherence, signal spectrum, and bandwidth performance. The power level analysis indicates that each channel delivers a consistent inband power of 17.3 dBm. Additionally, the oscillation signal exhibits reasonable phase noise, ensuring effective mm-wave signal upconversion.

Figure 5.4 displays the output spectrum for one channel of the RRH. The spectrum includes inband signal, LO leakage, lower sideband, and quantization noise within the 33 GHz measured band. Notably, the inband signal exhibits a 25 dB higher amplitude compared to the other components. For specialized applications in the future, the implementation could benefit from the inclusion of dedicated IF BPFs within the RRH to further enhance suppression. This analysis shows that the output signal does not exhibit any spurious issues.

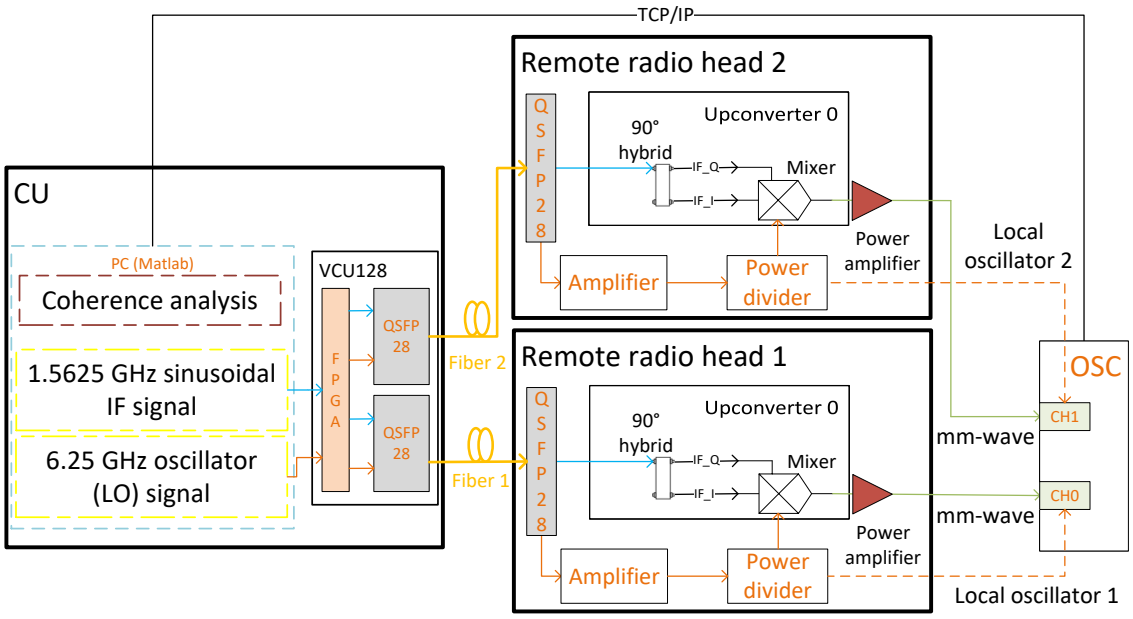

Figure 5.6: LO and mm-wave signal coherence measurement setup [F].

The bandwidth performance of the TX, with an ideal BPSDM simulation as a reference, is presented in Figure 5.5. The EVM experiences degradation as the bandwidth increases, with a fixed SDM sample rate and decreasing oversampling ratio from 268.8 to 33.4. The bandwidth is ultimately limited by quantization distortion induced by the oversampling ratio and the second-order BPSDM modulation scheme employed. For the 1.5 GHz IF signal, both the QSFP28 and hybrid exhibit similar EVM performance, albeit with differences in inband power. Notably, hardware limitations, stemming from the FPGA and fiber link, contribute to variations between IF signal measurements and simulations. After mixer upconversion, the mm-wave signals (26.5 GHz) demonstrate inferior EVM performance compared to IF signals, primarily due to the introduction of LO phase noise. It is noteworthy that the PA introduces no significant distortion, as evidenced by the overlapping mixer and PA output curves. In conclusion, the TX demonstrates the capability to support a 748 MHz wideband OFDM 64-QAM signal with a 5.5% EVM performance.

Figure 5.6 presents the measurement setup used for the investigation of system coherence. In the TX configuration, the CU generates two identical periodic bitstreams, each comprising repeated sequences of two ones and two zeros. These bitstreams are then transmitted to the two RRHs through dedicated channels. To assess the coherence of the system at the phase level, the CU generates 6.25 GHz LO signals from a common 25 Gbps bitrate. Simultaneously, sinusoidal IF signals at 1.5625 GHz are produced by the CU through the repetition of eight ones and eight zeros. The coherence analysis reveals standard deviations of 1.52° and 6.28° for the LO signals and mm-wave signals, respectively. Further analysis can be found in Paper [F].

The verification confirms that the proposed implementation is capable of supporting effective wideband, linear, and coherent transmission for communication signals within a D-MIMO system.

5.2.3 OFDM MIMO Precoding

In our experimental setup, channel estimation constitutes the initial phase, followed by precoded communication. To show the capabilities of wideband transmission with nonflat frequency responses, we employ an OFDM 64-QAM modulation scheme, utilizing parameters detailed in Table 5.1. The TX signal processing involves filtering, upsampling, and upconversion of the OFDM signal before the application of SDM. On the RX side of the demonstrator, offline frequency/timing synchronization is performed before the final OFDM demodulation step.

Table 5.1: OFDM signal parameters [F].

Parameter	**Value**
FFT size	1024 subcarriers
DC	null
Guard band 1	121 subcarriers
Guard band 2	122 subcarriers
Cyclic prefix	128 samples
Subcarrier number	780 subcarriers
Bandwidth (MHz)	93.6 187.2 280.8 374.4 468 561.6 655.2 748.8
Subcarrier spacing (KHz)	120 240 360 480 600 720 840 960

During the channel estimation step, the CU generates OFDM pilot signals to the RRHs. Adhering to the same OFDM pilot principle as outlined in [90], it becomes necessary to transmit N OFDM symbols to estimate N channels. This necessity arises from the fact that only one TX antenna carries a quadrature phase shift keying (QPSK) pilot symbol for one subcarrier at each OFDM symbol, while others remain deactivated. The resulting OFDM pilot symbol is then expressed by

$$\mathbf{X} = \begin{bmatrix} x_1 & 0 & .. & 0 & 0 & .... & 0 \\ 0 & x_2 & .. & 0 & x_{K+1} & .... & 0 \\ 0 & 0 & .. & 0 & 0 & .... & 0 \\ .. & .. & .. & .. & .. & .... & .. \\ .. & .. & .. & .. & .. & .... & x_{K\times N} \\ 0 & 0 & .. & x_K & 0 & .... & 0 \end{bmatrix} \tag{5.1}$$

$\mathbf{X}$ has a dimension of $N \times (N \times K)$, where N represents the channel number of TX antennas, which equals the number of OFDM symbols, and K is the number of subcarriers.

On the RX end, signals are received by M users. The procedures for LS channel estimation and ZF precoding are consistent, following the formulations in Equations (2.17) and (2.19) for each subcarrier i. $\{M, K, N\}$ is {2,780,6} for the MIMO procedure in this demonstration. For the MISO case, the channel estimation and precoding procedures remain identical to those in the MIMO case, with $M = 1$.

5.2.4 OTA measurements

In the following section, we will report OTA experiments demonstrating how the presented TX can be used for single- and multiple-user experiments.

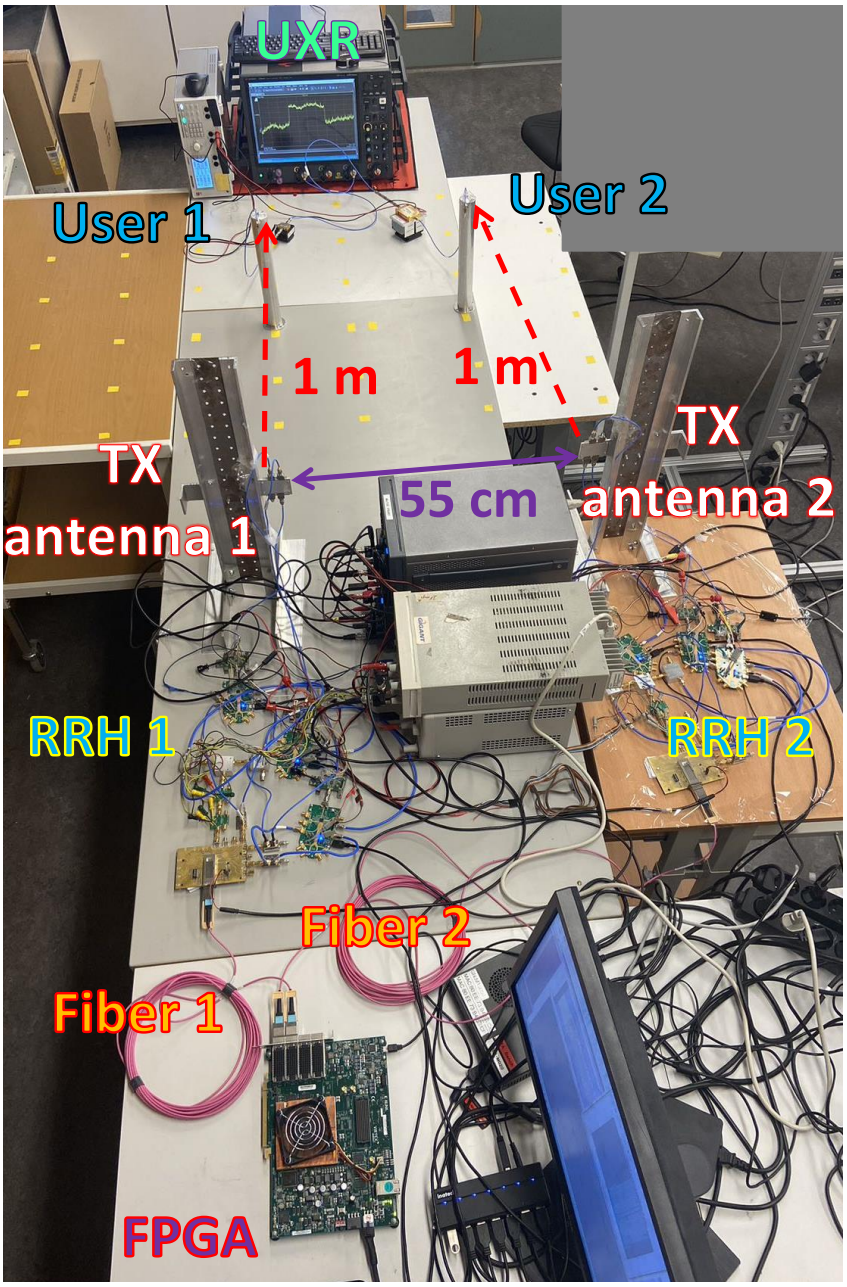

Figure 5.7: Measurement setup for investigation of the proposed transmitter. The two transmitting antennas are separated by 55 cm. The yellow labels attached to the bench indicate the user positions where OTA measurements were carried out [F].

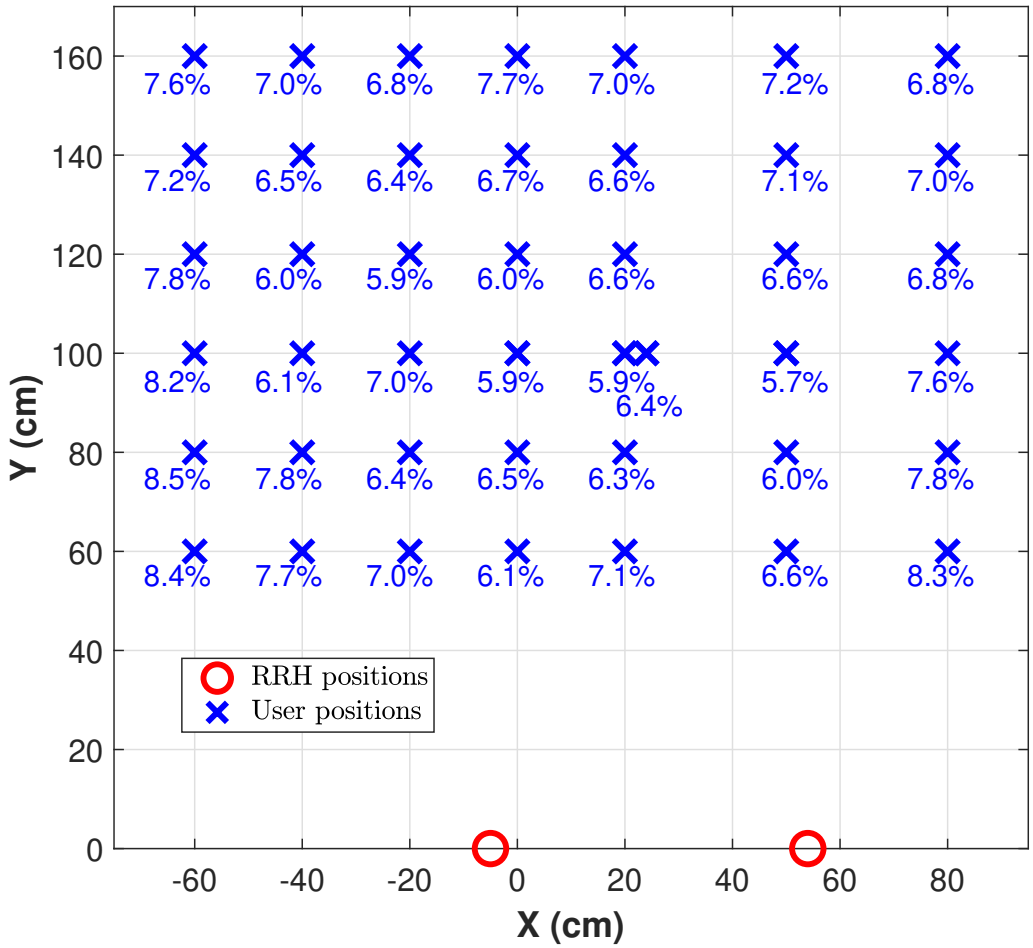

Figure 5.8: Error vector magnitude (EVM) coverage of the MISO measurements at 43 labeled positions as shown in Figure 5.7 [F].

MISO Performance

Independent receiving antennas are freely movable within this area for the MISO measurements. The MISO measurements are carried out within a designated area measuring 1.4 m × 1.6 m, marked at positions as illustrated in Figure 5.7. At each marked position, channel estimation and precoding are performed using a 748 MHz bandwidth OFDM signal, with pilot signals defined in (5.1) transmitted for channel estimation. In the subsequent step, the TX sends ZF-precoded OFDM 64-QAM data.

Figure 5.8 depicts the locations of the RRH and users utilized for these experiments and those that follow. The numbers in Figure 5.8 correspond to the EVM from the MISO experiments. The majority of positions meet the 8% EVM requirement specified for the OFDM 64-QAM signal set in the 3GPP [78]. Some peripheral positions exhibit worse EVM, particularly when users are situated at the limits of the antenna coverage area. Within the central region, the EVM is better than 6%.

Multi-User MIMO Performance

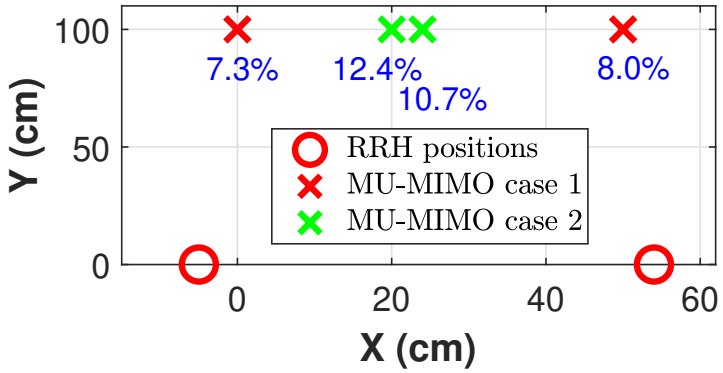

Figure 5.9: User positions of MU-MIMO measurements with Error vector magnitude (EVM) results with 748 MHz bandwidth signal [F].

In this MU-MIMO measurement setup, two RRHs serve two independent users. The measurement considers two cases that separate the two users by 50 cm and 5 cm, respectively (refer to Figure 5.9). For each case, the TX initiates the transmission by radiating pilot signals for LS channel estimation and subsequently executes the transmission of ZF-precoded user data. Compared with the previous MISO measurements at the corresponding locations, the 748 MHz bandwidth MU-MIMO measurements have worse EVM results due to the ZF-precoder allocating lower power per user in the two-user cases. Additionally, the channel response study in Paper [F] presents significant channel amplitude variations. This emphasizes the necessity for frequency-domain channel estimation and precoding in wideband applications.

The MU-MIMO measurements with the EVM results for different bandwidths are presented in Figure 5.10. Specifically, Case 1 demonstrates superior EVM for the two users compared to Case 2, attributed to the increased channel diversity resulting from more separated user positions. Generally, both cases serve two users

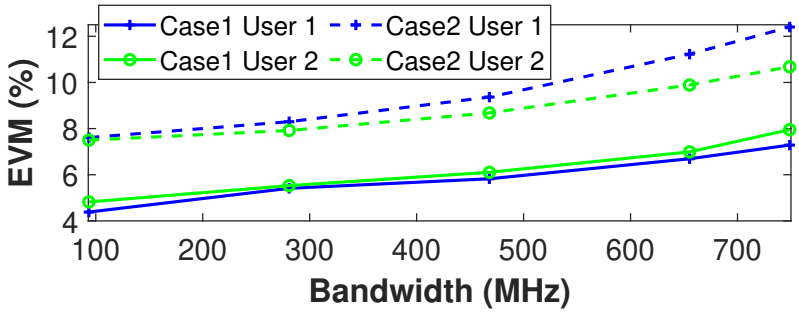

Figure 5.10: Error vector magnitude (EVM) results from MU-MIMO measurements with different bandwidths [F].

effectively. Furthermore, in Case 1, both users meet the EVM requirements specified by the 3GPP [78] for OFDM 64-QAM signals up to a 748 MHz bandwidth, exhibiting consistent performance as promised by the employed ZF precoding scheme.

Paper [F] investigates the inter-user interference in MU-MIMO measurements by analyzing the error spectrum in comparison to the received spectrum. The error spectrum serves as a frequency domain representation of the demodulated constellation's difference from the reference constellation for users. The results show that inter-user interference in Case 2 is attributed to the ill-conditioning of the channel matrix due to the closer user positions.

5.3 W-band Baseband SDoF D-MIMO Demonstrator

The previous section presents the proposed mm-wave IF SDoF D-MIMO architecture with demonstration results. In this section, the proposed mm-wave baseband SDoF D-MIMO architecture is implemented with off-the-shelf components and validated at 100 GHz (W-band).

5.3.1 Transmitter Implementation

Paper [G] extensively documents the implementation of the W-band demonstrator. The W-band D-MIMO system, depicted in Figure 5.11, is constructed on the baseband SDoF architecture from Chapter 4 and comprises a CU and two RRHs. The CU utilizes a PC to process two second-order LPSDMs. Additionally, the CU incorporates an FPGA board equipped with two QSFP28-enabled fiber connections. The CU generates two 12.5 GHz LO signals with periodic binary patterns (101010...). These LO signals, along with I/Q SDM bitstreams, are transmitted via fiber connections to the two RRHs.

In the RRHs, the differential I/Q SDM electric signals directly interface with the baseband inputs of a W-band active upconverter (gMTX0033A) [92]. The 12.5 GHz LO signals are first amplified using an amplifier (Analog Devices EVAL-HMC490LP5) before reaching the LO inputs of the active upconverter. The active upconverter

incorporates a times-eight (× 8) frequency multiplier for the LO input and emits a 100 GHz signal through an open waveguide.

In Figure 5.11, there is a receiving user (gMRX0033A) [92] equipped with the same open waveguide as the RRHs. The user unit requires a LO signal, incorporating an integrated times-eight (× 8) frequency multiplier, to downconvert the received 100 GHz signal to a differential I/Q signal. The I/Q signal is then sampled by an oscilloscope (Keysight UXR0334A Infiniium UXR-Series: 33 GHz, 4 Channels). Subsequent processing involves frequency/phase/timing synchronization and an I/Q equalizer before signal demodulation and constellation presentation.

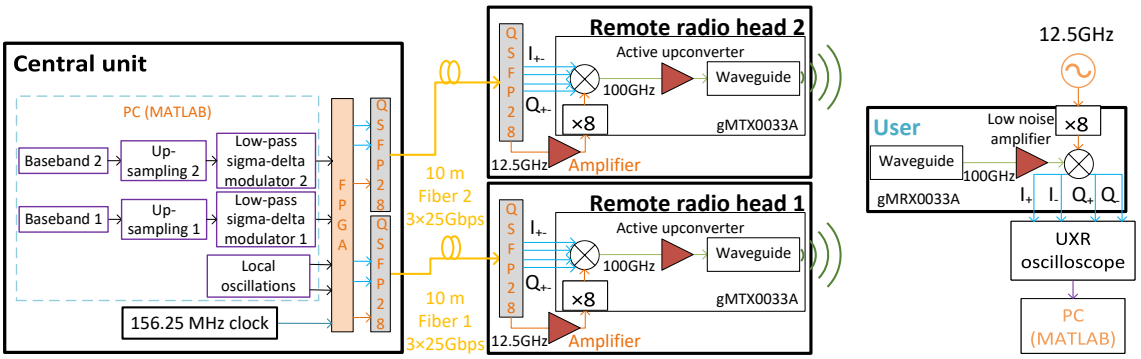

Figure 5.11: W-band distributed antenna system using a low-pass sigma-delta-over-fiber architecture with one user for demonstration [G].

5.3.2 Signal Processing

This system employs a single-carrier 16-(QAM) signal and necessitates two stages of channel estimation and precoding for MISO beamforming.

The system transmits orthogonal pilots of $\mathbf{X}$ at the channel estimation stage

$$\mathbf{X} = \begin{bmatrix} \mathbf{x}_1 & \mathbf{0} \\ \mathbf{0} & \mathbf{x}_2 \end{bmatrix}_{\mathrm{N}\times 2}. \tag{5.2}$$

The user baseband signal processing includes frequency/phase/timing synchronization and an I/Q equalizer. With the received aligned signal, the system can estimate channel effects, by the LS principle with equation (2.7).

The precoding solution of this system is uniform-amplitude MRT, as (2.10), since it is simpler than ZF in the implementation.

5.3.3 Measurement Results

The W-band D-MIMO system has been implemented for demonstration, as depicted in Figure 5.12. The LO signal performance and OTA demonstration results were measured for the system.

Power levels, phase noise, and coherence of the 12.5 GHz LO signals in the RRHs are thoroughly documented in Paper [G]. The phase coherence analysis of LO signals

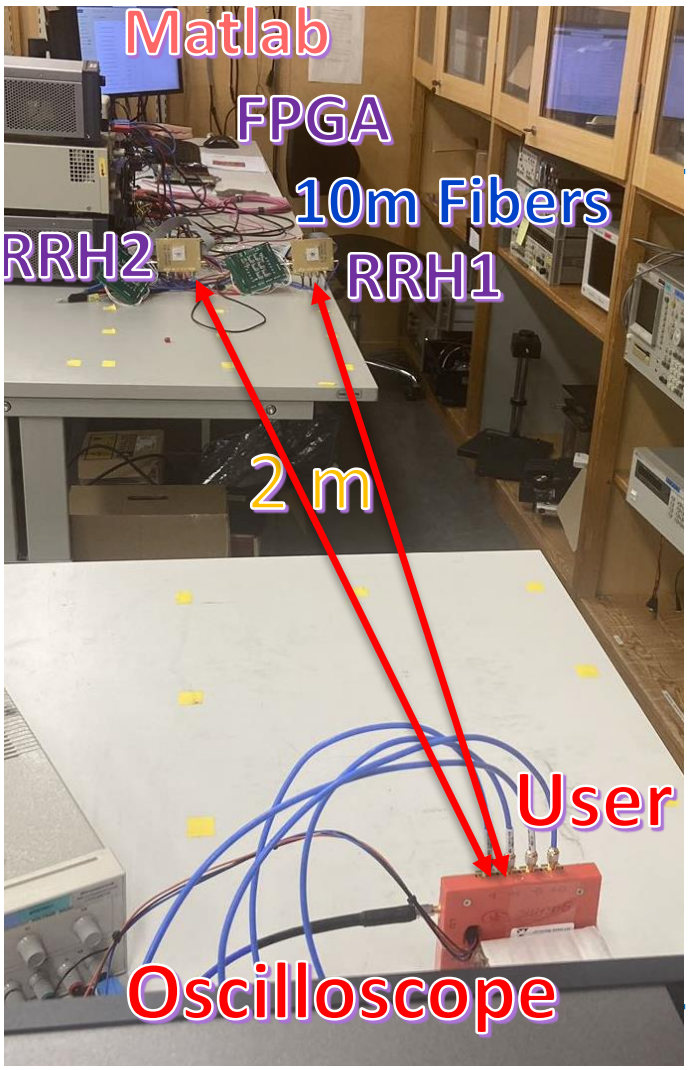

Figure 5.12: W-band distributed antenna system using a low-pass sigma-delta-over-fiber architecture with one user for demonstration [G].

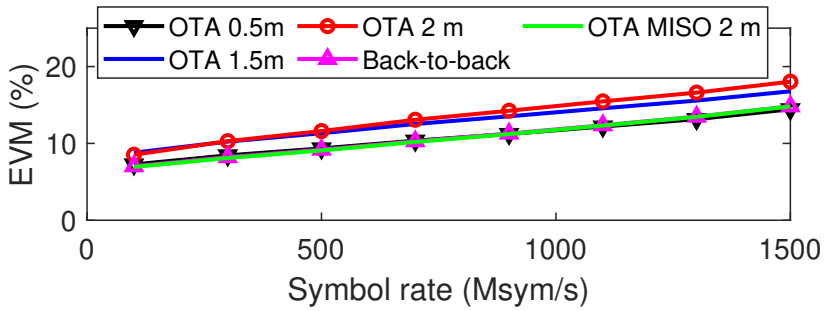

Figure 5.13: Symbol rate performance at different cases [G].

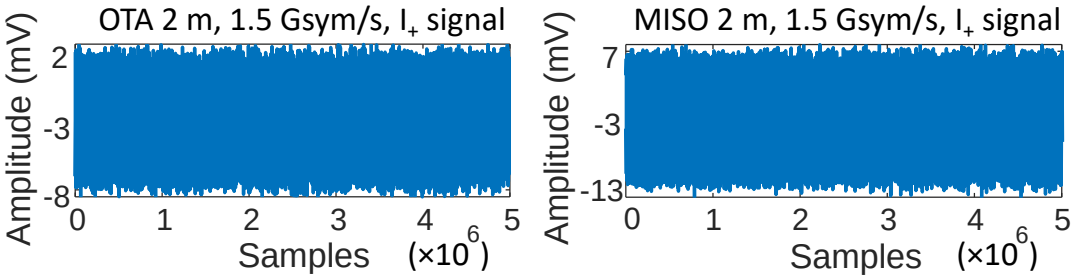

Figure 5.14: Received signal amplitude for SISO and MISO cases [G].

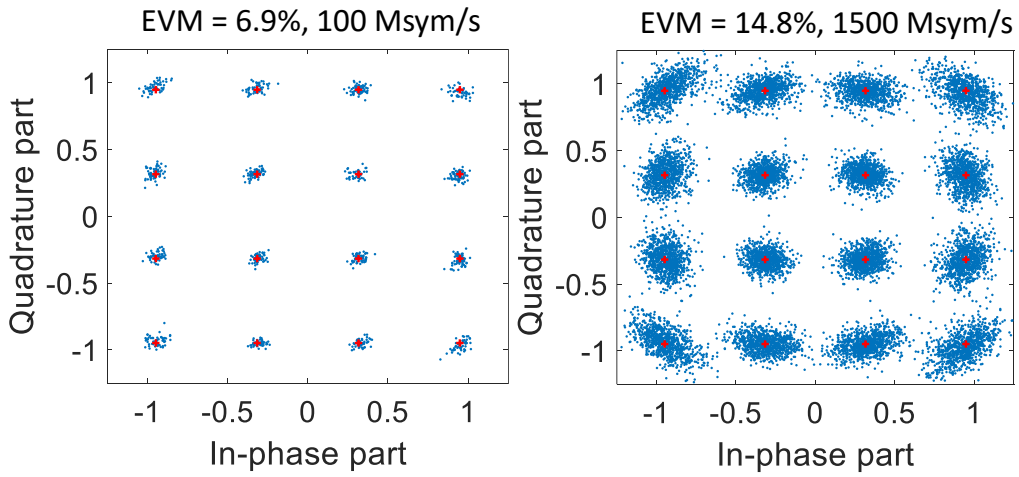

(a)

Figure 5.15: Constellation results for 100 Msym/s and 1500 Msym/s signals at MISO case [G].

reveals a standard deviation of only 3.6°, and the RF signals phase coherence is multiplied by a factor of 8, indicating excellent performance for D-MIMO systems.

There are three SISO cases and one MISO case for OTA measurements. The SISO demonstration involves OTA distances of 0.5 m, 1.5 m, and 2 m, while the MISO case operates at a 2 m OTA distance with symbol rates ranging from 100 Msym/s to 1500 Msym/s. A back-to-back measurement serves as a benchmark in Figure 5.13. The SISO OTA 0.5 m and the back-to-back reference exhibit similar results, whereas the SISO OTA 1.5 m and 2 m cases show worse performance. The EVM is enhanced to match the back-to-back reference with the MRT beamforming of MISO. For the 2 m measurement results in Figure 5.14, the MISO signal has a doubled amplitude of 20 mV compared to the corresponding SISO case. In Figure 5.15, MISO measurements yield EVMs of 6.9% and 14.8% for constellations with symbol rates of 100 Msym/s and 1500 Msym/s, corresponding to throughputs of 400 Mbps and 6 Gbps, respectively.

5.4 Chapter Conclusion

This chapter summarized RoF D-MIMO systems which are mostly based on ARoF and SDoF architectures. Furthermore, paper [F] and paper [G] proposed IF SDoF and

baseband SDoF-enabled D-MIMO demonstrations with detailed verification. Table 5.2 compares the proposed demonstrations with the state-of-the-art RoF D-MIMO publications. The proposed IF SDoF D-MIMO system has the greatest bandwidth performance with two users in the SDoF category and the proposed SDoF D-MIMO system works on the W-band spectrum.

Table 5.2: Comparison with state-of-the-art RoF D-MIMO publications.

Ref.	**RoF**	**MIMO**	**Bandwidth**	**OTA**	**Carrier**	**NMSE**
[93]	ARoF	4×1	800 MHz	10 m	28 GHz	-24.3 dB
[89]	ARoF	2×1	3 GHz	1.5 m	28 GHz	-23 dB
[90]	IF SDoF	2×1	160.32 MHz	2.0 m	$>$ 24 GHz	-24.4 dB
Paper [F]	IF SDoF	$(2 \times 3) \times 2$	748 MHz	1.0 m	26.5 GHz	-22 dB
Paper [G]	Baseband SDoF	2×1	1.5 GHz	2.0 m	100 GHz	-16.6 dB

Chapter 6

Conclusions and Future Work

6.1 Conclusions

This thesis explores fiber-connected wireless MIMO communication systems to enhance channel capacity for future beyond-5G and 6G systems. The MIMO capacity is statistically investigated using an automated measurement testbed and raytracing-based electromagnetic propagation software. Additionally, we propose an innovative wideband mm-wave SDoF link architecture for future mm-wave D-MIMO systems.

The MIMO testbed is designed with 12 RRHs and one automatic RX to investigate MIMO capacity. The automatic RX is an RF RX mounted on a programmed robot car capable of moving anywhere and acting as a user. Using this testbed, the automatic system collected channel information from 44 users in an indoor environment with D-MIMO and C-MIMO antenna configurations. Additionally, a raytracing-based electromagnetic propagation software was utilized to conduct a channel simulation for the same indoor area. Through an investigation of MIMO capacity based on Shannon capacity, with randomly selected four-channel information, the probability results indicate that the D-MIMO channel exhibits higher capacity than the C-MIMO case. The findings demonstrate that D-MIMO provides more uniform capacity for any random combinations compared to C-MIMO.

The mm-wave band has a broader bandwidth compared to a low-frequency signal and can accommodate applications with high-capacity demands. However, the mm-wave signal presents drawbacks such as high pass loss and low penetration. Thus, this thesis introduces and verifies an mm-wave SDoF link architecture with digital beamforming and MU-MIMO functionalities. In this mm-wave link, a QSFP28-based fiber connects the CU with the RRH and supports four sub-channels. A linear array antenna is used in the RRH to radiate the mm-wave signal and communicate with two users, represented by measurement equipment. The demonstration of the digital beamforming MISO reaches up to 700 MSym/s, and the MU-MIMO function achieves 500 MSym/s for two users.

Two types of SDoF-based mm-wave D-MIMO architectures are introduced with corresponding system implementations. Both architectures have coherent CU-inherited LO signals. The mm-wave bandpass SDoF D-MIMO system is validated through MISO and MU-MIMO measurements using an OFDM signal with a band-

width of up to 748 MHz. The mm-wave lowpass SDoF D-MIMO system is finally extended to the W-band for MISO measurement cases.

The thesis has proposed and developed several testbeds that help to experimentally verify the theoretical predictions of improved coverage uniformity and capacity of D-MIMO. The testbeds are flexible, low-complex, and built with off-the-shelf components, which make them suitable for large-scale experiments in realistic environments.

6.2 Future Work

With the future communication system requirement and current technology evolvement, the following topics will be exciting directions to explore.

6.2.1 Complete mm-wave Massive D-MIMO System

This thesis has studied mm-wave D-MIMO architectures using SDoF, and it can be extended to a mm-wave massive D-MIMO system. There are lots of system-level possibilities to pursue. Firstly, this study is only on DL direction, An integrated complete mm-wave massive D-MIMO system with UL and DL is the final step to approach. Secondly, digital compensation of RRH hardware impairment will be an attractive topic for investigation to further improve the D-MIMO testbed performance.

6.2.2 Localization

Future communication networks will be more powerful by having localization functions. With localization functions, the user not only has a communication service but also has a localizing service. Currently, the localization solutions [I] [94]–[99] have not fully explored the phase coherency property of the mm-wave D-MIMO systems.

6.2.3 mm-wave incoherent D-MIMO System

The mm-wave coherent D-MIMO architectures of this thesis also have the flexibility to be operated in an incoherent mode, where each RRH has its own LO. It is quite common to have an incoherent system in reality. Therefore, mm-wave incoherent D-MIMO systems study is a potential and interesting field to explore.

Chapter 7

Summary of Appended Papers

Paper [A]

Automatic Distributed MIMO Testbed for Beyond 5G Communication Experiments

This paper demonstrates an automated testbed suitable for beyond-5G distributed MIMO experiments, where bandwidth, number of transmitters and precoding methods are flexible and configured through a central unit. This is based on an all-digital RoF approach to communication through 12 fully coherent, low-complexity RRHs. An automated robot receiver is implemented to facilitate efficient communication data collection in realistic environments. Using the proposed system, C- and D-MIMO communication antenna configurations are compared in a real in-door environment. The results show that D-MIMO provides significantly more uniform power distribution and better overall MIMO capacity compared to C-MIMO.

Author contributions: Husileng designed the automatic robot receiver for the D-MIMO testbed and executed the indoor D-MIMO and C-MIMO communication measurements. Furthermore, Husileng processed the raw data from the measurements to have the power distribution and channel capacity results for the communication cases. In the end, Husileng prepared the manuscripts for this publication. Co-authors contributed with analysis of the measurement results and commenting on manuscripts.

Paper [B]

Comparison of Co-located and Distributed MIMO for Indoor Wireless Communication

This paper compares the communication performance for co-located and emerging D-MIMO in a typical indoor scenario. The simulations, verified against experimental measurement data, show that D-MIMO offers users a significantly more uniform

capacity. The results also show that the same user capacity can be achieved with half the number of antennas in the D-MIMO case.

Author contributions: Husileng was responsible for the measurement results and supervised the students with simulation configurations for the master thesis report. The first author prepared the manuscript and presented the paper in 2022 IEEE Radio and Wireless Symposium (RWS).

Paper [C]

Demonstration of Flexible mmWave Digital Beamforming Transmitter using Sigma-Delta Radio-Over-Fiber Link

This work proposed SDM enabled mm-wave MIMO transmitter and demonstrated mm-wave digital beamforming based on the proposed link. The digital beamforming is controlled from a central unit and distributed to a remote radio unit using a standardized QSFP28 fiber connection. The solution offers a flexible transmitter solution suitable for mm-wave distributed active antenna systems.

Author contributions: Husileng designed, developed, and verified all hardware/software of the transmitter for this demonstration. Husileng updated the receiver's performance for this publication and wrote the manuscripts for the submission. Husileng presented the paper at the 2022 52th European Microwave Conference (EuMC). Co-authors contributed to the analysis of the measurement results and commenting on manuscripts.

Paper [D]

Flexible mm-Wave Sigma-Delta-over-Fiber MIMO Link

This paper investigated a flexible mm-wave SDoF-based transmitter solution with digital beamforming MISO and MIMO functionality. A CU controls those functions by connecting a RRH with a standardized QSFP28 fiber link. The CU generates binary-encoded intermediate frequency signals using bandpass SDM. The QSFP28-based fiber link transmits the IF bitstreams to the RRH. The RRH consists of a QSFP28 module, 90° hybrids, and upconverters. The RRH feeds four parallel, independent, coherent, and CU-controlled mm-wave signals to a linear array transmitting antenna. The transmitter was experimentally verified and demonstrated digital OTA beamforming MISO/MU-MIMO communication. The results show that the proposed link can be used for the realization of scalable, low-cost, and flexible transmitter solution for emerging distributed antenna systems.

Author contributions: Husileng designed, developed, updated, and verified all hardware/software parts to have a flexible wideband setup. Husileng also developed the receiver's application for verification/MISO/MIMO measurements. Husileng wrote the manuscripts for submission. During major and minor revisions, Husileng prepared the response letter and revised the manuscript. Co-authors contributed to the analysis of demonstration results, commenting and revision of manuscripts.

Paper [E]

Wideband mm-wave Spectrum-Efficient Transmitter Using Low-Pass Sigma–Delta-Over-Fiber Architecture

This work proposed a mm-wave RoF architecture suitable for wideband mm-wave communication, using a low-pass SDM approach. The CU generates baseband sigma–delta bitstreams, I/Q components, which are transported to a RRH using a standard QSFP28 optical interconnect link connection. In the RRH, the baseband I/Q signals are upconverted to the mm-wave band, amplified, and transmitted through an antenna. The performance of the resulting SDoF transmitter architecture was experimentally verified and demonstrated a state-of-the-art symbol rate of up to 1.5 Gsym/s. Furthermore, in OTA measurements, the architecture supported 64/256/1024-QAM cases over a 5-m wireless distance. The results demonstrated the feasibility of the proposed architecture for the realization of wideband mm-wave distributed antenna systems.

Author contributions: Husileng designed, developed, and verified all hardware/software parts for the low-pass SDoF architecture and developed the receiver's applications for verification/OTA measurements. Husileng wrote the manuscripts for submission. Husileng prepared the response letter and revised the manuscript during revisions. Co-authors contributed to the analysis of demonstration results, commenting and revision of manuscripts.

Paper [F]

Wideband mm-wave 6 × 2 Distributed MIMO Transmitter using Sigma-Delta-over-Fiber

This paper investigated a mm-wave SDoF D-MIMO solution, in which a CU connects two RRHs with two standardized QSFP28 fiber connections. The four subchannels of the QSFP28 carry three individually controlled IF SDM bitstreams and one LO signal to each RRH. At each RRH, the upconversion to mm-wave frequency is performed while maintaining full phase coherence between all channels and distributed RRHs. This solution offers an effective and scalable way to feed multiple radio heads with coherent signals proper for high-performance mm-wave D-MIMO systems. The

comparison with other publications shows that the proposed system is the first mm-wave SDoF D-MIMO solution that serves multiple users and reaches the largest bandwidth.

Author contributions: Husileng designed, developed, and verified all hardware/software parts for the distributed systems in Ericsson/Italy and in Chalmers, and developed the receiver's applications for verification/MISO/MIMO measurements. Husileng suggested and implemented an orthogonal frequency-division multiplexing (OFDM) solution for wideband results. Husileng wrote the manuscripts for submission. Co-authors contributed to the analysis of results and experiments and to commenting and revision of manuscripts.

Paper [G]

W-Band Distributed MIMO Demonstration using Low-Pass Sigma-Delta-over-Fiber

This paper explores a 100 GHz distributed low-pass SDoF communication demonstration for greater data rates. Specifically, the study introduces a W-band distributed system architecture, utilizing commercially available off-the-shelf hardware components. Experimental findings achieved a symbol rate of 1.5 Gsym/s over a 2 m OTA transmission distance. This work is the first demonstration of a distributed antenna system for W-band applications.

Author contributions: Husileng integrated all of the hardware parts for the system. Furthermore, Husileng designed, developed, and verified all software parts for the system demonstration. Husileng wrote the manuscripts for submission. Co-authors commented on the measurement results and manuscripts.

References

[1] Ericsson. "Ericsson Mobility Report." Reports and Papers. (Nov. 2022), [Online]. Available: https://www.ericsson.com/en/reports-and-papers/mobility-report/mobility-visualizer.

[2] J. G. Andrews, S. Buzzi, W. Choi, S. V. Hanly, A. Lozano, A. C. Soong, and J. C. Zhang, "What Will 5G Be?" *IEEE Journal on selected areas in communications*, vol. 32, no. 6, pp. 1065–1082, 2014.

[3] J. Navarro-Ortiz, P. Romero-Diaz, S. Sendra, P. Ameigeiras, J. J. Ramos-Munoz, and J. M. Lopez-Soler, "A Survey on 5G Usage Scenarios and Traffic Models," *IEEE Communications Surveys Tutorials*, vol. 22, no. 2, pp. 905–929, 2020.

[4] A. Gupta and R. K. Jha, "A Survey of 5G Network: Architecture and Emerging Technologies," *IEEE Access*, vol. 3, pp. 1206–1232, 2015.

[5] M. Jaber, M. A. Imran, R. Tafazolli, and A. Tukmanov, "5G Backhaul Challenges and Emerging Research Directions: A Survey," *IEEE Access*, vol. 4, pp. 1743–1766, 2016.

[6] J. M. Khurpade, D. Rao, and P. D. Sanghavi, "A Survey on IOT and 5G Network," *2018 International Conference on Smart City and Emerging Technology (ICSCET)*, pp. 1–3, 2018.

[7] FAIST. "Distribution of 5G in cities and Countries worldwide." Blog. (Dec. 2022), [Online]. Available: https://www.faistgroup.com/news/distribution-5g-worldwide/.

[8] S. A. Abdel Hakeem, H. H. Hussein, and H. Kim, "Vision and research directions of 6g technologies and applications," *Journal of King Saud University - Computer and Information Sciences*, vol. 34, no. 6, Part A, pp. 2419–2442, 2022.

[9] J. Zong, Y. Liu, H. Liu, Q. Wang, and P. Chen, "6G Cell-Free Network Architecture," in *2022 IEEE 2nd International Conference on Electronic Technology, Communication and Information (ICETCI)*, 2022.

[10] Ericsson. "Follow the journey to 6G." 6G. (Dec. 2022), [Online]. Available: https://www.ericsson.com/en/6g.

[11] NOKIA Bell Labs. "What is 6G?" Research and Innovation. (Dec. 2022), [Online]. Available: https://www.bell-labs.com/research-innovation/what-is-6g/.

[12] European Commission. "6G research gets €130 million EU funding boost in Europe." Smart Networks and Services. (Jan. 2024), [Online]. Available: https://digital-strategy.ec.europa.eu/en/news/6g-research-gets-eu130-million-eu-funding-boost-europe.

[13] University of Oulu. "6G Flagship." (Dec. 2022), [Online]. Available: https://www.6gflagship.com/.

[14] E. G. Larsson, O. Edfors, F. Tufvesson, and T. L. Marzetta, "Massive MIMO for next generation wireless systems," *IEEE Communications Magazine*, vol. 52, no. 2, pp. 186–195, 2014.

[15] G. Interdonato, E. Björnson, H. Quoc Ngo, P. Frenger, and E. G. Larsson, "Ubiquitous cell-free massive MIMO communications," *EURASIP Journal on Wireless Communications and Networking*, vol. 2019, pp. 1–13, 2019.

[16] R. Roy, "Spatial division multiple access technology and its application to wireless communication systems," in *1997 IEEE 47th Vehicular Technology Conference. Technology in Motion*, vol. 2, 1997.

[17] C. E. Shannon, "A mathematical theory of communication," *The Bell system technical journal*, vol. 27, no. 3, pp. 379–423, 1948.

[18] T. L. Marzetta, E. G. Larsson, H. Yang, and H. Q. Ngo, *Fundamentals of Massive MIMO*. Cambridge University Press, 2016.

[19] D. Tse and P. Viswanath, *Fundamentals of Wireless Communication*. Cambridge University Press, 2005.

[20] S. Kay, *Fundamentals of Statistical Signal Processing: Estimation theory* (Fundamentals of Statistical Signal Processing). Prentice-Hall PTR, 2013.

[21] E. Björnson, L. Sanguinetti, H. Wymeersch, J. Hoydis, and T. L. Marzetta, "Massive MIMO is a reality—What is next?: Five promising research directions for antenna arrays," *Digital Signal Processing*, vol. 94, pp. 3–20, 2019, Special Issue on Source Localization in Massive MIMO.

[22] E. Björnson, J. Hoydis, and L. Sanguinetti, "Massive MIMO Networks: Spectral, Energy, and Hardware Efficiency," *Foundations and Trends® in Signal Processing*, vol. 11, no. 3-4, pp. 154–655, 2017.

[23] Ö. T. Demir, E. Björnson, and L. Sanguinetti, "Foundations of user-centric cell-free massive MIMO," *Foundations and Trends® in Signal Processing*, vol. 14, no. 3-4, pp. 162–472, 2021.

[24] Business Research Insights. "Radio-over-Fiber market." Market Reports. (Feb. 2023), [Online]. Available: https://www.businessresearchinsights.com/market-reports/radio-over-fiber-market-100128.

[25] C. Lim, Y. Tian, C. Ranaweera, T. A. Nirmalathas, E. Wong, and K.-L. Lee, "Evolution of Radio-Over-Fiber Technology," *J. Lightwave Technol.*, vol. 37, no. 6, pp. 1647–1656, 2019.

[26] J. Yuan, Y. Liu, Y. Hu, G. Xu, and J. C. Zhang, "Distributed FD-MIMO (D-FD-MIMO): from Concept to Field Test," in *2022 IEEE Radio and Wireless Symposium (RWS)*, 2022.

[27] A. I. Salama and M. M. Elmesalawy, "Experimental OAI-based Testbed for Evaluating the Impact of Different Functional Splits on C-RAN Performance," in *2019 Novel Intelligent and Leading Emerging Sciences Conference (NILES)*, vol. 1, 2019.

[28] I. C. Sezgin, M. Dahlgren, T. Eriksson, M. Coldrey, C. Larsson, J. Gustavsson, and C. Fager, "A Low-Complexity Distributed-MIMO Testbed Based on High-Speed Sigma–Delta-Over-Fiber," *IEEE Transactions on Microwave Theory and Techniques*, vol. 67, no. 7, pp. 2861–2872, 2019.

[29] C.-Y. Wu, H. Li, O. Caytan, J. Van Kerrebrouck, L. Breyne, J. Bauwelinck, P. Demeester, and G. Torfs, "Distributed Multi-User MIMO Transmission Using Real-Time Sigma-Delta-Over-Fiber for Next Generation Fronthaul Interface," *Journal of Lightwave Technology*, vol. 38, no. 4, pp. 705–713, 2020.

[30] C.-Y. Wu, C. Meysmans, H. Li, J. Van Kerrebrouck, O. Caytan, S. Lemey, J. Bauwelinck, P. Demeester, and G. Torfs, "Demonstration of a Scalable Distributed Antenna System Using Real-Time Bit-Interleaved Sigma-Delta-over-Fiber Architectures," in *2020 European Conference on Optical Communications (ECOC)*, 2020.

[31] L. Breyne, G. Torfs, X. Yin, P. Demeester, and J. Bauwelinck, "Comparison Between Analog Radio-Over-Fiber and Sigma Delta Modulated Radio-Over-Fiber," *IEEE Photonics Technology Letters*, vol. 29, no. 21, pp. 1808–1811, 2017.

[32] F. Olofsson, L. Aabel, M. Karlsson, and C. Fager, "Comparison of Transmitter Nonlinearity Impairments in externally modulated Sigma-Delta-over Fiber vs Analog Radio-over-Fiber links," in *2022 Optical Fiber Communications Conference and Exhibition (OFC)*, IEEE, 2022.

[33] I. C. Sezgin, "Sigma-Delta-over-Fiber for High-Speed Wireless Communication Systems," *Chalmers Open Digital Repository*, 2019.

[34] A. Shaikh and M. J. Kaur, "Comprehensive Survey of Massive MIMO for 5G Communications," in *2019 Advances in Science and Engineering Technology International Conferences (ASET)*, 2019.

[35] K. Zhu, M. J. Crisp, S. He, R. V. Penty, and I. H. White, "MIMO System Capacity Improvements Using Radio-over-Fibre Distributed Antenna System Technology," in *2011 Optical Fiber Communication Conference and Exposition and the National Fiber Optic Engineers Conference*, 2011.

[36] J. Vieira, S. Malkowsky, K. Nieman, Z. Miers, N. Kundargi, L. Liu, I. Wong, V. Öwall, O. Edfors, and F. Tufvesson, "A flexible 100-antenna testbed for Massive MIMO," in *2014 IEEE Globecom Workshops (GC Wkshps)*, 2014.

[37] S. Malkowsky, J. Vieira, L. Liu, P. Harris, K. Nieman, N. Kundargi, I. C. Wong, F. Tufvesson, V. Öwall, and O. Edfors, "The World's First Real-Time Testbed for Massive MIMO: Design, Implementation, and Validation," *IEEE Access*, vol. 5, pp. 9073–9088, 2017.

[38] P. Harris, S. Malkowsky, J. Vieira, E. Bengtsson, F. Tufvesson, W. B. Hasan, L. Liu, M. Beach, S. Armour, and O. Edfors, "Performance Characterization of a Real-Time Massive MIMO System With LOS Mobile Channels," *IEEE Journal on Selected Areas in Communications*, vol. 35, no. 6, pp. 1244–1253, 2017.

[39] X. Jiang and F. Kaltenberger, "Demo: an LTE compatible massive MIMO testbed based on OpenAirInterface," in *WSA 2017; 21th International ITG Workshop on Smart Antennas*, 2017.

[40] G. Xu, Y. Li, J. Yuan, R. Monroe, S. Rajagopal, S. Ramakrishna, Y. H. Nam, J.-Y. Seol, J. Kim, M. M. U. Gul, A. Aziz, and J. Zhang, "Full Dimension MIMO (FD-MIMO): Demonstrating Commercial Feasibility," *IEEE Journal on Selected Areas in Communications*, vol. 35, no. 8, pp. 1876–1886, 2017.

[41] Ericsson. "Ericsson Massive MIMO." RAN. (Dec. 2022), [Online]. Available: `http://www-cs-faculty.stanford.edu/~uno/abcde.html`.

[42] P. von Butovitsch, D. Astely, C. Friberg, A. Furuskär, B. Göransson, B. Hogan, J. Karlsson, and E. Larsson, "Advanced antenna systems for 5G networks," *Ericsson White Paper*, 2018.

[43] GlobeNewswire. "Nokia and Sprint demonstrate massive MIMO at MWC17." Source: Nokia Oyj. (Dec. 2022), [Online]. Available: `https://www.globenewswire.com/news-release/2017/02/27/927989/0/en/Nokia-and-Sprint-demonstrate-massive-MIMO-at-MWC17.html`.

[44] A. P. Guevara, C.-M. Chen, and S. Pollin, "Hardware and Spectrum Sharing for Distributed Massive MIMO," in *2018 52nd Asilomar Conference on Signals, Systems, and Computers*, 2018.

[45] C.-M. Chen, V. Volski, L. Van der Perre, G. A. E. Vandenbosch, and S. Pollin, "Finite Large Antenna Arrays for Massive MIMO: Characterization and System Impact," *IEEE Transactions on Antennas and Propagation*, vol. 65, no. 12, pp. 6712–6720, 2017.

[46] C.-M. Chen, Q. Wang, A. Gaber, A. P. Guevara, and S. Pollin, "Experimental Study of User Selection for Dense Indoor Massive MIMO," in *IEEE INFOCOM 2019 - IEEE Conference on Computer Communications Workshops (INFOCOM WKSHPS)*, 2019.

[47] L. Van der Perre, E. G. Larsson, F. Tufvesson, L. D. Strycker, E. Björnson, and O. Edfors, "RadioWeaves for efficient connectivity: analysis and impact of constraints in actual deployments," in *2019 53rd Asilomar Conference on Signals, Systems, and Computers*, 2019.

[48] A. P. Guevara, S. De Bast, and S. Pollin, "Weave and Conquer: A Measurement-based Analysis of Dense Antenna Deployments," in *ICC 2021 - IEEE International Conference on Communications*, 2021.

[49] Ericsson. "Radio Stripes: re-thinking mobile networks." Ericsson Blog. (Feb. 2019), [Online]. Available: `https://www.ericsson.com/en/blog/2019/2/radio-stripes`.

[50] H. Q. Ngo, A. Ashikhmin, H. Yang, E. G. Larsson, and T. L. Marzetta, "Cell-Free Massive MIMO Versus Small Cells," *IEEE Transactions on Wireless Communications*, vol. 16, no. 3, pp. 1834–1850, 2017.

[51] Z. Liu and L. Dai, "Asymptotic capacity analysis of downlink MIMO systems with co-located and distributed antennas," in *2013 IEEE 24th Annual International Symposium on Personal, Indoor, and Mobile Radio Communications (PIMRC)*, IEEE, 2013.

[52] M. K. Bhatt, B. S. Sedani, K. R. Parmar, and M. P. Shah, "Ergodic UL/DL capacity analysis of co-located and distributed antenna configuration for high speed train with massive MIMO system," in *2017 International Conference on Inventive Computing and Informatics (ICICI)*, 2017.

[53] R. Ibernon-Fernandez, J.-M. Molina-Garcia-Pardo, and L. Juan-Llacer, "Comparison Between Measurements and Simulations of Conventional and Distributed MIMO System," *IEEE Antennas and Wireless Propagation Letters*, vol. 7, pp. 546–549, 2008.

[54] E. Rådahl and S. Rimborg, "Simulations of the Capacity and Coverage for a Multi-User Distributed MIMO Network," M.S. thesis, Chalmers University of Technology, 2021.

[55] L. Xiao, L. Dai, H. Zhuang, S. Zhou, and Y. Yao, "Information-theoretic capacity analysis in MIMO distributed antenna systems," in *The 57th IEEE Semiannual Vehicular Technology Conference, 2003. VTC 2003-Spring.*, vol. 1, 2003.

[56] Ettus. "USRP B205mini-i." USRP Bus Series. (Nov. 2022), [Online]. Available: `https://www.ettus.com/all-products/usrp-b205mini-i`.

[57] B. Vucetic and J. Yuan, *Space-time coding*. John Wiley & Sons, 2003.

[58] Remcom. "InSite." Wireless InSite EM propagation software. (Nov. 2022), [Online]. Available: `https://www.remcom.com/wireless-insite-em-propagation-software`.

[59] D. Konstantinou, T. A. Bressner, S. Rommel, U. Johannsen, M. N. Johansson, M. V. Ivashina, A. B. Smolders, and I. T. Monroy, "5G RAN architecture based on analog radio-over-fiber fronthaul over UDWDM-PON and phased array fed reflector antennas," *Optics Communications*, vol. 454, p. 124 464, 2020.

[60] A. H. M. R. Islam, M. Bakaul, and A. Nirmalathas, "Multilevel Modulations for Gigabit Access in a Simple Millimeter-Wave Radio-Over-Fiber Link," *IEEE Photonics Technology Letters*, vol. 24, no. 20, pp. 1860–1863, 2012.

[61] L. Bogaert, J. Van Kerrebrouck, H. Li, I. L. de Paula, K. Van Gasse, C.-Y. Wu, P. Ossieur, S. Lemey, H. Rogier, P. Demeester, G. Roelkens, J. Bauwelinck, and G. Torfs, "SiPhotonics/GaAs 28-GHz Transceiver With Reflective EAM for Laser-Less mmWave-Over-Fiber," *Journal of Lightwave Technology*, vol. 39, no. 3, pp. 779–786, 2021.

[62] R. Budé, M. M. Versluis, G. Nazarikov, S. Rommel, B. van Ark, U. Johannsen, I. T. Monroy, and A. B. Smolders, "Millimeter-Wave Outphasing using Analog-Radio over Fiber for 5G Physical Layer Infrastructure," in *2020 50th European Microwave Conference (EuMC)*, 2021.

[63] R. Puerta, J. Yu, X. Li, Y. Xu, J. J. Vegas Olmos, and I. Tafur Monroy, "Single-Carrier Dual-Polarization 328-Gb/s Wireless Transmission in a D-Band Millimeter Wave 2 × 2 MU-MIMO Radio-Over-Fiber System," *Journal of Lightwave Technology*, vol. 36, no. 2, pp. 587–593, 2018.

[64] T. Nagayama, S. Akiba, T. Tomura, and J. Hirokawa, "Photonics-Based Millimeter-Wave Band Remote Beamforming of Array-Antenna Integrated With Photodiode Using Variable Optical Delay Line and Attenuator," *Journal of Lightwave Technology*, vol. 36, no. 19, pp. 4416–4422, 2018.

[65] M. Morant, A. Trinidad, E. Tangdiongga, T. Koonen, and R. Llorente, "Multi-Beamforming Provided by Dual-Wavelength True Time Delay PIC and Multi-core Fiber," *Journal of Lightwave Technology*, vol. 38, no. 19, pp. 5311–5317, 2020.

[66] I. Lima de Paula, L. Bogaert, O. Caytan, J. Van Kerrebrouck, A. Moerman, M. Muneeb, Q. V. d. Brande, G. Torfs, J. Bauwelinck, H. Rogier, P. Demeester, G. Roelkens, and S. Lemey, "Air-Filled SIW Remote Antenna Unit With True Time Delay Optical Beamforming for mmWave-Over-Fiber Systems," *Journal of Lightwave Technology*, vol. 40, no. 20, pp. 6961–6975, 2022.

[67] K. Ito, M. Suga, T. Arai, Y. Shirato, N. Kita, and T. Onizawa, "Passive beamformer based remote beamforming scheme for radio-over-fiber systems: Experimental demonstration using 28-GHz band reflectarray," *Optics Communications*, vol. 513, p. 128 026, 2022.

[68] H. Li, M. Verplaetse, J. Verbist, J. Van Kerrebrouck, L. Breyne, C.-Y. Wu, L. Bogaert, B. Moeneclaey, X. Yin, J. Bauwelinck, P. Demeester, and G. Torfs, "Real-Time 100-GS/s Sigma-Delta Modulator for All-Digital Radio-Over-Fiber Transmission," *Journal of Lightwave Technology*, vol. 38, no. 2, pp. 386–393, 2020.

[69] F. Zhao, X. Yang, L. Zhao, Y. Wei, and J. Yu, "Demonstration of 4096QAM THz MIMO wireless delivery employing one-bit delta-sigma modulation," *Opt. Lett.*, vol. 47, no. 24, pp. 6361–6364, Dec. 2022.

[70] J. Shi, J. Yu, J. Zhang, M. Zhu, L. Zhang, J. Liu, K. Wang, and W. Zhou, "4096-QAM OFDM THz-over-fiber MIMO transmission using delta-sigma modulation," *IEEE Photonics Technology Letters*, pp. 1–1, 2023.

[71] R. Schreier and G. C. Temes, *Understanding Delta-Sigma Data Converters*. Piscataway, NJ: IEEE press, 2005, vol. 74.

[72] Keysight. "N9042B UXA X-Series Signal Analyzer." Products. (Nov. 2022), [Online]. Available: https://www.keysight.com/it/en/product/N9042B/uxa-signal-analyzer-2-hz-50-ghz.html.

[73] Xilinx, Inc. "Virtex UltraScale+ HBM VCU128 FPGA Evaluation Kit." Boards and Kits. (Nov. 2022), [Online]. Available: https://www.xilinx.com/products/boards-and-kits/vcu128.html.

[74] FS. "Cisco QSFP-100G-SR4-S Compatible 100GBASE-SR4 QSFP28 850nm 100m DOM MTP/MPO-12 MMF Optical Transceiver Module." products. (Nov. 2022), [Online]. Available: https://www.fs.com/de-en/products/48354.html?attribute=12780&id=566810.

[75] Mini-Circuits. "ZX10Q-2-27+." RF & Microwave Products. (Nov. 2022), [Online]. Available: https://www.minicircuits.com/pdfs/ZX10Q-2-27+.pdf.

[76] Mini-Circuits. "ZX10R-14-S+." RF & Microwave Products. (Nov. 2022), [Online]. Available: https://www.minicircuits.com/pdfs/ZX10R-14-S+.pdf.

[77] Analog Devices. "24 GHz to 44 GHz, Wideband, Microwave Upconverter." ADMV1013. (Nov. 2022), [Online]. Available: https://www.analog.com/media/en/technical-documentation/data-sheets/ADMV1013.pdf.

[78] 3GPP, *Evolved Universal Terrestrial Radio Access (E-UTRA); Base Station (BS) radio transmission and reception (release 16) (V16.3.0)*, TS 36.104, TS 36.104, 2019.

[79] T. Ingason and H. Liu, "Line-of-Sight MIMO for Microwave Links-Adaptive Dual Polarized and Spatially Separated Systems," M.S. thesis, Chalmers University of Technology, 2009.

[80] Analog Devices. ">1.5 W (34 dBm), 24 GHz to 34 GHz, GaAs, pHEMT, MMIC, Power Amplifier." HMC943APM5E. (Oct. 2023), [Online]. Available: https://www.analog.com/media/en/technical-documentation/data-sheets/HMC943APM5E.pdf.

[81] R. A. Shafik, M. S. Rahman, and A. R. Islam, "On the Extended Relationships Among EVM, BER and SNR as Performance Metrics," in *2006 International Conference on Electrical and Computer Engineering*, 2006.

[82] M. Sung, J. Kim, E.-S. Kim, S.-H. Cho, Y.-J. Won, B.-C. Lim, S.-Y. Pyun, J. K. Lee, and J. H. Lee, "Demonstration of 5G Trial Service in 28 GHz Millimeter Wave using IFoF-Based Analog Distributed Antenna System," in *2019 Optical Fiber Communications Conference and Exhibition (OFC)*, 2019.

[83] J. Kim, M. Sung, S.-H. Cho, Y.-J. Won, B.-C. Lim, S.-Y. Pyun, J.-K. Lee, and J. H. Lee, "MIMO-Supporting Radio-Over-Fiber System and its Application in mmWave-Based Indoor 5G Mobile Network," *Journal of Lightwave Technology*, vol. 38, no. 1, pp. 101–111, 2020.

[84] M. Sung, J. Kim, E.-S. Kim, S.-H. Cho, Y.-J. Won, B.-C. Lim, S.-Y. Pyun, H. Lee, J. K. Lee, and J. H. Lee, "RoF-Based Radio Access Network for 5G Mobile Communication Systems in 28 GHz Millimeter-Wave," *Journal of Lightwave Technology*, vol. 38, no. 2, pp. 409–420, 2020.

[85] E.-S. Kim, M. Sung, J. H. Lee, J. K. Lee, S.-H. Cho, and J. Kim, "Coverage Extension of Indoor 5G Network Using RoF-Based Distributed Antenna System," *IEEE Access*, vol. 8, pp. 194 992–194 999, 2020.

[86] A. Moerman, J. Van Kerrebrouck, O. Caytan, I. L. de Paula, L. Bogaert, G. Torfs, P. Demeester, H. Rogier, and S. Lemey, "Beyond 5G Without Obstacles: mmWave-over-Fiber Distributed Antenna Systems," *IEEE Communications Magazine*, vol. 60, no. 1, pp. 27–33, Jan. 2022.

[87] L. Bogaert, J. Van Kerrebrouck, H. Li, I. L. de Paula, K. Van Gasse, C.-Y. Wu, P. Ossieur, S. Lemey, H. Rogier, P. Demeester, G. Roelkens, J. Bauwelinck, and G. Torfs, "SiPhotonics/GaAs 28-GHz Transceiver With Reflective EAM for Laser-Less mmWave-Over-Fiber," *Journal of Lightwave Technology*, vol. 39, no. 3, pp. 779–786, 2021.

[88] I. Lima de Paula, S. Lemey, D. Bosman, Q. V. d. Brande, O. Caytan, J. Lambrecht, M. Cauwe, G. Torfs, and H. Rogier, "Cost-Effective High-Performance Air-Filled SIW Antenna Array for the Global 5G 26 GHz and 28 GHz Bands," *IEEE Antennas and Wireless Propagation Letters*, vol. 20, no. 2, pp. 194–198, 2021.

[89] A. Moerman, J. Van Kerrebrouck, O. Caytan, I. L. de Paula, L. Bogaert, G. Torfs, P. Demeester, M. Moeneclaey, H. Rogier, and S. Lemey, "mmWave-over-Fiber Distributed Antenna Systems for Reliable multi-Gbps Wireless Communication," in *2022 3rd URSI Atlantic and Asia Pacific Radio Science Meeting (AT-AP-RASC)*, 2022.

[90] C.-Y. Wu, H. Li, J. Van Kerrebrouck, A. Vandierendonck, I. L. de Paula, L. Breyne, O. Caytan, S. Lemey, H. Rogier, J. Bauwelinck, P. Demeester, and G. Torfs, "Distributed Antenna System Using Sigma-Delta Intermediate-Frequency-Over-Fiber for Frequency Bands Above 24 GHz," *Journal of Lightwave Technology*, vol. 38, no. 10, pp. 2765–2773, 2020.

[91] R. Schreier, *Delta Sigma Toolbox*, Accessed: 2022-12-12.

[92] Gotmic. "Göteborg Microwave Integrated Circuits." (Dec. 2023), [Online]. Available: `https://www.gotmic.se/index.html`.

[93] M. Sung, J. Kim, E.-S. Kim, S.-H. Cho, Y.-J. Won, B.-C. Lim, S.-Y. Pyun, H. Lee, J. K. Lee, and J. H. Lee, "RoF-Based Radio Access Network for 5G Mobile Communication Systems in 28 GHz Millimeter-Wave," *Journal of Lightwave Technology*, vol. 38, no. 2, pp. 409–420, 2020.

[94] G. Piccinni, G. Avitabile, G. Coviello, and C. Talarico, "Real-time distance evaluation system for wireless localization," *IEEE Transactions on Circuits and Systems I: Regular Papers*, vol. 67, no. 10, pp. 3320–3330, 2020.

[95] X. Li, E. Leitinger, M. Oskarsson, K. Åström, and F. Tufvesson, "Massive MIMO-based localization and mapping exploiting phase information of multipath components," *IEEE transactions on wireless communications*, vol. 18, no. 9, pp. 4254–4267, 2019.

[96] C. Liu, Z. Tian, M. Zhou, and X. Yang, "Gene-sequencing-based indoor localization in distributed antenna system," *IEEE Sensors Journal*, vol. 17, no. 18, pp. 6019–6028, 2017.

[97] J. Xiong, K. Jamieson, and K. Sundaresan, "Synchronicity: Pushing the envelope of fine-grained localization with distributed mimo," in *Proceedings of the 1st ACM workshop on Hot topics in wireless*, 2014.

[98] J. Xiong, K. Sundaresan, and K. Jamieson, "Tonetrack: Leveraging frequency-agile radios for time-based indoor wireless localization," in *Proceedings of the 21st Annual International Conference on Mobile Computing and Networking*, 2015.

[99] C. Loyez, M. Bocquet, C. Lethien, and N. Rolland, "A distributed antenna system for indoor accurate WiFi localization," *IEEE Antennas and Wireless Propagation Letters*, vol. 14, pp. 1184–1187, 2015.